University of Michigan
Department of Mechanical Engineering
Cavitation and Multiphase Flow Laboratory

Report No. UMICH 014456-10-I

LIQUID JET AND DROPLET IMPACT (Chapter 6)

by

F. G. Hammitt

Support by ONR Contract NOOO14-76-C-0697

March 24, 1977

VI. Liquid Jet and Droplet Impact

A. Basic Theory and Analysis

1. General

In recent years, substantial efforts here (1-7, eg) and elsewhere have been concentrated upon the computer modelling of droplet and jet impact. It is useful to present a brief review of the status of this field.

To a first approximation, the liquid-solid impact process, as it applies to material erosion, is essentially a non-steady process, basically that classically termed "water-hammer", and governed by Eq. (A-1)

$$\Delta P_{WH} = \rho_o C_o V/g \qquad \text{----------} \qquad \text{(A-1)}$$

The zero subscripts indicate ambient liquid properties.

ΔP_{WH} is the resultant pressure rise, ρ is the liquid density, C the pressure wave celerity (~ sonic velocity) in the liquid, and V the perpendicular component of impact velocity.

This equation is almost exactly correct for an impact between two "semi-infinite" planes of liquid and solid. However, for drops or jets of finite size and/or curved leading surfaces, there will obviously be corrections related to droplet shape. In addition there are important corrections due to changing liquid properties, such as ρ and C, under the high pressures induced by the collision itself, as well as corrections due to the non-rigidity of the target material.

If the process were essentially "steady-state" as would be the case for the impact of an elongated jet (many L/D ratios), the pressure along the impacted surface would very quickly fall from water-hammer pressure magnitude to that of stagnation pressure (eq. A-2) if impact velocity is substantially less than acoustic speed of the liquid,

$$\Delta P_{st.} = \rho_o V^2/2 \qquad \text{(A-2)}$$

which is in general much smaller, but is the highest pressure attainable in a steady process. When V approaches C_o, ΔP_{st} is comparable to ΔP_{wh}.

2. Geometrical Effects

The perpendicular collision between flat semi-infinite liquid and solid planes is entirely analogous to the sudden deceleration of a liquid column in a "rigid" pipe, and hence the classical "water-hammer equation" describes the phenomenon correctly. However, the collision of finite flat or curved surfaces of liquid with a semi-infinite, rigid flat solid surface involves important differences. For a finite flat liquid surface, the effect of angle of impact

to analyze
is much more difficult, than the others, since the phenomenon is no longer "axially symmetric". Nevertheless, all of these situations have been investigated to some extent in our computer studies (1-7, eg.) as well as elsewhere. For simplicity, the present discussion will be limited primarily to our own work.

The situations here investigated for rigid flat surfaces include:

a) Spherical and combined flat and spherical shapes (Fig. 1)

b) Right circular cylinder impacting in direction parellel to axis

c) Conical droplet impacting in direction parallel to axis. This
y was chosen to allow the investigation of a constant contact angle of impact, as opposed to the situation with an impacting spherical drop, where the contact impact angle increases from zero to 90 deg. as the collision proceeds.

The spherical and combined flat-spherical shapes (Fig. 1) were investigated, since these shapes match most closely many actual droplet shapes in such important impingement cases as aircraft rain erosion and turbine wet steam erosion. Impact with the leading edge of a right-circular cylindrical drop was included to model as closely as feasible impact with elongated jets such as the liquid microjet originating from cavitation bubble collapse, as well as to provide a simple "limiting case" where acute contact angle effects which are present with spherical drops, are absent. Finally, the conical drop was investigated as another relatively simple (axially-symmetric) limiting case where an acute angle effect is present, but the angle is constant. This allows comparison with previous more simplified analyses which still take into account the contact angle effect (8, eg.).

In general, the effect of the contact angle, as for a spherical drop, eg, is to provide a non-uniform pressure distribution along the impact surface which reaches a maximum away from the axis and near the perimeter of contact, i.e., at increasing radius as the collision proceeds. While the water-hammer model (Eq. A-2) still provides a good approximation of the average pressure along the contact surface at any instant during the impact, the point pressure increases toward the outside of the contact region, and is a minimum along the axis (Fig. 2). According to our model, it exceeds the classical water hammer pressure only slightly. Some experimental information (Fig. 3) indicates that our calculation may be somewhat conservative in this regard, and that the actual peak pressure may be up to 1.5 x water-hammer pressure (9,10,eg). However, the difficulty of obtaining precise experimental information on this phenomenon is very considerable. Hence it must be admitted that the situation is not fully resolved at this time.

The time of application of the high pressures is extremely short. Figure 2 indicates non-dimensional times of less than unity. For water droplets of $\sim$1 mm radius, the units of this non-dimensional time are $\sim$1μs. Hence the degree of damage to be expected from such very transient stressing of the material is problematical. Also the conventional mechanical material properties cannot be expected to be valid for such high rates of loading, and the effective failure stresses may be much greater than expected.

Figure 4 depicts the surface pressures resulting from conical droplet impact. In this case also the maximum contact pressure moves outward as the collision proceeds, finally reaching a value

of $\sim$1.4 x water-hammer. Again the duration of the entire process is $\sim$1 μs for a droplet radius of $\sim$1 mm.

3. Bulk and Elastic Modulus Effects

a. General

Elastic modulus of the material impacted as well as bulk modulus of the liquid affect the results as well as the geometrical effects previously discussed. This point leads to the general conclusion that the results from the mathematical models here discussed depend only upon:

i) Mach number of impact (referred to liquid sonic velocity, i.e. V/C_o)

ii) Rigidity of impacted surface

iii) Geometry of collision, i.e., shape of impacting droplet and impacted surface. The absolute droplet size is not required, except for the eventual computation of absolute duration of effects. The resultant pressures are thus not a function of droplet size.

b. Bulk Modulus of Liquid

Any meaningful analysis of the liquid impact problem must obviously consider the liquid to possess a finite compressibility. An "incompressible liquid" model (infinite bulk modulus) would lead to a calculated infinite contact pressure of zero duration, since the liquid sonic velocity would then be infinite. Thus the "water-hammer model" requires a pressure wave speed, C in Eq. $^{A-1}$. For relatively weak water hammer, it is adequate to assume $C \cong C_o$ = sonic speed of liquid. However, this is not a good approximation for the impact case unless the impact liquid "Mach number" is very small, as is the case for

conventional water hammer. Eq. A-3 (Refs 2, 3, 8 , eg) shows the pertinent correction to C_o for water for impact velocities up to $\sim$4500 m/s. For impact speed of 300 m/s, i.e., liquid Mach number for water $\tilde{=}$ 0.2, the shock wave speed is $\sim$ 1.4 x the acoustic speed.

$$C/C_o = 1 + 2(V/C_o) - 0.1(V/C_o)^2 \text{---------} \quad (A-3)$$

A correction to density ρ_o must also be considered, but this is relatively unimportant except for very high impact Mach numbers.

c. Target Material Rigidity

The discussions above have all assumed a fully rigid flat material surface, although it is well known that finite target elasticity (or plasticity) will reduce somewhat the contact pressures, and hence also the stresses induced in the target material. As originally shown by DeHaller (11), the first-order correction for material elasticity is provided by Eq. A-4.

$$\Delta P = \rho_o C_o V/[1+(\rho_o C_o/\rho_s C_s)] \text{----------} \quad (A-4)$$

where ρ_s and C_s are the density and acoustic speed of the solid material, and their product is the "acoustic impedance". If the ratio of acoustic impedences between liquid and solid is appreciable, the reduction in impact pressure caused by the material elasticity effect can be large (Fig. 5).

The ratio of contact pressures between a collision of a liquid wi elastic solid and with a rigid solid (5) for the various cases here computed in detail, using a full mathematical model of the impact and assuming elastic response of the material, are shown in Fig. 5.

Spherical and cylindrical drops were considered with target materials of aluminum and plexiglass for liquid Mach number 0.2. Fig. 5 also shows the result from the classical DeHaller model (Eq. A-4) which appears to be somewhat conservative compared to the actual computer results, ie, calculations using the DeHaller model, will overestimate the contact pressures to some extent. It is noted that the reduction in contact pressure for aluminum (as compared to a rigid solid) for these cases is $\sim$ 15%, and for plexiglass $\sim$ 45%.

The computer calculations for Fig. 5 also provide the impact stresses and strains in the material as a function of position and time. These are reported in detail elsewhere (4-7, .eg), and will also be ıssed in a different section. However, this type of calculation can be made for any material and liquid impact situation. From such results meaningful estimates of the probability and type of material failure to be expected can be made. However, it is not yet possible to estimate from such results, the rates of material removal. Such an estimate would differ depending upon many factors such as type of material and material failure, importance of corrosion and other mechanisms, importance of very short term impact loadings ($\sim\mu$s) as opposed to conventional mechanical properties which are generally obtained under much slower rates of loading, and many other complicating factors.

B. Mathematical Models and Computer Analyses

1. General

The previous section has reviewed the general fluid-dynamic and material parameter interactions involved in the collision of a liquid jet with a solid material surface, i.e., the "physics" of the liquid-solid impact process. This section will review these processes in further detail, including the details of the numerical analyses which have been performed. The following section will consider the experimental and photographic results which have been obtained, and how these relate to theoretical and numerical predictions.

Liquid impact discussions in this book are limited to the intermediate velocity range by the scope of the book, the low to moderate subsonic range, as referred to sonic velocity of the liquid. This is the general range of interest for such phenomena as cavitation bubble collapse "microjets", steam turbine droplet impact, and aircraft rain erosion, i.e., the range up to about 1000 m/s. As it happens, the impact problem is of maximum complexity in this general velocity range, since none of the major governing fluid or material mechanisms can be here neglected. For very low velocity it is of course possible to completely neglect fluid and material elasticity, or "compressibility". For "hyper-velocity" impact, i.e., high supersonic range referred to liquid sonic speed, such as might be encountered with missile re-entry cone rain erosion, eg., micro-meteorite impact of space-craft, many fluid and material properties can be neglected. For example, a liquid and a solid become essentially identical under these circumstances, since the relative kinetic

energies of the collision greatly exceed material or liquid "binding energy" so that solid or liquid particles behave essentially as a highly compressible fluid. This general problem is attackable by computer techniques such as "PIC" ("particle-in-cell", ref. 12, eg.) which is generally limited to cases where fluid, or material, compressibility is substantial. Though such problems are beyond the scope of this book, it is interesting to note that for hyper-sonic collision even chemical energies may become negligible compared to the kinetic energies. Thus a collision with a small stone or an equal mass of TNT might be essentially equally damaging for such impact velocities.

2. Controlling Parameters for Moderately Subsonic Collisions

For the low to moderate subsonic liquid range here considered, the pertinent form of the fluid equation of motion is the "non-steady" form. It must as a minimum contain inertial and pressure terms. The inclusion of viscosity may or may not be necessary depending upon the relative value of various other parameters, but it is unlikely that gravity or surface tension need be included. The non-steady term is controlling during the initial portion of the collision. This is the portion important from the viewpoint of damage, where pressures of the general magnitude of "water hammer", rather than stagnation pressure, exist. For an elongated jet at least, the pressure later falls to the general magnitude of the stagnation pressure, as would generally be expected. The problem of steady-state jet impingment has generally

been solved classically, and is of course of much less complexity than the initial phase of jet impact, or of the droplet impact problem in general.

The conservation of mass equation applicable to the liquid impact problem in the moderate subsonic range must consider liquid compressibility. A "first-order" consideration of this factor is used in the conventional "water-hammer " analysis, originally proposed by St. Venant (13) and later by Cook (14). This results in the pressure calculation of Eq. A-1, and is often sufficient. However, as explained in Section A, correction to this relation for moderate subsonic liquid Mach numbers is required for good results.

While the complete neglect of liquid compressibility would lead to trivial results, i.e., infinite pressure for zero time, meangingful results will be obtained in many cases if only target material compressibility is completely neglected, i.e., the "rigid surface" approximation. However, depending upon the material-liquid combination and impact Mach number, target material elasticity and/or plasticity must also be considered to obtain reasonably accurate results. The points will be explained in greater detail in the following sections.

3. Detailed Pertinent Differential Equations for Impact Between Liquid and Rigid Solid

The detailed differential equations pertinent to the description of an axially-symmetric collision between a water droplet of otherwise arbitrary shape and solid surface follow. The degree of rigidity and precise shape of the solid surface, as well as the precise shape of the liquid droplet, enter the problem only through the boundary conditions, and hence do not

affect the basic differential equations. These, and numerical techniques pertinent to the axially-symmetric liquid-solid impact problem in the velocity range of interest, are best described by two Ph.D. theses recently completed here (1,4), and the subsequent publications (2,3,5-7, ,e.g.). For convenience, the equations and some of the other pertinent material will be summarized here.

Under the pertinent assumptions, the equations governing the impact between a liquid droplet of spherical or cylindrical shape and a rigid solid surface are written as follows.

The equation of continuity for the liquid phase becomes:

$$\frac{\partial \rho}{\partial t} + \frac{\partial(\rho u)}{\partial z} + \frac{1}{r}\frac{\partial(r\rho v)}{\partial r} = 0 \qquad \text{(B-1)}$$

The momentum equations for the liquid phase are:

$$\frac{\partial(\rho u)}{\partial t} + \frac{\partial(\rho u^2)}{\partial z} + \frac{1}{r}\frac{\partial(r\rho vu)}{\partial r} = -\frac{\partial p}{\partial z} \qquad \text{(B-2)}$$

$$\frac{\partial(\rho v)}{\partial t} + \frac{\partial(\rho vu)}{\partial z} + \frac{1}{r}\frac{\partial(r\rho v^2)}{\partial r} = -\frac{\partial p}{\partial r} \qquad \text{(B-3)}$$

A suitable form (1,4,15,eg.) of the equation of state for water (Tait's eq.) is:

$$\frac{p + B}{p_o + B} = \left(\frac{\rho}{\rho_o}\right)^A \qquad \text{(B-4)}$$

where u and v are the axial and radial velocity components respectively for the cylindrical coordinates z and r. Time t is another independent variable, and ρ and p are the fluid density and pressure. The values of the two constants in the equation of state for water are chosen (15) as:

$$A = 7.15 \qquad B = 3.047 \text{ kilobars}$$

Strictly speaking, the energy equation would also be required:

$$\frac{\partial(\rho E)}{\partial t} + \frac{\partial(\rho uE)}{\partial z} + \frac{1}{r}\frac{\partial(r\rho vE)}{\partial r} + \frac{\partial(pu)}{\partial z} + \frac{1}{r}\frac{\partial(rpv)}{\partial r} = 0 \qquad \text{(B-5)}$$

to complete the formulation, where $E = e + 1/2(u^2+v^2)$ is the specific total energy, and e is the specific internal energy. Since the main concern here is not energy transfer, the energy equation can usually be neglected for droplet impact analyses. However, it can be important in the particular case of stagnation temperature. While for impact in the velocity range here considered, liquid temperature rise due to the stagnation temperature effect is not great ($\sim$45°C for 600 m/s water) it may also not be negligible for certain considerations.

4. Pertinent Numerical Techniques

Various numerical techniques are possible for the solution of the differential equation set represented by Eqs. B-1 through 5. That named "ComCam" (Compressible Cell-and-Marker), developed here by Y. C. Huang (1-3,16, e.g.) was apparently the first and probably best known. The descriptions will thus consider particularly these studies. This program was somewhat modified and improved in the subsequent Ph.D. thesis of J-B Hwang (4-7, e.g.). The modifications were particularly concerned with the handling of the interface condition between liquid and solid. Hwang also (4,5, e.g.) included the effect of such resilient target solids as aluminum and plexiglass in his eventual very comprehensive program. Further details of his study of elastic target effects will be given in a later section.

Regardless of the numerical technique used for the analysis, it is also highly desirable to convert the equations into a non-dimensional form so that maximum applicability of the results

will be attained. This was of course done by both Huang (1-3 , 16,e.g.) and also Hwang (4-7 .,e.g.). The result was that pressure can be considered to be normalized by the conventional water-hammer pressure, velocity by sonic velocity, etc., so that it is eventually shown that for a fully rigid solid with water, the only independent parameters for the problem are impact liquid Mach number and droplet shape. The results in terms of non-dimensional time and position are then normalized pressure and velocity.

The method begins with an Eulerian grid. Field variables such as density and velocity are directly associated with the cells of the grid. In addition a series of Lagrangian "marker particles" are assigned to the liquid. These are necessary to mark the free surface movement. Numerical computation will start with particles located only along the surface. This is possible because fluid particles initially on the free boundary always remain on the free boundary (17). "CoM Cam" for Eulerian calculation then combines Eulerian and Lagrangian technqiues. In general, a modified 2-step Lax-Wendroff scheme (18) is used. It is not worthwhile to pursue the program details more fully here, since these can be found in full detail for those interested in the Ph.D. theses mentioned (1,4) and related papers. Full program listings are also given in these theses.

5. Dynamic Equations for Solid Materials(1,4 e.g.)

a. General

For a homogeneous isotropic elastic medium, the equations of motion are given by: (19-21, e.g.)

$$(\lambda + 2G)\nabla(\nabla\cdot\vec{u}) - G\nabla X\nabla X\vec{u} = \rho\frac{\partial^2\vec{u}}{\partial t^2} \qquad \text{(B-6)}$$

where $\vec{u} = \vec{u}(r, z, t)$ is the displacement vector, (not velocity here) and G I constants, and ρ the density. Written explicitly in terms of radial and axial components, $u_r(r, z, t)$ and $u_z(r, z, t)$, we have:

$$(\lambda + 2G)\left(\frac{\partial^2 u_r}{\partial r^2} + \frac{1}{r}\frac{\partial u_r}{\partial r} - \frac{u_r}{r^2} + \frac{\partial^2 u_z}{\partial r\,\partial z}\right) + G\left(\frac{\partial^2 u_r}{\partial r^2} - \frac{\partial^2 u_z}{\partial r\,\partial z}\right) = \rho\frac{\partial^2 u_r}{\partial t^2} \qquad \text{(B-7)}$$

$$(\lambda + 2G)\left(\frac{\partial^2 u_z}{\partial z^2} + \frac{1}{r}\frac{\partial v_r}{\partial z} + \frac{\partial^2 u_r}{\partial z\,\partial r}\right) + G\left(\frac{\partial^2 u_z}{\partial r^2} - \frac{\partial^2 u_r}{\partial z\,\partial r} - \frac{1}{r}\frac{\partial u_r}{\partial z} + \frac{1}{r}\frac{\partial u_z}{\partial r}\right) = \rho\frac{\partial^2 u_z}{\partial t^2} \qquad \text{(B-8)}$$

One of the Lamé's constants, G, is commonly known as shear modulus. The relations between Lamé's constants and Young's modulus E and Poisson's Ratio ν are as listed below.

$$\lambda / G = 2\nu/(1 - 2\nu)$$
$$G = E / 2(1+\nu)$$
$$\lambda = \nu E / (1+\nu)(1-2\nu)$$
$$\nu = \lambda / 2(\lambda + G)$$
$$E = G(3\lambda + 2G) / (\lambda + G)$$

Strain and stresses can be derived from displacements with following relations:

Strain

$$\epsilon_r = \frac{\partial u_r}{\partial r}, \quad \epsilon_z = \frac{\partial u_z}{\partial z}, \quad \epsilon_\theta = \frac{u_r}{r}$$

$$\gamma_{rz} = \gamma_{zr} = \frac{1}{2}\left(\frac{\partial u_z}{\partial r} + \frac{\partial u_r}{\partial z} \right) \qquad \text{(B-9)}$$

Stress

$$\sigma_r = (\lambda + 2G)(\epsilon_r + \epsilon_\theta + \epsilon_z) - 2G(\epsilon_\theta + \epsilon_z)$$

$$= (\lambda + 2G)\left(\frac{\partial u_r}{\partial r} + \frac{u_r}{r} + \frac{\partial u_z}{\partial z}\right) - 2G\left(\frac{u_r}{r} + \frac{\partial u_z}{\partial z}\right)$$

$$\sigma_z = (\lambda + 2G)(\epsilon_r + \epsilon_\theta + \epsilon_z) - 2G(\epsilon_r + \epsilon_\theta)$$

$$= (\lambda + 2G)\left(\frac{\partial u_r}{\partial r} + \frac{u_r}{r} + \frac{\partial u_z}{\partial z}\right) - 2G\left(\frac{\partial u_r}{\partial r} + \frac{u_r}{r}\right).$$

$$\sigma_\theta = (\lambda + 2G)(\epsilon_r + \epsilon_\theta + \epsilon_z) - 2G(\epsilon_r + \epsilon_z) \qquad \text{(B-10)}$$

$$= (\lambda + 2G)\left(\frac{\partial u_r}{\partial r} + \frac{u_r}{r} + \frac{\partial u_z}{\partial z}\right) - 2G\left(\frac{\partial u_r}{\partial r} + \frac{\partial u_z}{\partial z}\right)$$

$$\tau_{rz} = \tau_{zr} = 2G\,\gamma_{rz} = 2G\,\gamma_{zr} = G\left(\frac{\partial u_z}{\partial r} + \frac{\partial u_r}{\partial z}\right)$$

The elastic half-space is originally at rest. Thus, we have the following initial conditions:

$$u_r(r, z, 0) = u_z(r, z, 0) = 0 \qquad \text{(B-11)}$$

Boundary conditions on the axis of symmetry ($r = 0$) are:

$$u_r(0, z, t) = 0 \qquad \text{(B-12a)}$$

$$\frac{\partial u_z}{\partial r}(0, z, t) = 0 \qquad \text{(B-12b)}$$

b. Calculational Procedure

For each time step of the numerical calculation, the response of the liquid phase is calculated first using the shape and velocity of the solid surface at the beginning of this time step as boundary conditions on the interface. The new surface shape and velocity are then calculated using Eqn. B-7 and B-8, assuming that the pressure distribution just calculated in the liquid phase is being applied through this time step. The response of the liquid phase is then refined using the new surface shape and velocity. This trial and error procedure is performed until the surface shape and velocity from two consecutive iterations are judged to be sufficiently close.

The necessary conditions for the liquid-solid interface, during the early stages of the impact, are the continuity of displacement and velocity. The liquid pressure is the only load on the solid surface. Liquid and solid must have the same normal displacement and velocity, if they are to remain in contact. Mathematically, these boundary conditions are:

$$\sigma_z(r, 0, t) \leqq -p\left[r, u_z(r, 0, t), t\right] \tag{B-13}$$

$$\sigma_r(r, 0, t) \begin{cases} = 0 & \text{if full-slip} \\ \leqq -\mu \dfrac{\partial v_r}{\partial z}\left[r, u_z(r, 0, t), t\right] & \text{if no slip} \end{cases} \tag{B-14}$$

$$v_z(r, Z_{int}, t) \leqq \frac{\partial}{\partial t} u_z(r, 0, t) \tag{B-15}$$

$$\begin{cases} \dfrac{\partial}{\partial z} v_r(r, Z_{int.}, t) = 0 & \text{if full slip} \\ v_r(r, Z_{int}, t) \leqq \dfrac{\partial}{\partial t} u_r(r, 0, t) & \text{if no slip} \end{cases} \tag{B-16}$$

$$\frac{\partial}{\partial z} p(r, Z_{int}, t) = 0 \tag{B-17}$$

where $Z_{int} \equiv u_z(r, 0, t)$ is the axial displacement of the solid

surface. Arrows in the equations denote how, in the iteration discussed earlier, the quantities in one phase are fed into the other phase.

Equations for liquid and solid phases will be non-dimensionalized separately in sections d. A dimensionless quantity (with superscript *) is defined as the quotient of a physical quantity and a corresponding characteristic value (with subscript c) whose selection will be discussed whenever the choice become clear

c. Non-Dimensionalization of Liquid Equations

The following dimensionless quantities are defined for the liquid phase:

$$t_L^* = t / t_{cL}, \qquad \rho^* = \rho_L / \rho_c ,$$

$$r^* = r / r_c , \qquad z^* = z / z_c ,$$

$$R^* = R / r_c , \qquad Z^* = Z / z_c ,$$

$$p^* = p / p_c , \qquad B^* = B / p_c ,$$

$$v_r^* = v_r / v_c , \qquad v_z^* = v_z / v_c$$

d. Non-Dimensionalization of Solid Material Equation

The following dimensionless quantities are introduced for the solid material:

$$u_r^* = u_r / u_c, \quad u_z^* = u_z / u_c, \quad t_s^* = t C_l / R_o \qquad \text{(B-18)}$$

where $C_l = \sqrt{(\lambda + 2G)/\rho_s}$ is the longitudinal wave velocity for the solid.

Non-dimensionalized forms of Eqn. B-7 and B-8 are

$$\frac{\partial^2 u_r}{\partial r} + \frac{1}{r}\frac{\partial u_r}{\partial r} - \frac{u_r}{r} + \frac{\partial^2 u_z}{\partial r \partial z} + \frac{G}{\lambda + 2G}\left(\frac{\partial^2 u_r}{\partial z^2} - \frac{\partial^2 u_z}{\partial r \partial z}\right) = \frac{\partial^2 u_r}{\partial t^2} \qquad \text{(B-19)}$$

$$\frac{\partial^2 u_z}{\partial z^2} + \frac{1}{r}\frac{\partial u_r}{\partial z} + \frac{\partial^2 u_r}{\partial r \partial z} + \frac{G}{\lambda + 2G}\left(\frac{\partial^2 u_z}{\partial r^2} - \frac{\partial^2 u_r}{\partial r \partial z} - \frac{1}{r}\frac{\partial u_r}{\partial z} + \frac{1}{r}\frac{\partial u_z}{\partial r}\right) = \frac{\partial^2 u_z}{\partial t^2} \qquad \text{(B-20)}$$

6. Results of Numerical Analyses

While full details of these numerical analyses are given elsewhere (1-7,e.g.), the more important results will be summarized here, as well as results from other related analyses.

a. Droplet Geometry Effects (Rigid Flat Surface)

1) General

As discussed in Section A, detailed fluid-dynamic behavior during a liquid droplet collision with a rigid flat plane depends heavily upon geometrical considerations such as droplet shape and angle of collision. It is somewhat less sensitive to the only other independent parameter involved (aside of course from various liquid properties), i.e., impact liquid Mach number. While the classical "water-hammer pressure" (Eq. A-1) provides a good preliminary estimate of the maximum interface pressure attained during the collision, substantial detailed variations, both positive and negative, from this estimate exist, as discussed briefly in Section A. Since maximum pressures and velocities only are generally of interest from the viewpoint of erosion, which is the major practical interest in the collision process, it is only the very initial portion of the collision that must be considered. In fact, within a very few microseconds, the surface pressure falls for a droplet of 1 mm radius from the order of water hammer pressure to that of stagnation pressure, as will be shown in detail from the results of the numerical studies previously discussed (1-7,eg.).

For relatively very low velocities such as might be typical of pipe-line water-hammer problems, the stagnation pressure is negligible from the viewpoint of damage, while the water-hammer pressure is of course important. However, the ratio between

these pressures decreases for increased velocities. Figure 6 shows this ratio as a function of both impact liquid Mach number and velocity (7) for water. Equation B-1 is pertinent:

$$\Delta P_{WH}/\Delta P_{stag} \cong 2/M_o + 4.0 \qquad \text{(B-1)}$$

where $M_o = V_o/C$.

As noted there, the ratio approaches infinity for very low impact velocity, but 4.0 for very high velocity. In the usual range of interest for the droplet impact problems here considered, the ratio is in the range 5-10.

2) Spherical Droplet Impact

Impacting liquid droplets encountered in most pertinent situations can be reasonably well modelled by a spherical drop, which can also well simulate the leading edge of a liquid jet. Figure 7 shows the shape history of an initially spherical water drop after impact at liquid Mach number 0.2 ($\sim$300 m/s), as calculated by Hwang (4-7, e.g.). The droplet deforming process is also very similar to that previously computed by Huang (1-3 ,e.g except that the liquid surface adheres somewhat more closely to the plate. Differences between the Huang and the Hwang studies were somewhat for cylindrical droplets, as discussed later

Figure 8 shows the pressure distribution on the rigid plane ($z = 0$) at several instants after the initial contact. Maximum pressure occurs initially at the center of the contact area, but shifts to the edge after $C_o t/R_o = 0.2$. Pressure decreases rapidly at the center after reaching a peak value of $0.7\ \rho_o C_o V_o$. The maximum pressure travels radially outward as the solid-liquid contact progresses in this direction. The peak pressure for the entire process is $\sim 1.0\ \rho_o C_o V_o$, and occurs along a circle of half the initial droplet diameter at $C_o t/R_o = 0.7$. At

the maximum time investigated ($C_o t/R_o$ = 2.5), the pressure is everywhere approaching the stagnation pressure, as would be expected. Note that to a first approximation $\Delta P_{stag}/\Delta P_{WH} \tilde{=} M_o/2$.

The occurrence of peak pressure at a location other than the center is consistent with recent experimental findings. The computed distribution of maximum pressure is shown in Fig.3 along with measurements by Rochester and Brunton (22, 23) and by Johnson and Vickers(24). These curves show qualitative rather than quantititative agreement, since the physical situations differed to some extent. Rochester and Brunton (22) projected a solid projectile against a 5 mm diameter water "disc", rather than against a sphere as considered in our calculation. The impact liquid Mach number was only 0.07 rather than 0.2 for our calculation. Since the experiment used a 2-dimensional rather than the 3-dimensional geometry of our calculation, it is probable that the pressures measured would be greater, since the degrees of freedom for the escape of the liquid entrapped in the collision area are greater. Figure 3 shows that this was in fact the case. Heymann's earlier analysis (8,e.g.), which also predicted higher pressures was also for a 2-dimensional situation. While his analysis does not provide the pressure distribution, it predicts an edge pressure of 2.8 $\rho_o C_o V_o$ for an impact liquid Mach number of 0.2, as used in our calculation. Thus its "coefficient" is much higher than for all other analyses or experiments. Heymann predicted this maximum pressure would occur at a radius of 0.1 R_o.

Johnson and Vickers (24) measured the impact pressure for an approximately cylindrical water jet fired against a flat surface, so that their geometry differs considerably from our analysis. In their case, the pressure spreads over a relatively large area because the leading portion of their mushroom-shaped jet (shown schematically in Fig. 9) has a considerably larger radius than that of the jet body, R_o upon which Fig. 3 is based, since no accurate information on the jet leading edge geometry exists. Their liquid jet Mach number (~ 0.0 was much less than that of either our calculation or the Rochester-Brunton measurement.

Engel (25) examined the damage marks on rubber coatings bonded to metallic bases produced by 2 mm diameter water drops at 450-800 m/s ($M \cong 0.3$ to 0.53). She suggested that peak pressure developed when the contact area radius reached 0.5 R_o. This result agrees well with our calculation.

Figure 10 shows the pressure distribution on the axis of symmetry at several instants after impact. In general the pressure magnitude decreases for greater distances from the impact surface during the early portion of the process, and is always well less than water-hammer pressure at the axis. Figure 11 depicts the pressure transient at various locations on the plane. Very rapid pressure rise-rates are indicated immediately following impact, but these very rapidly decay to a relatively steady value of $\sim 0.1\ \rho_o C_o V_o$. The "coefficient" is, as would be expected about that indicated by the ratio $\Delta P_{stag} / \Delta P_{WH} = M_o/2$, since

M_o = 0.2 for these calculations.

Figure 12 shows radial velocity on the liquid-solid interface at several instants after collision. Maximum radial velocity, occurring near the edge of the contact area throughout the impact process, exceeds twice impact velocity, as also confirmed photographically (26, 27, eg.). The existence of a radial velocity substantially greater than impact velocity is explicable, since this is actually a "spouting velocity" from a region of essentially water-hammer pressure which, as previously explained, substantially exceeds stagnation pressure.

Figure 13 shows lines of constant pressure, as function of water-hammer pressure, within an impacting spherical drop (1-3, e.g.). It is noted that the complex interplay of pressure and reflection waves results in predicted regions of negative pressure, where presumably cavitation might occur. Photographic evidence of such cavitation has been obtained by Brunton (27) at locations quite similar to those predicted by our calculation (Fig. 14).

3) Cylindrical and Composite Droplet Impact

Cylindrical droplet impact moving parallel to its axis was studied by both Huang (1-3, e.g.) and Hwang (4-7, e.g.), primarily because it represents the simplest case possible after the one-dimensional case of the collision between liquid and solid semi-infinite planes. Also a complex droplet shape composed of a central cylindrical section surrounded by spherical segments can be envisioned (Fig. 1). By suitable choice of the controlling parameters, the computer program can be arranged to consider

either purely spherical, purely cylindrical, or composite droplet shapes. Such composite droplets (Fig. 11) probably represent real droplet or jet impact more closely than either purely cylindrical or purely spherical shapes.

Figure 15 depicts the cross-section of an initially cylindrical drop (L/D = 1.0) at several instants after collision with a rigid plane. The top of the cylinder remains flat until $C_o t/R_o$ = 1.6, which is ~1 μs for a 1 mm radius water drop. During this period the drop also begins to spread radially along the contact surface, giving rise to the high radial velocities generated by such collisions.

Figures 16 and 17 show the pressure distribution on the liquid-solid interface and on the axis of symmetry respectively at different instants after initial contact. As opposed to the spherical droplet collisions already discussed, the contact pressure at the axis substantially exceeds the classical water-hammer pressure, $\rho_o C_o V_o$ primarily because of the increase in C during the collision. This effect would of course increase for higher impact liquid Mach number than that here computed (0.2). However, for cylindrical impact there is no increase of contact pressure away from the origin as for the spherical case, except at the end of collision (Fig. 16). Rather (Fig. 16) the pressure attenuates, radially as would be normally supposed. Also, eventually the pressure becomes negative near the center giving rise to the possibility here of cavitation, as discussed already for a spherical drop.

Figure 17 shows the propagation of the "shock wave", ie, strong pressure gradient, into the interior of the droplet. The propagation speed is relatively constant up to non-dimensional time, $C_o t/R_o = 0.5$. Thereafter it decreases somewhat. The wave front attains significant thickness due to existence of a "finite mesh size" and "artificial viscosity", both features of the numerical procedure used. "Artificial viscosity" is useful to stabilize the numerical calculation, and also to give the capability of modelling to some extent the effect of real liquid viscosity, especially for highly viscous liquids, where this effect might become important. At $C_o t/R_o = 1.6$ the pressure becomes negative over most of the axis, even falling below the presumed tensile strength of water ($\sim$270 bar, see ref. 28, 29, eg) for impact velocity = 300 m/s (liquid Mach number 0.2). This could of course lead to local cavitation, as previously discussed, during droplet impact. Such cavitation could augment the erosion often associated with droplet impact. Calculations by Huang here (1-3, eg.) and Glenn elsewhere (30), also showed negative pressure on a rigid wall as well as inside a cylindrical drop. Also, as previously mentioned, there is photographic evidence (27) of cavitation within an impacting liquid disc.

Figure 18 shows the pressure at selected locations as a function of time. The peak pressure propagates into the droplet with a speed of $\sim 2.5\ C_o$, and is sustained for a non-dimensional time of ~ 0.8, which yields ~ 0.5 μs for $R_o = 1$ mm. Considering our definition of non-dimensional time, $\tau = C_o t/R_o$, actual duration, t is proportional to droplet radius, and inversely proportional to sonic velocity in the liquid.

Figure 19 shows the radial velocity along the liquid-solid interface at different instants. This is much greater near the edge of the contact

area than elsewhere. As previously mentioned in connection with spherical droplets, the maximum radial velocity is several times the original impact speed. This also has been confirmed photographically (26,27,eg.), as previously mentioned.

Table 1 summarizes the results of the computer calculations discussed in the foregoing, comparing the effects of droplet geometry and material rigidity, all for liquid impact Mach number of 0.2 upon flat semi-infinite planes. It is there shown that the maximum pressure is greater for the cylinder than for the sphere, and is of course greater for a rigid solid than otherwise, to be discussed later. Also, according to the present results for liquid Mach 0.2, it never exceeds very substantially the classical water-hammer pressure, and in fact may be considerably less than that for the non-rigid materials investigated. For higher liquid Mach number, the classical water hammer pressure can be substantially exceeded primarily because of the increase in liquid shock wave speed under the compressed condition.

4) Conical Droplet

While maximum pressure occurs at the axis for a cylindrical drop, it occurs near the edge of the contact surface for a spherical one. This outward movement of the maximum pressure point is associated with the expanding contact area caused by the curved liquid leading surface. To investigate this situation under somewhat simpler conditions, ie, constant contact angle between liquid and solid, a conical droplet shape (at the suggestion of F. J. Heymann) was investigated (4,6). Figure 20 depicts the shape history of this droplet and Fig. 4 the pressure distribution at several instants. For this case the peak pressure increases linearly with radius up to 0.8 R_o, after which the pressure reduces, presumably due to the termination of the conical surface. The maximum

pressure attained was $\sim 1.4\ \rho_o C_o V_o$, about the same magnitude reached with a cylindrical drop (Table 1). A direct comparison with Heymann's (8,eg.) predicted "coefficient" of 2.8 was not possible because our conical angle of 14°, chosen to simplify the computer problem, is greater than his predicted critical angle. However, no theoretical or experimental information indicates the likelihood of a coefficient at M = 0.2 greater than $\sim$1.5 (Table 1 and Fig. 4).

Radial velocity again has a maximum near the outer edge of the contact surface, reaching maximum values similar to those attained for the other droplet shapes.

The distribution of maximum pressure here calculated shows excellent agreement with the experimental data of Johnson and Vickers (24). The different distribution near the axis (Fig. 20) can be attributed primarily to the different droplet geometries. While our calculation is for a conical droplet shape, the leading edge of their jet is smooth and flat at the center (Fig. 9).

5) Material Rigidity Effects

As previously discussed, the inclusion of non-rigid material properties in the computation, results in reduced maximum pressures during the collision (Table 1). The relative importance of this effect is best estimated by Eq. A-4, where the "acoustic impedence ratio" between liquid and solid is considered. For fixed liquid properties, the effect obviously becomes of increased importance roughly as the product ρE of the material is reduced. Thus, as would be expected, the impact pressure reduction for aluminum, and especially plexiglass, is much greater than for steel. For this reason, we have computed the effect only for these materials (Table 1).

Figure 5 shows the reduction in maximum surface pressure due to surface elasticity as a function of acoustic impedance ratio between liquid and solid. Our computed points for cylindrical and spherical drops upon aluminum and plexiglass (PMMA) with water impact at 0.2 liquid Mach number are shown, as well as the curve predicted by the DeHaller-model (Eq. A-4). The DeHaller relation (11) provides a reasonable engineering approximation which is always conservative, i.e., it overestimates the surface stresses and pressures.

The transient surface displacements for aluminum are indicated in Fig. 21. The center displacement is a maximum at $C_o t/R_o \tilde{=} 0.5$, but then rebounds rapidly. Figure 22 shows the surface shape at several instants after the initial contact, while Fig. 23 shows a typical distribution of principal stresses. Stresses are normalized by $\lambda + 2G$ whose value for aluminum is 1.12×10^5 MN/m^2. Tensile stress (Fig. 24) on the surface first occurs outside the contact area, reaching a maximum value of 140 MN/m^2

(15,600 psi) at $C_o t/R_o \simeq 0.5$. The position of maximum tensile stress then shifts outward gradually before starting to decay at $C_o t/R_o \simeq 0.70$. A somewhat larger tensile stress (168 MN/m^2 = 18,700 psi) was reached within the body near the axis at $C_o t/R_o = 0.63$. The maximum compressive stress (Fig. 25) is much larger, reaching a value of ~ 900 MN/m^2 ($\simeq$ 100,000 psi) on the surface near the axis. Figure 26 shows the distribution of shear stress at a given instant. The maximum attained is 390 MN/m^2 = (43,500 psi). It occurs near the axis and decreases with radial distance. Such stresses could certainly cause failure to many aluminum alloys in one impact (300 m/s), and to many other alloys through eventual fatigue mechanisms.

6. Other Numerical Studies

Many of the pertinent droplet impact numerical studies have been done in the author's laboratory at Michigan, and these have been emphasized in the foregoing, since they form the most unified comprehensive group of such studies available to the author's knowledge. Earlier pre-computer analyses have only been mentioned when they appeared particularly pertinent to the discussion, since they do not particularly add to the present understanding of the subject. However, there are several relatively isolated computerized studies (30-36, eg) which are generally consistent with our results here discussed, but which should be included for the sake of completeness.

Several very new studies regarding variations of the original problem have been reported by G. R. Johnson (34-36). These include the generation of a new and improved computer program involving triangular, rather than rectangular, computing elements (34), and impact-induced severe elastic-plastic deformations (35,36), while previous work (4-7,32,33,eg.) had concentrated on small and elastic material responses.

C. EXPERIMENTAL AND PHOTOGRAPHIC STUDIES

1. General

Section B has considered in detail the governing relations as well as computerized models applicable to the liquid droplet impact problem for the subsonic range of liquid Mach numbers which apply to most problems of engineering interest. The effects of material elasticity have also been included, as well as some comparisons with experimental data. This section will consider all pertinent basic research experimental and photographic studies so far as is possible, in order to illustrate the research state of the art for this range of phenomena, and the degree of agreement achieved between prediction and experiment.

2. Impact Surface Pressures

a. General

Experimental investigations of liquid-solid impact phenomena have involved many facets. From the viewpoint of hydrodynamics, efforts have been made to measure the impact pressure, and to obtain high-speed photography of the impact process. As to its damaging effect on solid materials, there have been experiments to study the damage patterns, and thus learn something of the surface pressures and velocities which may have produced the damage.

A high relative velocity between solid and liquid is obviously required for droplet impact studies. This can be achieved either by propelling the liquid droplet or jet toward the material surface to be eroded, or by propelling the solid material toward a relatively stationary droplet, or through a droplet environment, as , e.g., an artificial rain regime. Due to problems of droplet instability, sometimes described in terms of a critical Weber number, it is usually not possible to propel a spherical

droplet of sufficient size and at sufficient velocity to model conditions of interest. However approximately spherical droplets of $\gtrsim$ 1 mm diameter are characteristics of such real-life applications as steam turbine blading droplet erosion, and aircraft or missile rain erosion. Also, droplets of known and regular geometry are required so that meaningful comparisons can be made with the results of numerical computations such as those described in the previous section.

Due to the instability of high-velocity liquid droplets, in general, experiments take the form either of impact between high-velocity solid targets and essentially stationary droplets, or impact between projected liquid slugs of relatively undetermined or non-spherical geometry, and a stationary target. A common form of such jet, which has been used for many studies, has a relatively "mushroomed" shape leading edge (Fig. 9) as previously discussed in connection with the Johnson and Vickers experiment (24). Typical experiments wherein the droplet has been propelled toward a stationary target are described in ref. (9,37-39,eg) and for impact with liquid environments such as artificial rain, ref. 40,41, eg. References 42-44, eg. consider cases where high velocity liquid jets are fired toward stationary targets.

b. Specific Investigations

Engel (25,45,46,eg) has made extensive studies of water drop collision with solid surfaces, and was one of the first to study this particular problem from the viewpoint of aircraft rain erosion. Her experiments included starch-iodide tracer for radial liquid flow, high-speed photography and Schlieren pictures of the collision process, oscilloscope traces from high-response-rate pressure transducers, observation of time

dependence of the droplet radius and flow velocity, and splash patterns as a result of water drops impacting surfaces with different degrees of resilience. Collision velocity was controlled by the height of liquid fall, so that this particular set of experiments was limited to quite low impact velocities (~10 m/s).

Jenkins and Booker (37-38) studied the impact process of a water drop and a surface moving at high speed by firing a projectile at a water drop suspended on a fine web. High speed shadowgraph and streak photography were used to determine the splash shape and radial velocity respectively. Radial velocity for 1000 ft./sec. impact was found to be ~3400 ft./sec.

Brunton and others at the Cavendish Laboratory of Cambridge University have made many important contributions over the years. For instance, Hancox and Brunton (43) studied the deformation of solids by liquid jet impact. Specimens mounted on a high-speed rotating disc impacted a relatively low velocity water jet streaming parallel to the axis of rotation of the disc. The location where appreciable radial flow commenced was estimated from the distribution of shear pits on the surface. They found the contact angle between liquid surface and solid at which radial flow started was ~17° over a range of jet diameter and velocity. The impact load was measured using a barium-titanate pressure transducer which replaced the specimen for these runs.

Brunton and Camus (44) examined the secondary flow processes within an impacting drop and found cavitation to exist on the liquid-solid interface and inside the drop. Cavitation induced within impacting droplets has been also discussed elsewhere in this book, and was in fact predicted by our computer models in this laboratory[45] and elsewhere (46). Collapse of the cavitation bubbles (44) produced measurable shock waves

and estimated liquid collapse velocities greater than the initial impact velocity.

Rochester and Brunton (39) measured the distribution of maximum impact pressure and shear stress on the interface between a water drop and a solid surface. An oblong-shaped "bullet" with a flat front surface was fired against a 5 mm diameter water disc suspended between two perspex plates. A very small piezoelectric ceramic was mounted on the front surface to measure local pressures and shear stresses. The results of this work have already been discussed herein for comparison with our computer model results. With impact velocity of 100 m/s, maximum pressure was 1.8 $\rho_o C_o V_o$, and occurred 0.5 mm from the axis. Pressure at the center was $\sim 0.7\ \rho_o C_o V_o$. The maximum in measured pressure coincided with the position of the edge at the instant outward jetting began. Contact angle at this point was $\sim 11°$ over a range of droplet diameters.

Johnson and Vickers (24) also measured the transient normal and shear stress distributions, in their case caused by perpendicular and inclined impact of water jets against nominally rigid surfaces. Their liquid jet was $\sim$ 50 mm diameter with impact velocity of 46 m/s. They found a maximum normal stress of $\sim 1.5\ \rho_o C_o V_o$ along a circle of the same radius as the impacting jet. This result differs from Rochester and Brunton (39), who found the maximum pressure relatively much closer to the axis. Johnson and Vickers (24) found maximum shear stress to be $\sim 0.45\ \rho_o C_o V_o$ along a circle of 0.9 jet radius.

One can tentatively conclude from these results, and our computer model, which is in approximate agreement as previously discussed, that:

i) The classical water hammer pressure $\rho_o C_o V_o$ provides a relatively good engineering approximation for the impact pressure between a liquid curved surface and a flat solid plate.

ii) The instantaneous pressure during the start of impact exceeds

this value by a factor of ~1.5. While the exact value of this "coefficient" is somewhat in doubt at the moment, it apparently does not exceed 2, as Heymann's earlier approximate analysis (8) had suggested.

iii) The jetting velocity is several times the impact velocity.

iv) The duration of pressures in excess of the classical water hammer pressure for droplets of the diameter range 1-3 mm (which are of practical interest) is very short, probably only a fraction of a micro-second. Hence its damage-creating capability is in doubt.

3. Material Deformation, Stresses and Damage from Liquid Impingement

The group at Cambridge University has also contributed very importantly to the study of surface damage due to liquid impingement. For example, Bowden and Brunton (49) and Bowden and Field (50) reported on the development and use of a momentum-exchange water gun device, which has since become quite classic in the field. Modified versions have since been used in many laboratories including our own. Their water gun, as originally reported, produced a jet velocity of up to ~ 1200 m/s, with a jet of ~ 2 mm diameter. These investigations have combined the bombardment of surfaces with such jets with ultra-high-speed photography (order of 10^6 f/s). They thus confirmed the very short duration of the high-pressure portion of the impact (few microseconds for droplets of a few mm diameter). The elongated jet produced by these water guns (Figs. 27 and 28) is typically preceded either by a small "Monroe jet" (49,50, eg.) at a velocity somewhat higher than that of the main jet, or by a mushroom-shaped leading edge (Fig. 9) which shows a schematic representation of this jet form). The actual form of jet obtained depends upon the position of the meniscus of the water slug in the nozzle prior to firing. (49,50, eg.). A concave-inward meniscus produces a Monroe-jet, which is quite analogous to the explosive jet produced by

an armor-piercing "shaped-charge" ("Bazooka" of World War II), and represents a technique previously used in mining.

As a result of the above and related work at Cambridge, numerous details of the form of surface failure for various materials were observed. In summary, the following features were observed:

i) Circumferential surface fracture,

ii) Subsurface flow and fracture,

iii) Large-scale plastic deformation,

iv) Shear deformation around the periphery of the impact zone,

v) Fracture due to the reflection and interference of stress waves.

Hancox and Brunton (43) studied the damage of solids by multiple low-velocity impact (~40 - 180 m/s) of liquids using a wheel and jet apparatus previously discussed. They followed the development of erosion damage with increasing numbers of impacts (as have various other investigators) for several materials of different characteristics, and studied the influence of impact velocity, grain size, surface roughness and other parameters on erosion damage.

Other investigations have considered much higher velocity ranges typical of the aircraft rain erosion problem. It is unnecessary to attempt to review very many of these here. However, as typical examples, Schmitt and colleagues (40,51,52,eg.) performed a comprehensive investigation of a large number of plastic, ceramic, metallic and composite materials for short-time exposure rain erosion resistance at velocities of 1.5, 2.0, 2.5, 3.0 and 4.0 times the sound speed of air, i.e., these values can be considered as conventional atmospheric air Mach numbers. Specimens for these tests were mounted on multistaged rocket sleds fired down a track through an artificial rain field at Holloman Air Force Base. The application of interest was of course aircraft and missile component

rain erosion.

Studies of the high-velocity liquid impact erosion resistence of various materials under different conditions also have been performed in various laboratories using either rotating arm or disc devices, or liquid jet guns, usually essentially modifications of the original Bowden-Brunton (49, eg.) momentum exchange gun device. Typical results of such experiments are shown in Fig. 29. . Aluminum (Type 1100-F) and nickel (Type 270) were tested in our laboratory using a repeating water jet gun, of a design originated by Kenyon (53), but producing jets very similar to those of the Bowden-Brunton device. This device (54,eg.) can produce ~2 mm diameter jets of up to 600 m/s velocity. For the present tests (Fig. 29), impact velocities were 400 and 600 m/s. The typical "incubation period" is shown with little mass loss, but noticeable surface deformation.

4. Impact Between Liquid Drop and Elastic Half-Space

It is generally believed at present that most ductile materials fail in shear and brittle materials in tension. However, it also appears possible that ductile behavior is relatively suppressed here because of the very high rate of loading in both impact and cavitation. For this reason, as discussed under cavitation damage, brittle fractures seem to predominate, and the best correlation between erosion rate and mechanical properties is achieved with "ultimate resilience," i.e., "strain energy to failure " if failure is in the brittle mode.

When ductile solids are subjected to impact by a high-velocity object, or otherwise induced impulsive pressure, the deformation can be categorized as follows:

i) Elastic

ii) Elastic plus plastic

iii) Hydrodynamic, i.e., viscous

For elastic deformation (category i) there is no apparent damage after impact, whereas for category ii) a permanent deformation occurs. In iii) the combination of materials properties and impact conditions is such that the solid responds as a viscous fluid. This occurs primarily in "hypersonic impact" as, eg., collisions between meteoroids and spacecraft. This type of collision is not of concern for most other types of engineering applications.

For many engineering applications where liquid-solid collisions are important, eg., wet steam turbines, permanent damage does not start until after a considerable period of initial exposure, usually termed the "incubation period," as shown in Fig. 29. For such cases, permanent damage does not start until stress hardening and other related processes have degraded the surface resistance of the material considerably. The solid material can be reasonably considered as an elastic medium during this incubation period.

The duration of the incubation period of course is related to the strength and duration of the impact pulse (55). If this is too short, there is insufficient time for appreciable material flow due either to shear or normal stresses, so that many materials withstand elastically momentary stresses much greater than their static (conventional) yield stress would indicate. Under these conditions, ductile materials may fail in a brittle mode as previously mentioned.

Fractures of brittle materials originate at inherent flaws, and propagate with finite speed along the surface of principal tensile stress. If the impulse duration is too short, cracks may not be able

to expand enough to become significant. However, regardless of the nature of deformation, detailed information on the stress distributi is needed for predicting the location and cause of failure. As a first approximation, the elastic deformation assumption can best be used.

Bowden and Field (50) suggested and verified that small cracks surrounding the main ring fracture of brittle materials were initiat by Rayleigh surface stress waves. While this simple model appeared to hold true for thick materials, they found also that the reinforce of reflected longitudinal and transverse waves with Rayleigh surface waves caused further localized cracks.

Blower (56) assumed the impact of a spherical liquid to be equivalent to a constant uniform pressure $\rho_o C_o V_o$ over a circle whose radius increased in proportion to the square root of time. He then solved the elastic wave equations by a Laplace transform technique, and obtained in closed form the transient surface stress and deforma distribution for a homogeneous isotropic elastic half-space, with Poisson's ratio equal to 0.3. He showed that a Rayleigh surface wave would appear at the moment when the radius of the loaded area is increasing with the Rayleigh wave speed. Behind the Rayleigh wave front, he found an abrupt transition (singularity) which caused extreme radial and azimuthal tensions. Since their duration was extremely short, he did not think them responsible for the observed liquid impact erosion, as Bowden and Field (50) had suggested.

Peterson (57), based on results of Huang (1-3, eg.) here and Tyler (31) elsewhere, assumed as a first approximation that the impact pressure could be represented by a quasi-static, hemispherical distribution over a circular area. He then applied Love's solution (58), i.e. Hertz contact stress, to obtain the stress distribution in a semi-infinite homogeneous elastic solid. The maximum impact pressure, which would then occur at the axis, was determined by one-dimensional Rankine-Hugoniot relations. He found the principal compressive stress to be greatest on the surface at the axis. Shear stress was maximum at 0.45 R_o below the surface along the axis, where R_o is the radius of the loaded area. Obviously, however, this model does not include surface shear stress along the surface induced by the impact-induced high radial velocity previously discussed. Some investigators have attributed a portion of the damage to this feature. However, simple calculations made by the present author indicate that fluid-induced surface shear ($\tau = \mu \partial u/\partial y$) is not likely to be important in the damaging process. Of course, liquid impact of the radial velocity against surface asperities may generate a substantial portion of the water-hammer pressure, which might then obviously contribute significantly to the damage. According to the Peterson analysis (57), the surface under the impact area, i.e., area of his hypothetical imposed load, will be subjected only to compressive stresses, and thus should remain relatively undamaged. On the other hand, he found (57) that surface tensile stresses immediately outside the loaded area would be sufficient to initiate circumferential cracks in certain materials. Photographs of impact damaged surfaces, discussed elsewhere, verify this conclusion.

Blower's assumption (56) for the expansion rate of the loaded area agrees quite well with numerical results (1,2,4-7,eg.) for the impact of a spherical drop and a semi-infinite solid body. However, his assumption

of constant and uniform pressure does not agree well with our calculations, or other measurements. The weight of evidence now confirms the existence of high edge pressures for the impact of a spherical drop. Experiments of Goodier et al (59) on the impact of a steel ball with an elastic

half-space with impact velocity to 6,000 m/s showed the measured duration of contact and force-time relation agreed well with the prediction of the Hertz contact theory (58) used by Peterson (57). Use of the Hertzian approach for liquid-solid impact, however, is much more limited because liquids are far from elastic over the pressure range involved, and pertinent static force-deformation relations are lacking. Further, the duration of the high-pressure portion of usual liquid-solid impacts is only a few microseconds, whereas that for solid-solid impact, for which the Hertz contact theory was derived, are typically much longer, i.e., order of 100 microseconds.

Typical results from our calculations here (4,5, eg) in the form of isobar distributions at two different instants for the impact between spherical water droplet and an elastic planar surface for collision speed of 0.2 C_o, i.e., "liquid Mach number" 0.2, are shown in Figs. 30 and 31. Just as for impact between a spherical droplet and a rigid surface, maximum pressure is initially at the center and during the collision moves to the edge of the contact area. The edge of the contact area also forms a deeper depression than the center.

Timm (60, 61), working here, used a million frame/second Beckman-Whitley rotating mirror camera to study liquid jet impingement upon various elastomeric coatings upon steel backings. Figures 32 and 33 show typical results for different elastomeric materials. He found significant differences in the velocity and direction of splash-back depending upon the properties of the target material. Splash-back was minimal for the more rigid elastomerics, and also for plexiglass, but quite pronounced (Fig. 32 for some of the rubber-coated materials. However, no correlation between the pattern of splash-back and erosion resistance of the materials could be found (60, eg.). His pictures for the impact of a

bullet upon plexiglass indicated the propagation of elastic waves into the material.

Field et al (58) took high-speed photographs of the impact between a water jet and PMMA (polymethylmethacrylate) plastic. Their pictures show clearly the propagation of elastic waves (shock waves) into the plastic. Also shown is a detached shock wave in the plastic outside the impact area.

5. Miscellaneous Effects

a. Liquid Relaxation and Short-Time Duration of Liquid Impact

As already mentioned, the time duration of the important portion of liquid impact from the viewpoint of maximum pressures and hence erosion effects is extremely short, only a very few microseconds. Also as mentioned, this may give rise to effective material mechanical properties which differ substantially from those obtained in conventional material property tests. These can be regarded as semi-static by comparison. In general the material strength properties under such highly dynamic loading conditions are greater than the conventional values, whereas ductility properties tend to be suppressed, with the result that failures often appear to be of the brittle fracture type. Unfortunately these highly transient effects are not fully understood or documented, so that in this area of liquid impact erosion research much yet remains to be done.

In addition to the material-oriented transient effects, the liquid behavior also must be taken into account. In both cavitation bubble collapse and liquid impact there is the possibility that fluid behavior, both liquid and vapor, may not follow equilibrium relations. For example, vapor evaporation or condensation, and subsequent heat transport, may not be sufficiently rapid to prevent a change in vapor pressure during the final portion of

cavitation bubble growth or collapse. This can thus restrain the growth or collapse of bubbles, reducing overall cavitation effects, for either inception or damage. This particular situation, dubbed "thermodynamic effects" in the cavitation literature, is further discussed in the section on cavitation bubble dynamics. However, there are also highly transient liquid effects which may affect liquid-solid impact, and these are discussed in the following.

b. Liquid Relaxation Effects

The duration of the final important portion of cavitation bubble collapse or that of the important initial portion of liquid-solid impact may be so short that, at least with certain liquids, non-equilibrium relaxation effects become important. This has been observed, eg, in impact tests by Kozirev, et al (63, 64, eg) with certain resins, where the liquid appeared to behave as a brittle solid rather than as a conventional liquid during the impact process. Figure 34 is from a high-speed motion picture sequence showing this behavior which he ascribes to the hypothesis that the relaxation time of the liquid is long compared to the duration of the impact. He believes that this type of phenomenon may occur in the final stages of cavitation bubble collapse and the resultant liquid microjet impact upon an adjacent material. Much research is still necessary to evaluate the possible significance of this phenomenon, but it certainly appears possible that such non-equilibrium phenomena may be important in some instances.

c. Light Flash Phenomena

The observation of sono-luminescence in cavitation is well documented by numerous investigators and discussed in further detail here in the sections on cavitation bubble dynamics. The luminescence is now generally ascribed to the very high temperatures resulting from the essentially adiabatic compression

of the permanent gas and vapor trapped within collapsing cavitation bubbles, and falls under the general heading in this book of cavitation "thermodynamic effects". It is there also discussed. However, it is another example of non-equilibrium behavior due to the very short time duration of the phenomenon.

Somewhat similar liquid flashes have also been reported (65-67,eg) for very high-velocity liquid-solid impact cases. The light is there believed due to essentially adiabatic compression of air trapped between the liquid jet and the solid. Again further research is required to understand more definitely this phenomenon.

D. Overall Erosion Performance

1. General

The overall liquid-induced erosion performance of materials subjected particularly to cavitation has been discussed in detail in Section V-C of this book. Semi-empirical relations were there presented relating measured erosion rates (volume loss rate per unit exposed area, i.e., "MDPR" = "mean depth of penetration rate") and material mechanical and fluid properties. As discussed elsewhere in this section and Chapter V (Cavitation Damage), a consideration of the basic mechanisms of cavitation and liquid impact damage show that these are in all probability very similar. In fact, historically, rotating wheel jet impact tests have been used to provide an indication of cavitation, as well as droplet impact erosion, resistence of materials. It is also well-accepted that the general appearance of erosion resulting from these two phenomena is very similar. Hence, the data sets (68,69)used for the generation of damage-predicting relations for cavitation damage particularly, but also presumably applicable to some extent to impact damage were drawn from both cavitation and liquid impact tests. The present section, emphasizing liquid impact particularly, discusses other pertinent features applicable only to impact effects, rather than cavitation. Examples of other such features are the effects of impact velocity, angle, droplet or jet diameter. While such parameters apply also to cavitation damage, their effects cannot easily be studied except with impact tests, since in general their magnitudes are not known or controllable in cavitation tests.

A semi-rational approach to either the impact or cavitation erosion phenomenon can be made, as already discussed in Section V-C. One such approach (68) results in Eq.D-1 here repeated for convenience from Section V-C. The nomenclature is explained there.

$$MDPR = \left(\frac{\eta}{\varepsilon}\right)\left(\frac{A_p}{A_e}\right)\left(\frac{\rho_{eff}}{2}\right)(V^3) \qquad \text{---------} \qquad (D\text{-}1)$$

As explained in V-C only the first quotient in Eq D-1, i.e., (η/ε), and the effective density ρ_{eff} can be estimated at all for cavitation tests. The effective density ρ_{eff} is there roughly that of the liquid, but it is the actual density of a mixture of liquid droplets and surrounding gas in an impact test. Hence it can be readily calculated for impact tests from the test parameters.

η is the efficiency of energy transfer between impacting "microjet" (cavitation) or droplet and material surface, and is thus a function of at least the "acoustic impedance ratio". ε is a material property giving the necessary energy input to a material surface to cause removal of unit volume of material. Hence for fixed "flow conditions" in either an impact or cavitation test, the ratio η/ε is assumed proportional to MDPR, i.e., rate of volume loss per unit area exposed, and cavitation or impact tests could be used to evaluate "best-fit" relations between measured erosion rates and material and fluid properties. This is the course which has already been described in Section V-C. The present section attempts to further clarify the relationship between measured erosion rates and the other parameters called to attention by semi-empirical relations such as Eq.D-1 and particularly pertinent to liquid impact rather than cavitation erosion.

2. Effects of Velocity and Angle

a. General Considerations

It has generally been accepted in the past that only the component of velocity normal to the surface (Eq. D-1)is important to the damage process. It is also generally believed, as the result of much previous test data, that damage rate is most often proportional to the fifth or sixth power of velocity rather than the third power, as shown by the semi-rational Eq.(D-1). However, such a higher order velocity dependence may still be consistent with Eq.(D-1) since the efficiency of energy transfer between droplet and material surface (η) is quite probably also velocity dependent to some extent. There is also the possibility that the effect of the high radial velocity generated in the collision, and discussed in section B of this chapter, could affect the velocity dependence. This mechanism was not considered in the generation of the simplified model resulting in Eq. (D-1)

It has also been often considered that there is a "threshold velocity", presumably applied to the normal component, below which zero or negligible damage will result. Obviously the value of such a "threshold velocity" must depend upon duration of the test, so that such a simplified general model cannot be truly valid. If the "threshold velocity" model is used, then the velocity dependence is related to the energy increment above such a threshold. Such a concept would then assume a "threshold energy" to cause damage. This possibility also was not considered in the generation of Eq. (D-1) It is the purpose of the following material to examine the validity of these various concepts, based upon some relatively recent impact data, as previously reported in detail in ref. 68.

b. Specific Test Results

For this purpose some of the data generated by recent rocket sled tests at Holloman AFB have been examined to determine the suitability of certain

of these semi-empirical damage-predicting equations. The portion of the rocket sled data selected for this analysis comprised ten groups of materials including ceramics. plastics, and metals. They were tested in the 6000 ft. rain field at Holloman AFB at Mach numbers ranging from 1.5 to 3.0, at various angles of impact ranging from 13.5° to 90 $^{-deg}$. The full details of this analysis have been reported previously (70). Some salient features will be repeated here for convenience.

An earlier report (71)based upon an experimental fit of rocket sled data suggests the velocity appears in an exponential form:

$$MDPR = C_1 e^{aV} \sin \theta + C_2 e^{bV} \qquad \text{---------- (D-2)}$$

where C_1, C_2, a and b are constants depending on material properties, and θ = angle of impact (90^{-deg} for perpendicular impact).

Baker, et al.(72) proposed a relation based on their impact data, which includes the concept of a threshold velocity below which damage is essentially zero:

$$MDPR = K(V \sin \theta - V_o/\sin \theta \quad \text{for } V \sin \theta > V_o$$
$$= 0 \qquad \text{for } V \sin \theta \leq V_o \qquad \text{---------- (D-3)}$$

More recently Hoff and Langbein (73) have suggested a modification of Eq. D-3 whereby the denominator is squared:

$$MDPR = K (V \sin \theta - V_o)^n / \sin^2 \theta \quad \text{for } V \sin \theta > V_o$$
$$=0 \qquad \text{for } V \sin \theta \geq V_o \qquad \text{---------- (D-4)}$$

Eq. D-2 is simply a curve-fitting expression, not based on any physical model. Eq. D-3 on the other hand assumes basically that MDPR is proportional to the difference between the normal component of the impact velocity and some "threshold velocity" all raised to some power, n. A similar assumption has often been made in the cavitation literature (74-76,eg.) where damage was found proportional to the 6th power of the flow velocity,

based upon tests on a soft aluminum ogive in a water tunnel. In Eq. (D-3) sin θ has been added to the denominator to take some account of the damage due to shear from the high radial velocity after impact, which increases for oblique collisions, as discussed to some extent in section B of this chapter. Actually, since in the rocket sled type test the specimen impacts a reduced number of raindrops if the impact is not normal, it might be argued that an additional sin θ is required in the numerator, cancelling that in the denominator. This latter variation was not tested in the present numerical analysis.

Eq. D-4 is identical to eq. D-3 except that $\sin^2 \theta$ appears in the denominator. This term can be derived logically from a model assuming energy flux on the target to be the predominent mechanism (73), if it is also assumed that the efficiency of energy transfer between impacting drop and target is a function of V sin θ only (D-1). However, it seems unlikely that this is strictly the case, so that Eq. D-3 and D-4 remain semi-empirical in nature, and to be tested only in terms of a data fit.

c. Computer Correlation Results

The most comprehensive analysis of the rocket sled data was made using Eq. D-3. For each material a least mean square fit regression analysis was made to determine the best value of threshold velocity V_o, and of the amplitude constant K and the velocity exponent n. (70). Table 2 shows effects of velocity threshold, V_o, K and velocity exponent, n, for one of the materials n.

This table shows particularly the effect of the choice of threshold velocity V_o on the best values for the velocity exponent, n and the amplitude constant, K. The effect on K of varying the assumed V_o between 0 and 2000 f/s is small, but the velocity exponent varies from 6.44 to 2.28, depending on the essentially arbitrary choice of "threshold velocity". No certain value of

V_o was in fact indicated by the tests. A plot of MDPR vs. normal impact velocity, V shows a small or zero MDPR for small velocities, and then a rapidly increasing MDPR for larger velocities. Such a curve can be fitted almost equally well by various combinations of V_o (including V_{zero}) and velocity exponent, n, as the present calculations show. Since, strictly, it is unlikely that there will be zero damage for repeated impacts at any velocity, it may be permissible to avoid the concept of threshold velocity entirely. If it is used, it must obviously be a function of number of impacts per second and test duration as well as velocity may be necessary to define an arbitrarily small but finite limit for MDPR, which will then define the threshold velocity. Figure 35 shows two typical sketches for the probable relations between probable error and choice of threshold velocity for the present data. For those materials exhibiting behavior of the type shown in Fig. 35. , the optimum choice for threshold velocity is zero. For other materials, as in sketch 35 a definite optimum V_o appears.

For some of the present materials, "best values" of V_o, K and n were computed from both Eq. D-3 and D-4. Table 3 shows the comparison for an inorganic laminate, D-2 and a thermal plastic. A more complete description is given in ref. 70. While Eq. D-4 calls for an exponent 2 for the sin θ term, the effect of exponents ranging from 1.0 to 2.5 was examined (n = 1 corresponds to Eq. D-3. It is noted that for these materials, the choice of n affects the best choice of threshold velocity (and of course n, which is not listed), but affects the minimum probable error only slightly. From this data it appears that a choice of n = 1, desirable for the sake of simplicity, would not significantly reduce the "goodness" of the correlation. The effect on probable error of assuming zero threshold velocity (also desirable for simplicity) is shown in the last column. It is noted that the additional error so introduced is not large.

d. Generalized Erosion Model

The limited success achieved in correlating the rocket sled test data using Eq. D-3 or D-4 leads to the conclusion that a more basic mathematical model is required. However, the lack of good correlation is partly due to the type of data used. It is not entirely permissible to compare damage attained after a fixed exposure period for materials of widely differing resistances as was necessary for these rocket sled tests, since only a mean MDPR can then be computed for materials in very different portions of their MDP vs. time (or number of impacts) curve. It is thus necessary to use data wherein the total MDP vs. exposure curve is available, so that only comparable portions of this curve would be compared. The generation of a semi-rational erosion model has been described in detail in Section V-C of this book, pertinent to both cavitation and droplet impact. This results in Eq. (1) of both sections V-C and VI-C.

3. Material Property Correlations

a. General - As already discussed, material mechanical property correlations for predicting erosion resistance of given materials to liquid droplet impact or cavitation erosion are essentially identical, at least in the present state of the art. These have already been discussed in detail in Section V-C under the subject of cavitation erosion resistance. The extent to which damage resistance of materials can be realistically related to the conventional material mechanical properties, which is represents unfortunately a relatively low capability today, is there discussed. It is there shown that "ultimate resilience" and Brinell hardness are apparently the properties of greatest use in this regard at present, but that standard deviation about predicting relations is of the order x3. Whether or not such an imprecise prediction is, or is not, of engineering utility is of course a matter of personal judgment.

This relatively unsatisfactory situation exists today even for material-fluid combinations where the role of corrosion cannot be more than negligible. For "corrodible" materials, the degree of uncertainty is of course much greater. However, a detailed examination of corrosion effects is beyond the scope of this book, which is rather related primarily to highly intensive fluid mechanical effects. Nevertheless, it is well known that the combined effects of cavitation, or impingement, along with corrosion is usually much greater than their summation if acting singly. The cause of this accelerated effect is easy to envision. Corrosion roughens and weakens the surface, accelerating impingement or cavitation erosion, and the mechanical effects of cavitation or impingement quickly remove the protective coating which normally would inhibit further corrosion.

Another interesting inter-relation which exists between impact and cavitation is that liquid impact can often induce cavitation within the

impacting droplet, as explained in previous sections of this chapter, while it is presently presumed that cavitation damage is to a substantial extent the result of liquid "microjet" impact upon the damaged surface. This microjet is induced by collapse of cavitation bubbles near the surface, as fully explained in the discussions of cavitation bubble dynamics in this book.

b. Characteristic Erosion-Time Curves

Much earlier erosion work was based only on single runs, and necesarily even some recent work such as that using a rocket sled, previously described. These provide only a given volume loss after a fixed time interval (71, eg). However, it has more recently become fully realized that the erosion-time curves induced in either cavitation or impact tests are not linear with time. This was probably first emphasized by the work of Thiruvengadam (77, eg.), and is now being well documented and described in the definitions, etc. being promulgated by ASTM Committee G-2 (78, eg). However, there is still much disagreement in this matter, and it appears that cavitation or impingement curves generated by different types of test devices and different material-fluid combinations differ importantly in their characteristic erosion-time curves. However, there appears to be no systematic difference between cavitation and impingement erosion tests in this regard. In general, "S-shaped" curves are generated (Fig. 36, characterized by an initial period of negligible or low damage rate "incubation period". This is followed by a period of increasing rate, then a period of approximately constant maximum erosion rate, and finally a period of decreasing, or sometimes oscillating, rate. Which of these periods are of greatest importance of course depends upon the application.

Some pertinent theoretical work has also been done in recent years to explain the shape of these curves, particularly by Heymann (69, eg), Engel (79, 80, eg), and others. It is possible to justify any of the experimentally observed curve shapes by a mathematical model assuming material failure to be primarily a high-strain fatigue mechanism (69, eg).

c. Recent Impact Erosion Studies

Several recent relatively comprehensive studies have been made to attempt to understand in more detail material reactions to droplet impact and thus attain the ability to predict "a priori" material resistance to such attack. These studies have included detailed basic computer modelling of the fluid and material behavior, such as the work here of J.-B. Hwang already discussed where the influence of a non-rigid (elastic) material was considered. In addition, various quasi-basic studies of material reaction, where erosion rates were correlated with theoretical material models, have been made. In some cases various non-metallic materials have been studied because of their importance in such applications as rain erosion of high-speed aircraft and missile components. Relatively recent work by Engel (79,80, eg) has developed a quasi-empirical failure model for various non-metallics for this purpose. More recently Springer and colleagues at U-M (81-84,, eg) have developed such models for "homogeneous", coated and fiber-reenforced materials. A detailed description of these and other such hypothetical failure models is beyond the scope of this book, which is concerned more with fluid behavior than material reaction which is of course a major topic in itself. Various recent studies of this general type are found in the ASTM hard-cover book (ibid 81). Other related relatively recent studies are reported in the series of "Meersburg Conference" proceedings (ibid 82). It is probable that continued conferences will appear in future in these two series.

E. Liquid Impact Test Devices

1. General - Applications Including Jet Cutting

Liquid impact test devices have to some extent been described in this chapter in section C, concerning experimental and photographic studies, and also in section V-A on cavitation test devices. Historically, conventional liquid impact tests have also been considered to be cavitation tests. In fact, local cavitation may well occur in many apparent impact situations, and damaging cavitation bubble collapse apparently often involves liquid microjet impact. Hence the two phenomena are at this point intimately related. It seems useful here to describe briefly the various types of nominal liquid impact tests devices. These can best be divided according to whether the high relative impact velocity is generated primarily by motion of the specimen or of the liquid slug, of whatever geometry it may be.

For the testing of general erosion resistance of materials as well as for purposes of basic research, devices in which the liquid slug is relatively stationary are most numerous and also most important. However, these devices are today by no means standardized*, since they are not sufficiently numerous and are usually designed to deal with relatively specialized needs in different specific applications. This lack of standardization is also at present the case in devices designed to produce jet cutting or controlled erosion, such as to assist coal-mining, tunneling, oil-well drilling, wood cutting, and numerous other applications. Also standard tests are lacking for these jet-cutting devices, some of which rely partially on cavitation and/or mechanical cutters.

2. Moving Target Devices

a. Rotating Disc Tests for Hydraulic Turbine Application

The earliest and simplest form of this type of liquid erosion testing device is the rotating disc (or wheel), to the periphery of which test

*A round-robin test program was recently conducted by ASTM Comm. G-2 (85) from which it was concluded that standardization at this time was not possible.

specimens are attached. These have been employed since the 30's (11,67,86, eg). The rotating specimens generally cut a relatively low velocity cylindrical water jet, so that the relative impact velocity was primarily the result of the specimen velocity, generally $\sim$ 100 m/s. It is apparent that this geometry (Fig. 37) would often generate local cavitation around the test specimens, so that the resultant erosion most probably included a substantial component of cavitation. In fact, the impact velocity was such that damage from impact itself of some of the resistant materials which were tested, such as various stainless steels, would not otherwise have been expected. The application to which this early testing was addressed was generally hydraulic turbines and pumps.

b. Rotating Discs for Steam Turbine Application

Relatively similar test devices operating at higher velocities ($\lesssim$500 m/s) have been developed and utilized by various steam turbine companies (87, eg.), particularly in England. The application of interest for these studies was the wet steam water droplet erosion problem encountered in the low pressure end of large steam turbines. This general problem is further discussed in Chapter VII.

c. Aircraft and Missile Rain Erosion

During the post World War II period, the problem of rain erosion of aircraft and missile components has become of importance. This has resulted in the development of even higher velocity test devices, wherein material specimens are driven through an artificial rainfield. In most cases this has been accomplished by "propellor arms", i.e., essentially zero-lift rotating propellor arms, to which the specimens to be tested are attached. These "arms" are generally of relatively large radius, up to 14 ft. in the Bell device (41,eg) order to minimize the centrifugal loading on the specimens. The highest velocity

machine to have been operated to the present is that at Bell Aerospace [41] with a maximum design speed of Mach 3, i.e., ~ 1000 m/s. Numerous lower speed devices exist in various laboratories in the U.S., England, Germany (Dornier), and elsewhere. These machines are generally distinguished from the previously described steam turbine test devices by the fact that the required test times are very much shorter, since the aircraft and missile components to be tested, such as radomes, eg. are of much less resistant materials than are the steam turbine blades. A "radome", eg. must be primarily transpartent to radar, and hence metallic materials are excluded. A recent book and reports by Springer[81-84,eg] summarized much recent information on the erosion resistance of these types of materials.

Ultra-high-velocity tests for rain erosion have been conducted using a "rocket sled" propelled along through an artificial rainfield [40,51,52,eg.] at Holloman AFB. For this device velocities up to about air Mach 5 [89] have been reached. This test of course does not permit intermittent examination of the test specimens, as do the rotating arm or disc tests previously discussed. It does allow the simultaneous testing of numerous materials at different angles of impact in a single run, thus assuring that all experience the same rainfield. This type of test also eliminates the extraneous centrifugal loading involved in the rotating arm and disc tests.

d. Basic Liquid Impact Research Test Devices

For purposes of basic research into liquid impact phenomena, Fyall, et al [26] at RAE Farnborough developed a device wherein the target is fired as a "bullet" against a suspended stationary spherical liquid droplet. Control of the droplet shape and size is much more precise for this device than for any of those involving artificial rainfields previously described. Falling drops achieve some reasonable degree of spheroidicity, but not to the extent achieved by the Fyall device. Also, since the droplet is completely stationary, the potential for high-speed photography is maximized. Problems of droplet stability

preclude the acceleration of a liquid droplet or desired size ($\sim$ 1 mm radius) against a stationary target. Of course the Fyall device is not well adapted to the study of material erosion under repeated impact, since it is essentially a single-shot device. It also introduces the difficulty of target recovery without damage, but a decelerating system for this purpose was successfully developed.

A somewhat similar device wherein a target "bullet" was fired against a liquid disc supported between parallel plates was developed and used by Brunton, et al [22,39,eg.] at University of Cambridge. This work has been previously discussed in this chapter. It of course does not model impact with a spherical drop, rather introducing a droplet disc geometry, i.e., impact between a flat plate and the side of a liquid cylinder. However, it does allow precise control of droplet shape and size, as well as the inclusion of a very small pressure transducer in the "bullet". Again recovery without damage of the bullet is required. This device[22,39] as well as that of Fyall [26], does provide precise photographic and other information for direct comparison with such computer models as those already discussed in Section C of this chapter.

3. Stationary Target Devices

As already mentioned, for reasons of droplet stability, i.e., a critical Weber number exists, it does not appear possible to propel a spherical droplet at pertinent size and velocity against a stationary target. For this reason, devices of this type are less adapted to liquid impact erosion tests, since a "realistic" droplet shape cannot easily be achieved. However, in general, facilities of this type tend themselves to be much less complex and expensive. Also, devices for purposeful jet-cutting are almost necessarily of the stationary target type, so that standardized test devices for such machines must also propel the jet or other liquid slugs against essentially stationary targets.

The difficulty of uncontrolled and perhaps undesirable droplet shape was overcome to some extent by the momentum-exchange liquid-gun device, pioneered and developed by Bowden and Brunton (44, 49,50 eg.) and discussed somewhat in Section C. This device can produce a high-velocity jet with an approximately spherical leading edge. Hence it can model quite well impact with spherical droplets since it is only the initial portion of the impact which is of primary importance from the viewpoint of erosion. It can also produce a microjet (Monroe jet) of even higher velocity than the main jet (depending upon the initial position of the liquid meniscus). Maximum velocities attained with such devices are reported to be up to $\sim$ 1000 m/s (49). As originally developed this is a single-shot device, not adapted to multiple impact erosion studies, but rather to studies of the basic impact phenomenon.

The provision of repeated impacts upon a target with a device providing quite similar droplet shape, but somewhat reduced velocity capability ($\lesssim$ 550 m/s) was achieved by the water "gun" device pioneered by Kenyon (53), and later used also in our own laboratory at Michigan for erosion testing of various materials as well as high-speed photographic studies of droplet impact (45, 54 , eg). Typical results are shown in Figs. 29 and 32,33 of this chapter. The Kenyon and Michigan devices separate the water cavity from which the jet is to be ejected from the driving mechanism by a thin steel diaphragm, rather than a rubber washer as in the Bowden-Brunton device. The necessary shock for liquid propulsion is provided in the Kenyon-Michigan device by a steel bolt driven by a heavy spring, rather than a pellet from an air or gas gun or conventional rifle, as in the Bowden-Brunton device. Figures 38-39 show schematic representations of these two systems, respectively. The Kenyon-Michigan device allows automatic operation to provide essentially a water "machine gun", capable of producing about 30 shots per minute. These devices are thus obviously easily adapted to material resistance screening tests, but unfortunately do not provide a very simple and realistic droplet shape

from the viewpoint of the aircraft or turbine erosion problem, as do the rotating arm and disc, or rocket sled devices, previously discussed. However, both Bowden-Brunton type and Kenyon-Michigan devices do provide economic and simple bench-type facilities useful for some types of impact erosion testing and study. Their cost is generally an order of magnitude less than most of the rotating devices.

Bibliography

1. Y.C. Huang, "Numerical Studies of Unsteady, Two-Dimensional Liquid Impact Phenomena," Ph.D. thesis, Mech. Engr. Dept., Univ. Mich., Ann Arbor, Mich., ORA Report No. UMICH 03371-8-T, June 1971.

2. Y.C. Huang, F.G. Hammitt, W.J. Yang, "Hydrodynamic Phenomena During High-Speed Collision Between Liquid Droplet and Rigid Plane," Trans. ASME, J. Fluids Engr., 1, 95, 2, 1973, p. 276-294.

3. F.G. Hammitt, Y.C. Huang, "Liquid Droplet Impingement Studies at University of Michigan," Conf. Publication #3, Inst. of Mech. Engrs., Univ. of Warwick, Coventry, April 3-5, 1973, p. 237-243.

4. J.B. Hwang, "The Impact Between a Liquid Drop and an Elastic Half-Space," ORA Report No. UMICH 012449-5-T, Mar. 1975, Ph.D. thesis, Mech. Eng., U. of Mic

5. J.B. Hwang, F.G. Hammitt, "Transient Distribution of the Stress During the Impact Between a Liquid Drop and an Aluminum Body," Proc. 3rd International Symposium on Jet Cutting Technology, Chicago, May 11-13, 1976.

6. J.B. Hwang, F.G. Hammitt, "High Speed Impact Between Curved Liquid Surface and Rigid Flat Surface," ORA Report No. UMICH 012449-10-T, October 1975; submitted to ASME for publication.

7. J.B. Hwang, F.G. Hammitt, W. Kim, "On Liquid-Solid Impact Phenomena," 1976 ASME Cavitation Forum, p. 24-27.

8. F.J. Heymann, "On the Shock Wave Velocity and Impact Pressure in High-Speed Liquid-Solid Impact," Trans. ASME, J. Basic Engr., 90, D, 1968, p. 400-402.

9. M.C. Rochester, J.H. Brunton, "Surface Pressure Distribution During Drop Impingement," Proc. 4th International Conf. on Rain Erosion and Associated Phenomena, Meersburg, Germany, May 1974.

10. W. Johnson, G.W. Vickers, "Transient Stress Distribution Caused by Water-Jet Impact," J. Mech. Engr. Sci., 15, 4, 1973, p. 302-310.

11. P. DeHaller, "Untersuchungen uber die durch kavitation hervorgerufenen korrosionen," Schwiez Bauzig, 101, 1933, p. 243.

12. F.H. Harlow, "The Particle-in-Cell (PIC) Computing Method for Fluid Dynamics," Methods in Computational Physics, 3, 1964, p. 319-343.

13. Saint-Venant, "Theorie de l'Elasticité des Corps Solides," J. Mathématiques (Louiville), 1867, p. 387.

14. S.C. Cook, "Erosion by Water Hammer," Proc. Roy. Soc. (London), A, 119, 1928, p. 481-488.

15. P.G. Tait, "Report on Some of the Physical Properties of Fresh Water and Sea Water," Rept. on Scientific Results of Voyage of H.M.S. Challenger, Phys. Chem., 2, (1888), p. 1-71.

Bibliography (cont.)

16. Y.C. Huang, F.G. Hammitt, "The Compressible Cell and Marker Numerical Method (ConCAM) for Compressible Fluids Problems," Proc. Symp. on Applications of Computers to Fluid Dynamic Analysis and Design, Jan. 1973. also available as ORA Report No. UMICH 03371-20-T, Univ. Mich., Ann Arbor Mich.

17. Sir Horace Lamb, Hydrodynamics, Dover, 1965.

18. P. Lax, B. Wendroff, "System of Conservation Laws," Comm. on Pure and Appl. Math., XIII, 1960, p. 217-237.

19. W. Edwin, W. Jardetzky, F. Press, Elastic Waves in Layered Media, McGraw Hill, 1957.

20. R.J. Wasley, Stress Wave Propagation in Solids: An Introduction, Marcel Dekker, Inc., New York, 1973.

21. S.P. Timoshenko, J.N. Goodier, Theory of Elasticity, 3rd ed., McGraw-Hill, 1970.

22. M.C. Rochester, J.H. Brunton, "Surface Pressure Distribution During Drop Impingement," Proc. 4th Int. Conf. on Rain Erosion and Assoc. Phenomena, Meersburg, Germany, May 1974.

23. M.C. Rochester, J.H. Brunton, "The Influence of Physical Properties of the Liquid on the Erosion of Solids," Erosion, Wear and Interface with Corrosion, STP 567, ASTM 1974, p. 128-151.

24. W. Johnson, G.W. Vickers, "Transient Stress Distribution Caused by Water-Jet Impact," J. Mech. Eng. Science, 15, 4, 1973, p. 302-310.

25. O.G. Engel, "Damage Produced by High-Speed Liquid-Drop Impact," J. Appl. Phys., 44, 2, Feb. 1973, p. 692-704.

26. A.A. Fyall, "Single Impact Studies with Liquid and Solids," Proc. 2nd Conf. o Rain Erosion, Meersburg, Germany, Aug. 1967, edit A.Fyall, RAE, Farnsborough,

27. J.H. Brunton, J.J. Camus, "The Flow of Liquid Drop During Impact," Proc. 3rd Int. Conf. on Rain Erosion and Assoc. Phenomena, Elvetham Hall, Englan Aug. 11-13, 1970.

28. L.J. Briggs, "Maximum Superheating of Water as a Measurement of Negative Pressure," J. Appl. Phys., 26, 8, Aug. 1955, p. 1001-1003.

29. R.E. Apfel, "The Tensile Strength of Liquids," Scientific American, 227, 6, Dec. 1972, p. 58-71.

Bibliography (cont.)

30. L.A. Glenn, "On the Dynamics of Hypervelocity Liquid Jet Impact on a Flat Rigid Surface," J. Appl. Math. and Phys. ., 25, 1974, p. 383-398.

31. L.D. Tyler, "The Flow Dynamics of a Liquid Drop During High-Speed Impact," Bull. of Am. Phys. Soc., 16, 11, 1971, p. 1319.

32. R.M. Blower, "On the Response of an Elastic Solid to Droplet Impact," J. Inst. of Math. and Its Applications, 5, 2, 1969, p. 167-193.

33. W.F. Adler, "Analytical Modeling of Liquid and Solid Particle Erosion," AFML-TR-73-174, Air Force Materials Lab., WPAFB, Sept. 1973.

34. G. R. Johnson,"Liquid Solid Impact Calculations with Triangular Elements", Trans. ASME, J. Fluids Engr., 1978.

35. G. R. Johnson, "Analysis of Elastic-Plastic Impact Involving Severe Distortions", Trans. ASME, J. Appl. Méch., Sept. 1976, 439-444.

36. G. R. Johnson, "A New Computational Technique for Impulsive Loads", Proc. 3rd. Inter. Symp. on Ballistics, Karlsruhe, W. Germany, March 1977.

37. D.C. Jenkins, J.D. Booker, "The Impingement of Water Drops on a Surface Moving at High Speed," Aerodynamic Capture of Particles, ed. E.G. Richardson, Pergamon Press, New York, 1960, p. 97.

38. D.C. Jenkins, "An Experimental Method for Studying the High-Speed Impact of a Liquid Drop on a Liquid Surface," Ingenieur Archiv, XXXVI, 1967, p. 280-284.

39. M.C. Rochester, J.H. Brunton, " The Influence of Physical Properties of the Liquid on the Erosion of Solids," Erosion, Wear and Interface with Corrosion, STP 567, ASTM, 1974, p. 128-151.

40. G.F. Schmitt Jr., A.H. Krabill, "Velocity-Erosion Rate Relationships of Materials in Rain at Subsonic Speeds," AFML-TR-70-44, Air Force Material Laboratory, Wright-Patterson AFB, Ohio, October 1970.

41. N.E. Wahl, "Design and Operation of Mach 3 Rotating Arm Erosion Testing Apparatus," Proc. 3rd Int'l Conf. on Rain Erosion and Associated Phenomena, Aug. 11-13, 1970, Royal Aircraft Establishment, England, p. 13-42,

42. F.G. Hammitt, J.B. Hwang, etal., "Experimental and Theoretical Research on Liquid Droplet Impact," Proc. 4th Int'l Conf. on Rain Erosion and Associated Phe May 8-10, 1974, Meersburg, Germany.

43. N.L. Hancox, J.H. Brunton, "The Erosion of Solids by the Repeated Impact of Liquid Drops," Phil. Trans. Royal Soc. London, Ser. A, 260, 1110, 1966, p. 121-14

44. F.G. Hammitt, J.B. Hwang, etal., "Cavitation and Droplet Impingement Damage of Aircraft Rain Erosion Materials," Proc. 3rd Int'l Conf. on Rain Erosion and Associated Pheno., Aug. 11-13, 1970, p. 907-935.

45. O.G. Engel, "Water Drop Collision with Solid Surface," J. Res. Nat. Bur. Stand. 54, 5, May 1955, p. 281.

46. O.G. Engel, "Pits in Metals Caused by Collision with Liquid Drops and Soft Metal Spheres," J. Res. Nat. Bur. Stand., 62, 6, 1959, p. 229-246.

47. J.H. Brunton, J.J. Camus, "The Flow of Liquid Drop During Impact," Proc., International Conf. on Rain Erosion and Associated Phenomena, 1970, p. 327.

48. F.J. Heymann, "On the High-Speed Impact Between a Liquid Drop and a Solid Surface," J. Applied Physics, 40, 13, 1969, p. 5113-5122.

49. F.P. Bowden, J.H. Brunton, "Deformation of Solids by Liquid Impact at Supersonic Speeds," Proc. Royal Soc. (London), Series A, 263, 1961, p. 433-450, also see Series A, 260, no. 1110, 79-85, 1966.

50. F.P. Bowden, J.E. Field, "The Brittle Fracture of Solids by Liquid Impacts, by Solid Impacts, and by Shock," Proc. Royal Soc. (London), Series A, 282, 1964, p. 331.

51. G. F. Schmitt, Jr., "Erosion Rate-Velocity Dependence for Materials at Supersonic Speeds," ASTM STP 474, 1969, 323-352.

52. G. F. Schmitt, Jr., W. G. Reinecke, and G. D. Waldman, "Influence of Velocity, Impingement Angle, Heating; and Aerodynamic Shock Layers on Erosion of Materials at Velocities of 5500 ft/s (1700 m/s), ASTM STP 567, 1973, 219-238.

53. H.F. Kenyon, P.H. Dawson, "Erosion by Water Jet Impacts," Report No. TP/R5626, Associated Electrical Industries Ltd., Manchester, England, 1969.

54. F.G. Hammitt, J-B. Hwang, Linh N. Do, "Interrupted Jet Water Gun Impact Erosion Studies on Metallic Alloys," Cavitation and Polyphase Flow Forum, ASME, 1974, p. 24-26.

55. H. Kolsky, Stress Waves in Solids, Dover, 1963.

56. R.M. Blower, "On the Response of an Elastic Solid to Droplet Impact," J. of the Institute of Mathematics and Its Applications, 5, 2, 1969, p. 167-193.

57. F. B. Peterson, "Some Consideration of Material Response Due to Liquid-Solid Impact," J. Fluid Engr., Trans. ASME, 95, Series A, 2, 1973, p. 263-270.

58. A. E. H. Love, "The Stress in a Semi-Infinite Solid by Pressure on Part of the Boundary," Trans. Roy. Soc. (London), Series A, 228, 1929, p. 377-420.

59. W. E. Goodier, W. E. Jahsman, E. A. Ripperger, "An Experimental Surface Wave Method for Recording Force Time Curves in Elastic Impacts," J. Appl. Mech., Trans. ASME, 26, 1, 1959, p. 3-7.

60. E. E. Timm, "An Experimental Photographic Study of Vapor Bubble Collapse and Liquid Jet Impingement," Ph.D. thesis, Dept. of Chem. Engr., Univ. of Mich., 1974; also available as ORA Report No. UMICH-01357-39-T, U. of Mich., Ann Arbor, Mi., 1974.

61. F. G. Hammitt, E. E. Timm, J-B. Hwang, Y. C. Huang, "Liquid Impact Behavior of Various Non-Metallic Materials," Erosion, Wear and Interface with Corrosion, ASTM STP-567, 1974, p. 197-218.

62. J. E. Field, J. J. Camus, et al., "Impact Damage Produced by Large Water Drop," Proc. 4th International Conf. on Rain Erosion and Allied Phenomena, May 8-10, 1974, Meersburg, West Germany, edit. A. Fyall, RAE, Farnsborough, England.

63. S. P. Kozirev and K. K. Shalnev, "Explanation of Solid Damage Due to Free Drop Impact, Jet Impact, and Cavitation by Relaxational Hypothesis", Proc. 4th Conf. on Fluid Mechanics, Budapest, 1972.

64. S. P. Kozirev and K. K. Shalnev, "Interpretation of Experimental Data in Witness of Relaxational Hypothesis of Cavitation Erosion," Proc. 5th Conf. on Fluid Mechanics, Budapest, 1975.

65. S. De Corso and R. Kothmann, "Characteristics of the Light Flash Produced upon Impact of a Liquid with a Surface",Materials Research and Standards, 5, 10, ASTM, 525-528, 1965.

66. A. G. Gaydon, "Light Emission from Shock Waves and Temperature Measurements," Proc. 9th Int. Shock Tube Symposium, Stanford Univ. 1973, 11-22.

67. G. R. Hoff, "Personal Communication" to F. G. Hammitt, Dornier-System GmbH, Friedrichshafen, Germany, 1971.

68. F.G. Hammitt, etal., closure to "A Statistically Verified Model for Correlating Volume Loss Due to Cavitation or Liquid Impingement", ASTM STP 474, 319-322, 1970.

69. F.J. Heymann, "Toward Quantitative Prediction of Liquid Impact Erosion," ASTM STP 474, 1970, p. 212-244.

70. T. M. Mitchell and F.G. Hammitt, "Preliminary Analyses Applied to a Portion of Holloman AFB Rocket Sled Data on Rain Erosion Materials", ORA Report No. 01077-4-T, University of Michigan, Oct. 1968.

71. G. Tatnall, K. Foulke, and G. Schmitt, Jr., "Joint Air Force-Navy Supersonic Rain ErosionEvaluation of Dielectric and Other Materials", Report No. NADC-AE-6708, 1967.

72. W. C. Baker, K.H. Jolliffe, and D. Pierson, "The Resistance of Materials to Impact Erosion Damage", A Discussion on Deformation of Solids by the Impact of Liquids, Phil. Trans. Roy. Soc., A, No. 1110, Vol. 260, 193-203, July 1966.

73. G. Hoff, G. Langbein, and H.Reiger, "Investigation of the Angle-Time Dependence of Rain Erosion", Progress Report No. 62269-7-002050, Dornier System GmbH, March 1968.

74. R. T. Knapp, "Recent Investigations Of Cavitation and Cavitation Damage", Trans. ASME, v. 77, 1045-1054, 1955.

75. R.T. Knapp, J.W. Daily, and F.G.Hammitt, Cavitation, McGraw-Hill, Inc., New York, N.Y.

76. F.G. Hammitt, etal, "Initial Phase of Damage of Test Specimens in a Cavitating Venturi as Affected by Fluid and Material Properties and Degree of Cavitation", Trans. ASME, J. Basic Engr., D, 87, 453-464, 1965.

77. A. Thiruvengadam, "A Unified Theory of Cavitation Damage", Trans. ASME J. Basic Engr., D, 85, 3, 365-376, 1963.

78. ASTM, "Standard Definitions of Terms Relating to Erosion by Cavitation and Impingement," Designation G 40-73, 1973

79. O.G. Engel, "Basic Research on Liquid-Drop-Impact Erosion," NASA Report No GESP-253, july 1969.

80. O. G. Engel, A. J. Pietutowski, "Investigation of Composite-Coating Systems for Rain-Erosion Protection," Naval Air Systems Command Contract N00019-71-C-0108, 1972, Univ. of Dayton, Dayton, Ohio.

81. G. S. Springer and C. B. Baxi, "A Model for Rain Erosion of Homogeneous Materials," ASTM STP 567, June 1973, 106-127.

82. G. S. Springer, C.-I. Yang, and P. S. Larsen, "Analysis of Rain Erosion of Coated Materials", Proc. 4th Int'l Conf. on Rain Erosion and Associated Phenomena, edit. A. A. Fyall and R. B. King, Royal Aircraft Est., England, 1974.

83. G. S. Springer and C-I. Yang, "Analysis of Rain Erosion of Coated and Uncoated Fiber Reinforced Composite Materials," Rept. AFML-TR-74-180, Contract F33615-72-C-1563, Aug. 1974.

84. G. S. Springer, "Erosion by Liquid Impact," Washington Scripta, distributed by Halsted, Wiley, 1976.

85. F. J. Heymann, personal communication concerning the Liquid Impact Round Robin for ASTM Committee G-2, 1975-1977.

86. H. Nowotny, Destruction of Materials by Cavitation (in German), VDI-Verlag, Berlin, 1942.

87. D. G. Christie, G. W. Hayward, "Observations of Events Leading to the Formation of Water Drops Which Cause Turbine Erosion," Phi. Trans. Roy. Soc. (London), Series A, part 1100, 260, 1966, p. 183-192.

88. F. P. Bowden, "The Formation of Microjets in Liquids under the Influence of Impact or Shock," Proc. Roy. Soc. (London), Series A, 260, no. 1110, 1966, 94-95.

89. K. N. Letson and P. A. Ormsby, "Rain Erosion Testing of Slip Cast Fused Silica at Mach 5," ASME paper 76-ENAS-6, 1976.

List of Figures

List of Figures (cont.) Chap. VI-A and B

TABLES

Solid Material	$\rho_s C_s$ Kg/(m^2 - sec)	$1 + \frac{\rho_o C_o}{\rho_s C_s}$	Droplet Shape	Max. Impact Pressure $p_{max}/\rho_o C_o V_o$	$\frac{p_{Elastic}}{p_{Rigid}}$
Rigid	∞	1.0	Cylinder	1.34	1.0
			Sphere	1.06	1.0
Aluminum	1.74×10^6	1.086	Cylinder	1.17	0.873
			Sphere	0.861	0.812
PMMA	$.267 \times 10^6$	1.557	Cylinder	0.75	0.560
			Sphere	0.613	0.578

861

Table 1 The Maximum Pressure of Various Impact Situations $M_{liq.} = 0.2$

TABLE 2

Effect of V_o on Values of K and n for Material C-2, an Epoxy Laminate.

V_o (f/s)	n	K ($\times 10^5$)
0	6.44	25.7
200	6.36	27.9
400	6.24	29.7
600	6.08	32.3
800	5.87	34.8
1000	5.59	36.7
1200	5.22	39.6
1400	4.73	43.4
1600	4.09	41.3
1800	3.28	40.1
2000	2.28	28.4

TABLE 3

Results of Evaluation of Equation MDPR $\sin^a \theta = [K(V-V_o)\sin\theta]^n$ for Various Values of n.

Material D-2. (Ref. 70)
(Inorganic Laminate)

n	Threshold Velocity (f/s)	Minimum Probable Error (μ/s)	Probable Error for $V_o = 0$ (μ/s)
1.0	1100	82	146
1.5	1000	88	143
2.0	900	95	141
2.5	800	101	140

Material I-2. (Ref. 70)
(Thermal Plastics)

1.0	350	7.3	7.7
1.5	200	7.3	7.4
2.0	100	7.2	7.3
2.5	0	7.2	7.2

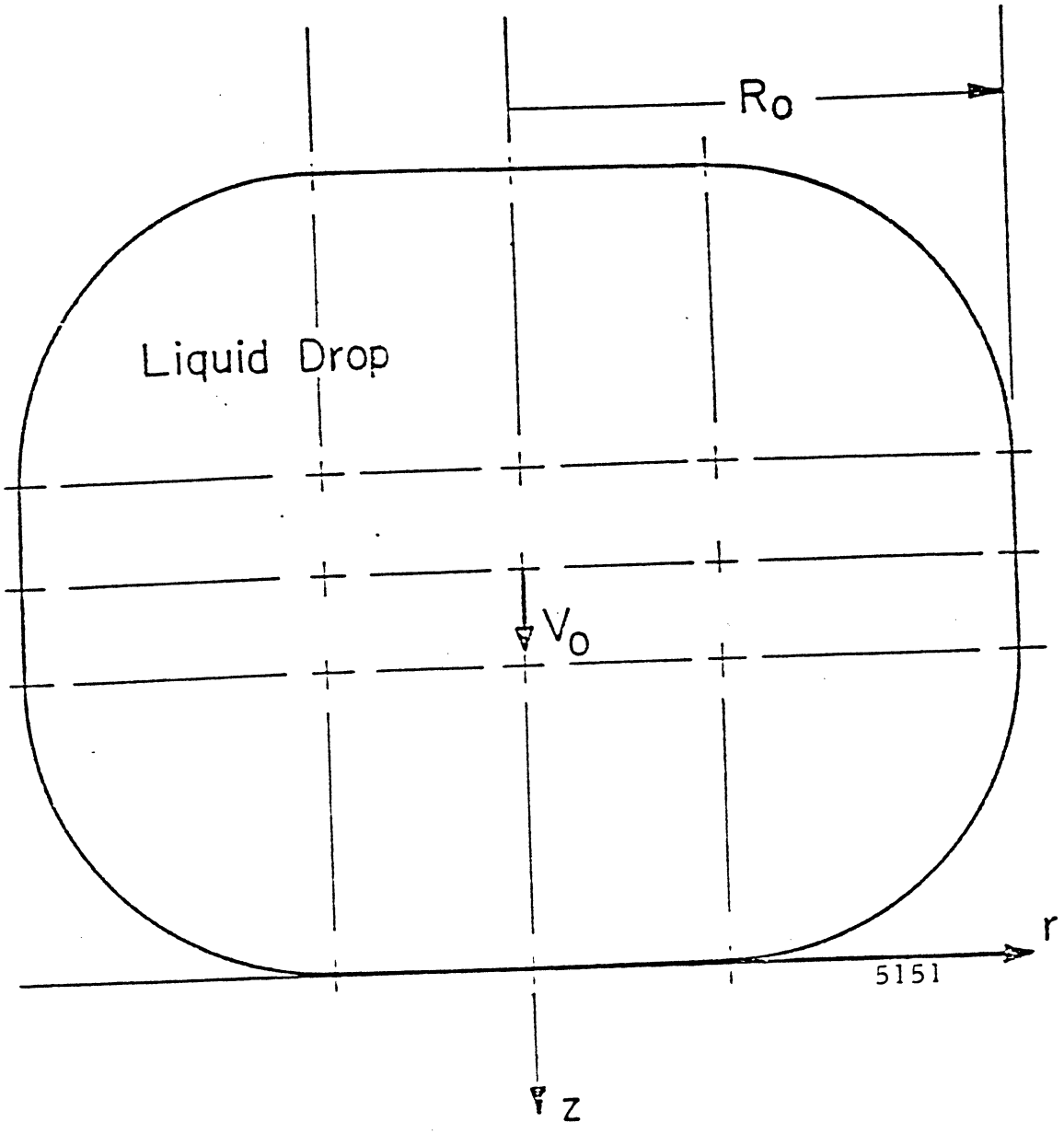

Fig. 1. Problem Geometry

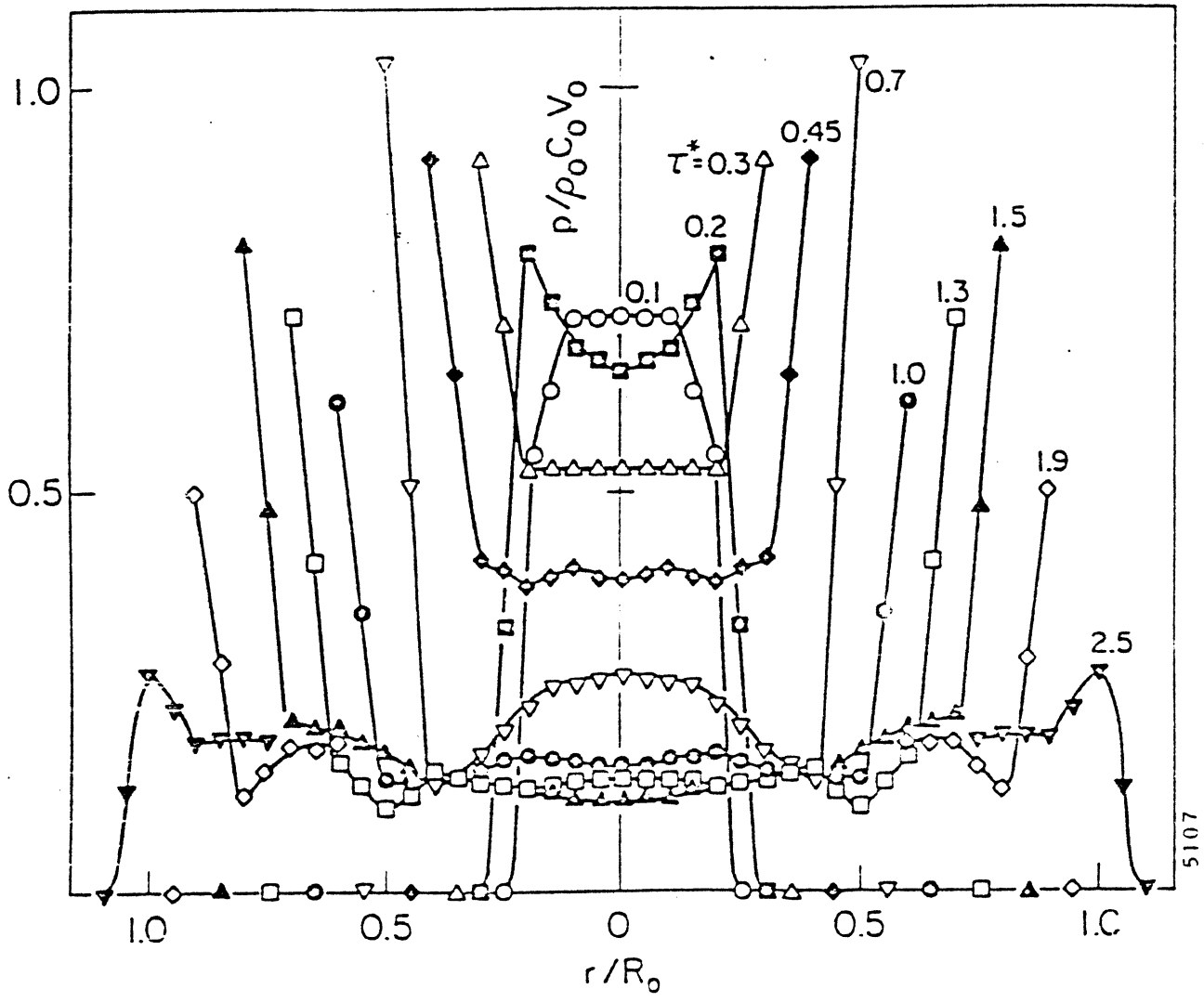

Fig. 2 Pressure Distribution on the Liquid-Solid Interface at Several Instants after the Collision of a Spherical Water Drop and a Rigid Plane.

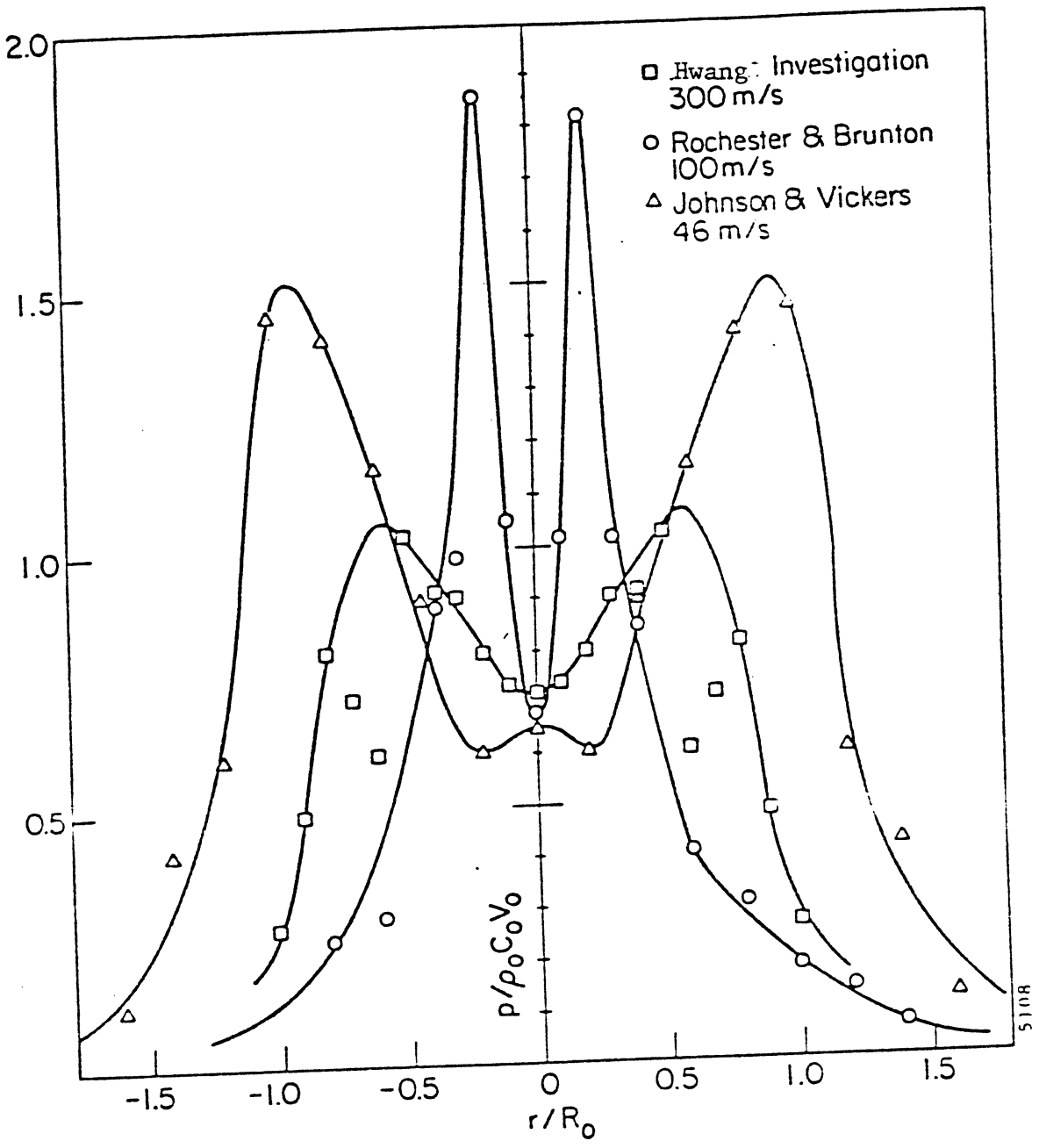

Fig. 3. Distribution of Maximum Pressure on the Liquid-Solid Interface (z = 0). Data from Present Investigation and Published Literatures.

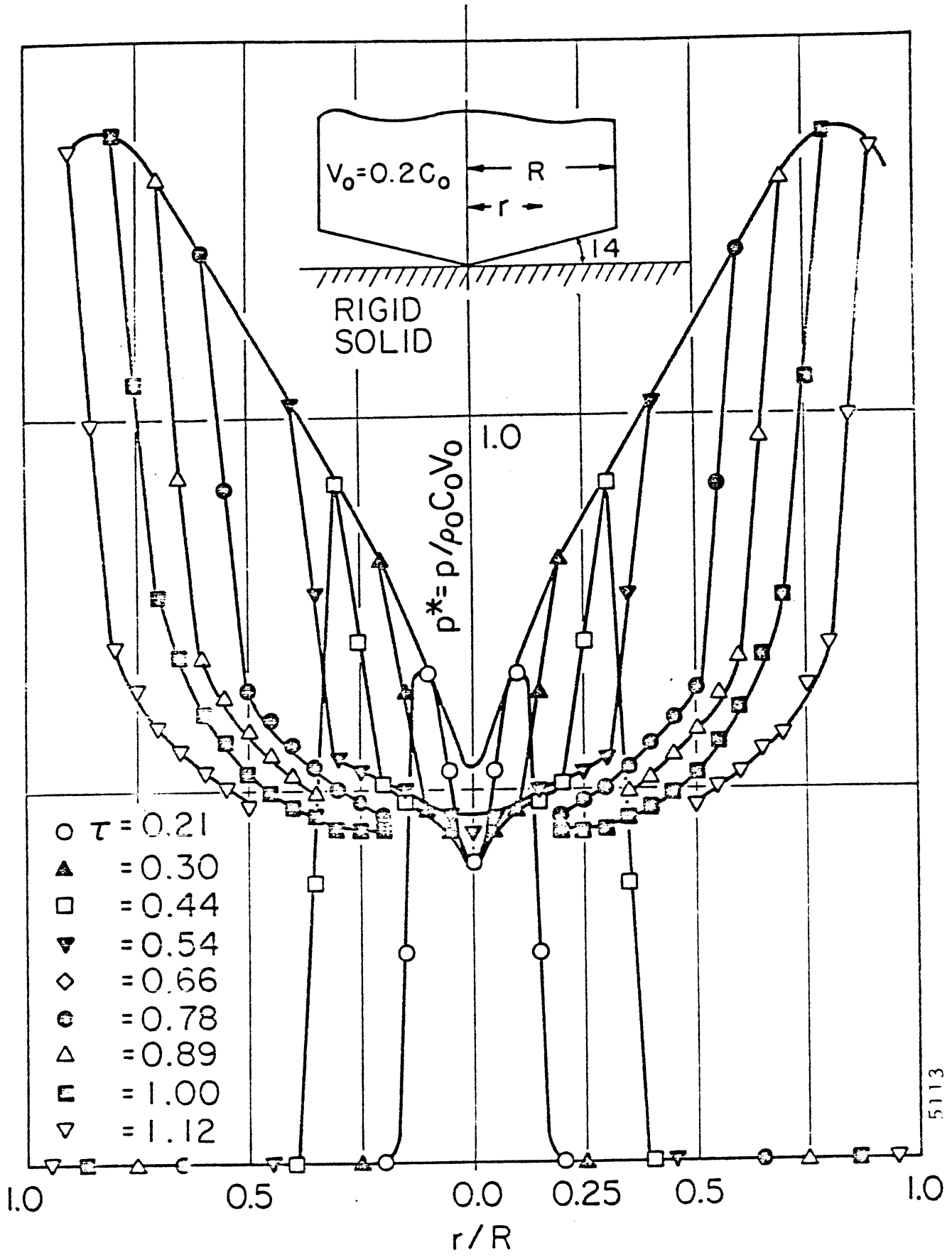

Fig. 4. Pressure Distribution on the Interface (z = 0) at Several Instants following the Collision of a Conical Water Droplet and a Rigid Plane.

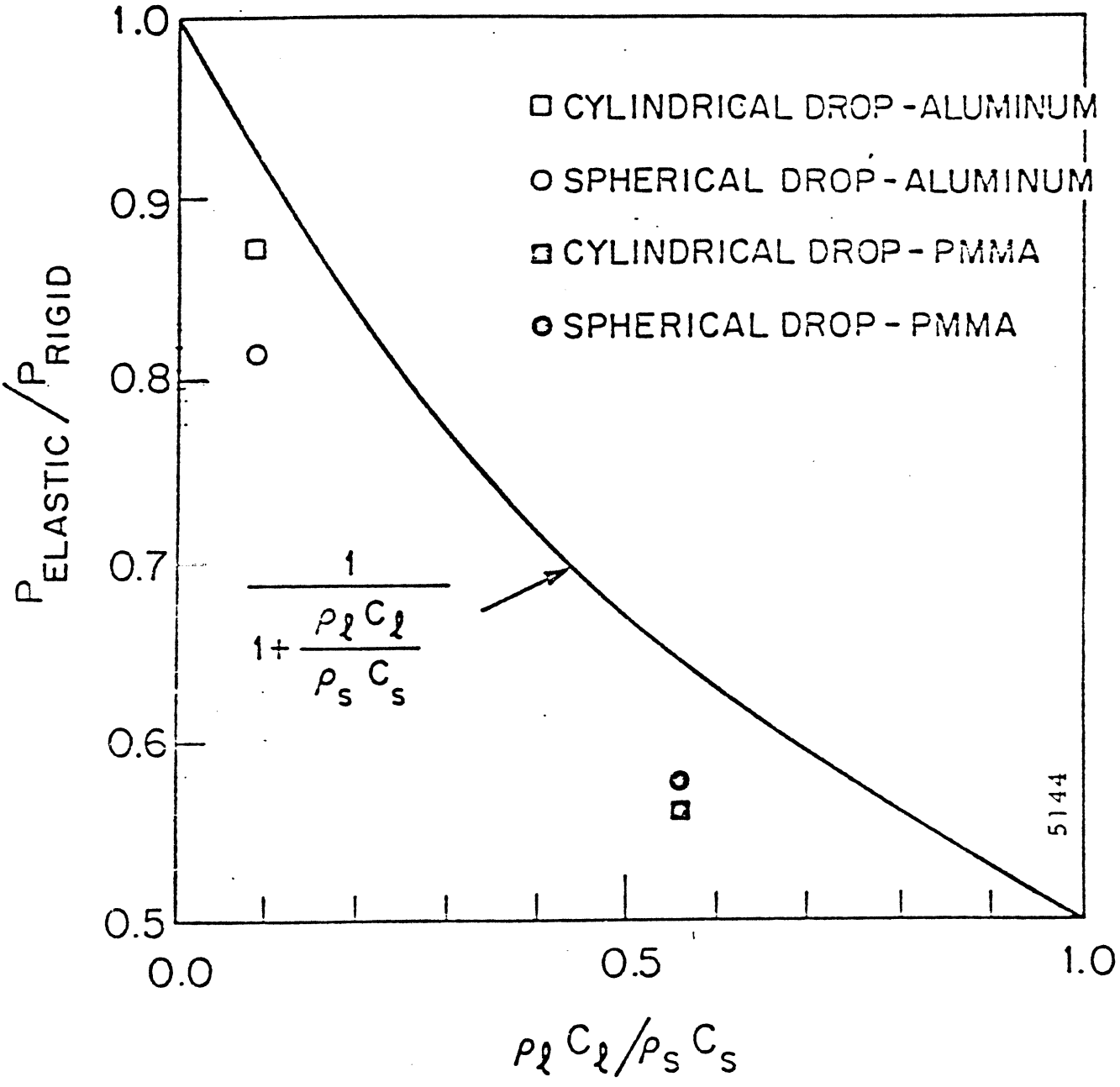

Fig. 5. The Reduction of Impact Pressure as a Function of the Ratio of Acoustic Impedance.

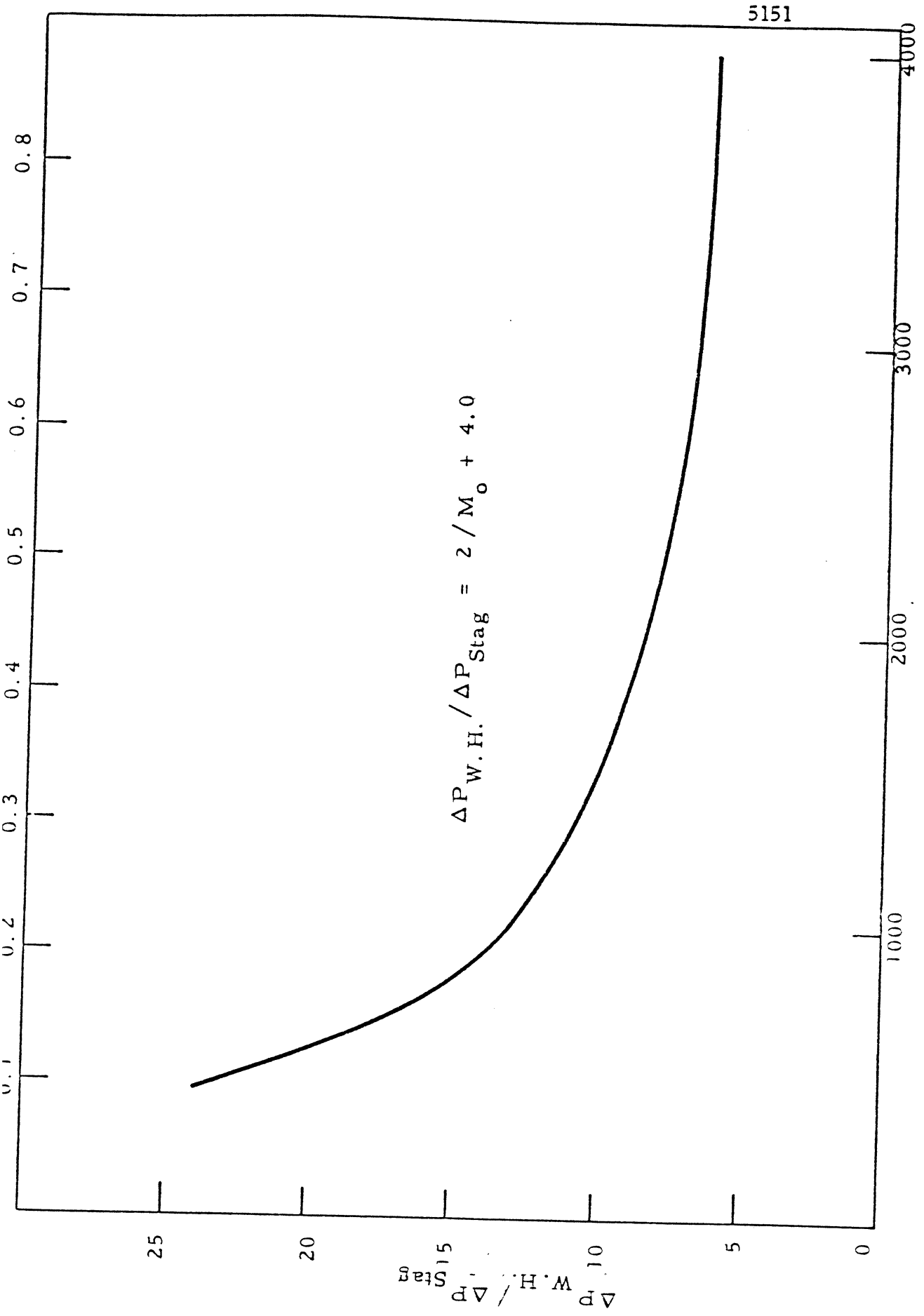

Fig. 6 Ratio of Water Hammer to Stagnation Pressure Rise Vs. Impact Velocity

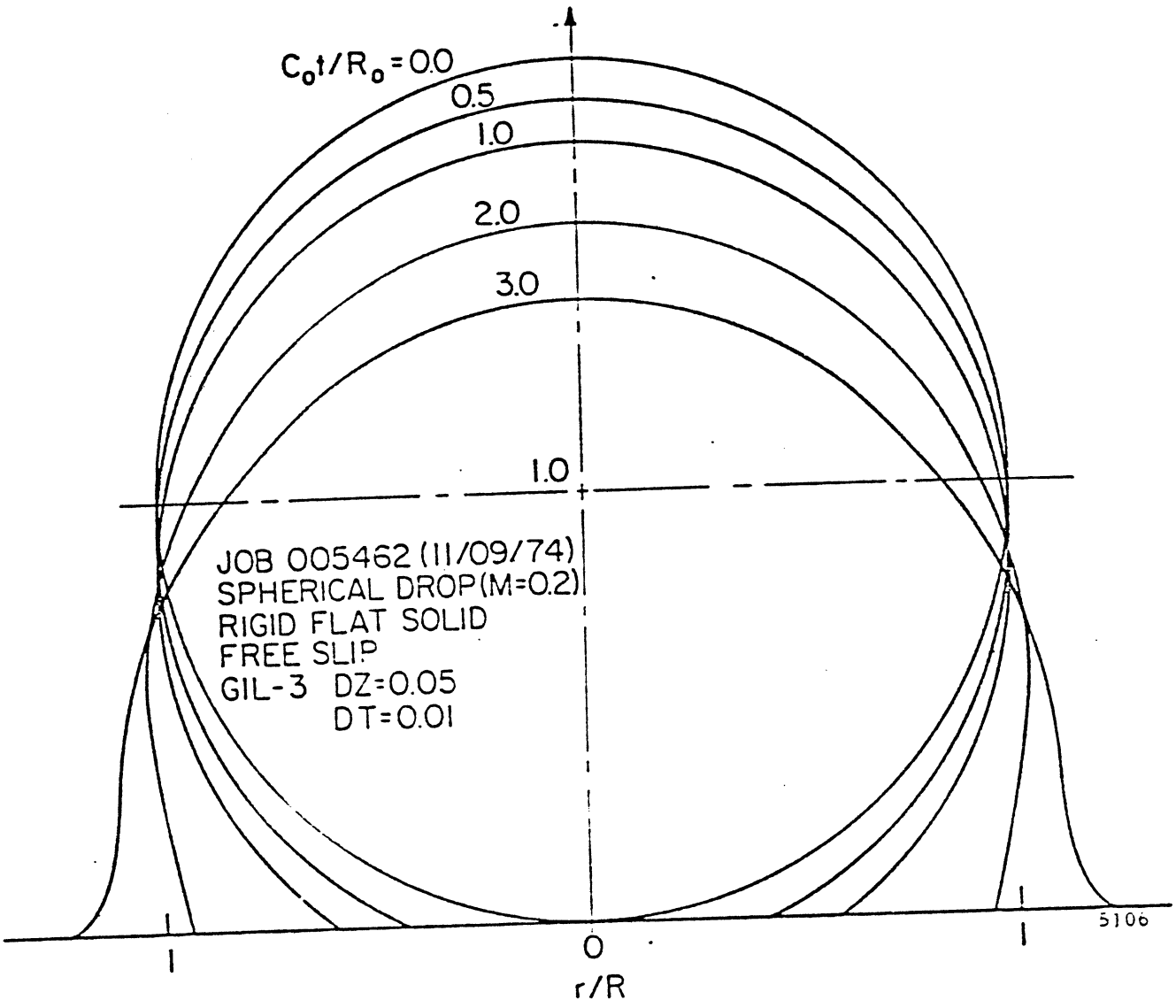

Fig. 7 Shape History of an Initially Spherical Water Drop following the Collision with a Rigid Plane.

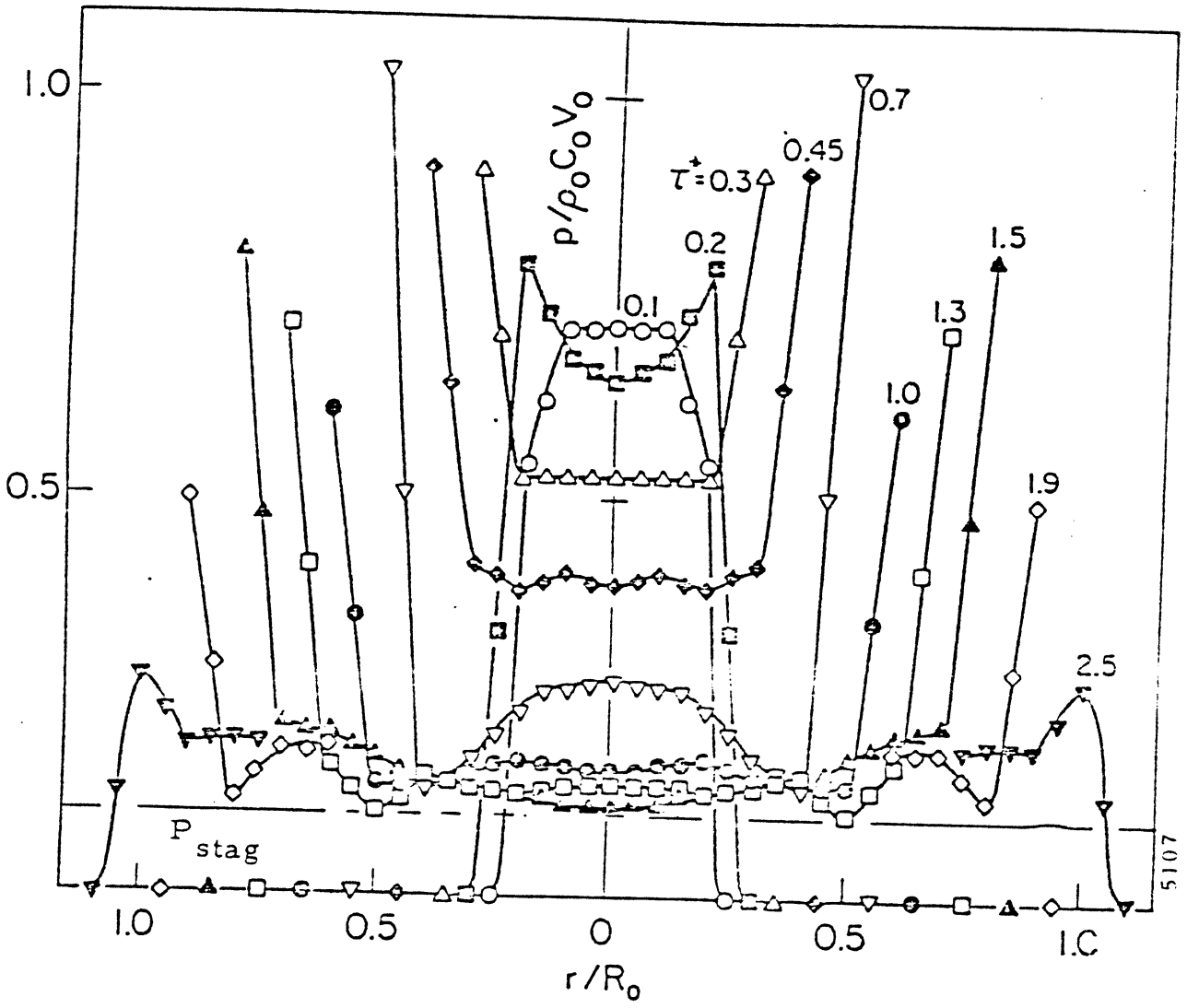

Fig. 8 Pressure Distribution on the Liquid-Solid Interface (z = 0) at Several Instants after the Collision of a Spherical Water Drop and a Rigid Plane.

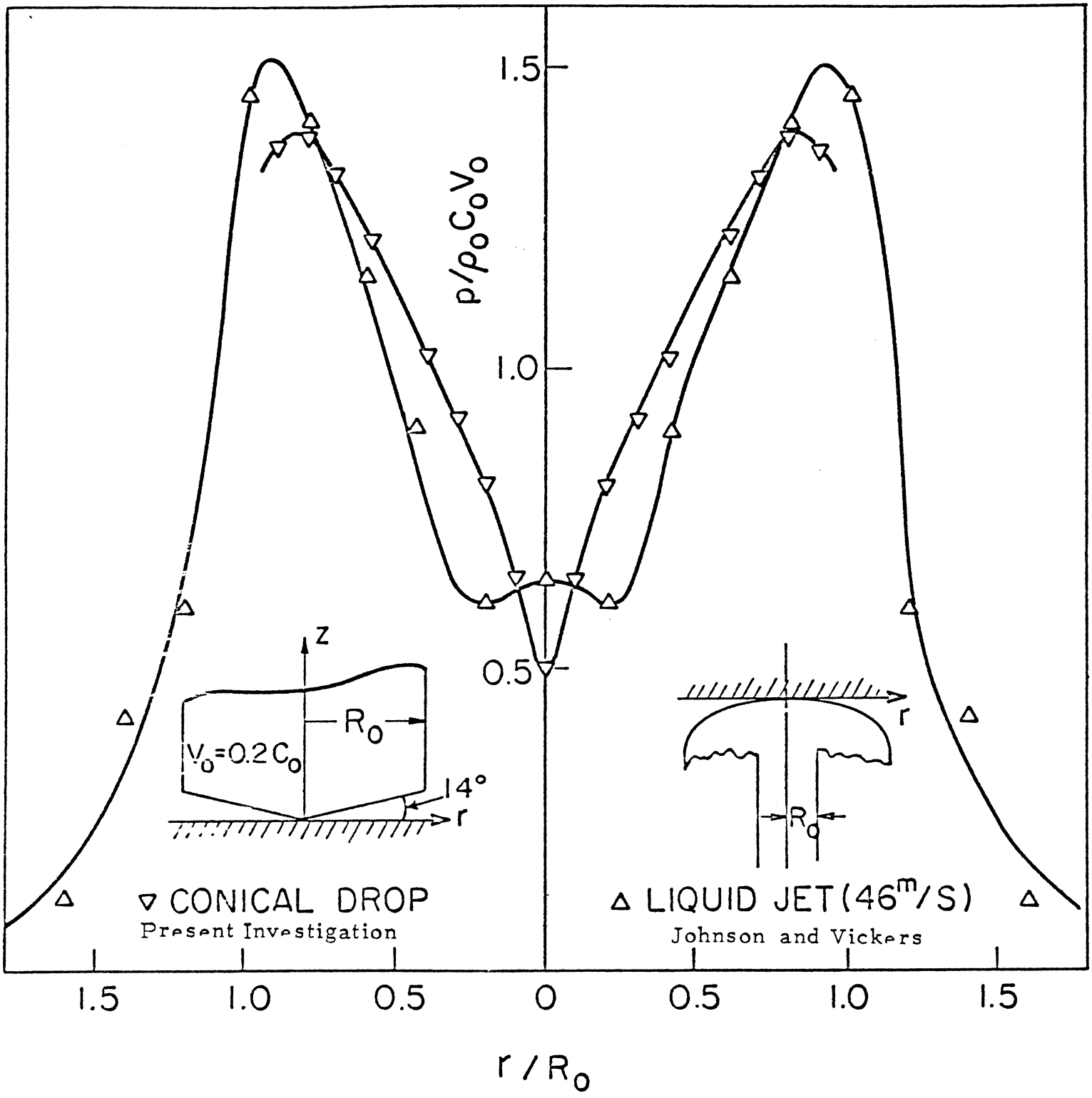

Fig. 9 The Distribution of Maximum Pressure on a Rigid Plane due to the Impact of a Conical Drop ($V_o = 0.2C_o$) and a Liquid Jet (46 m/sec)

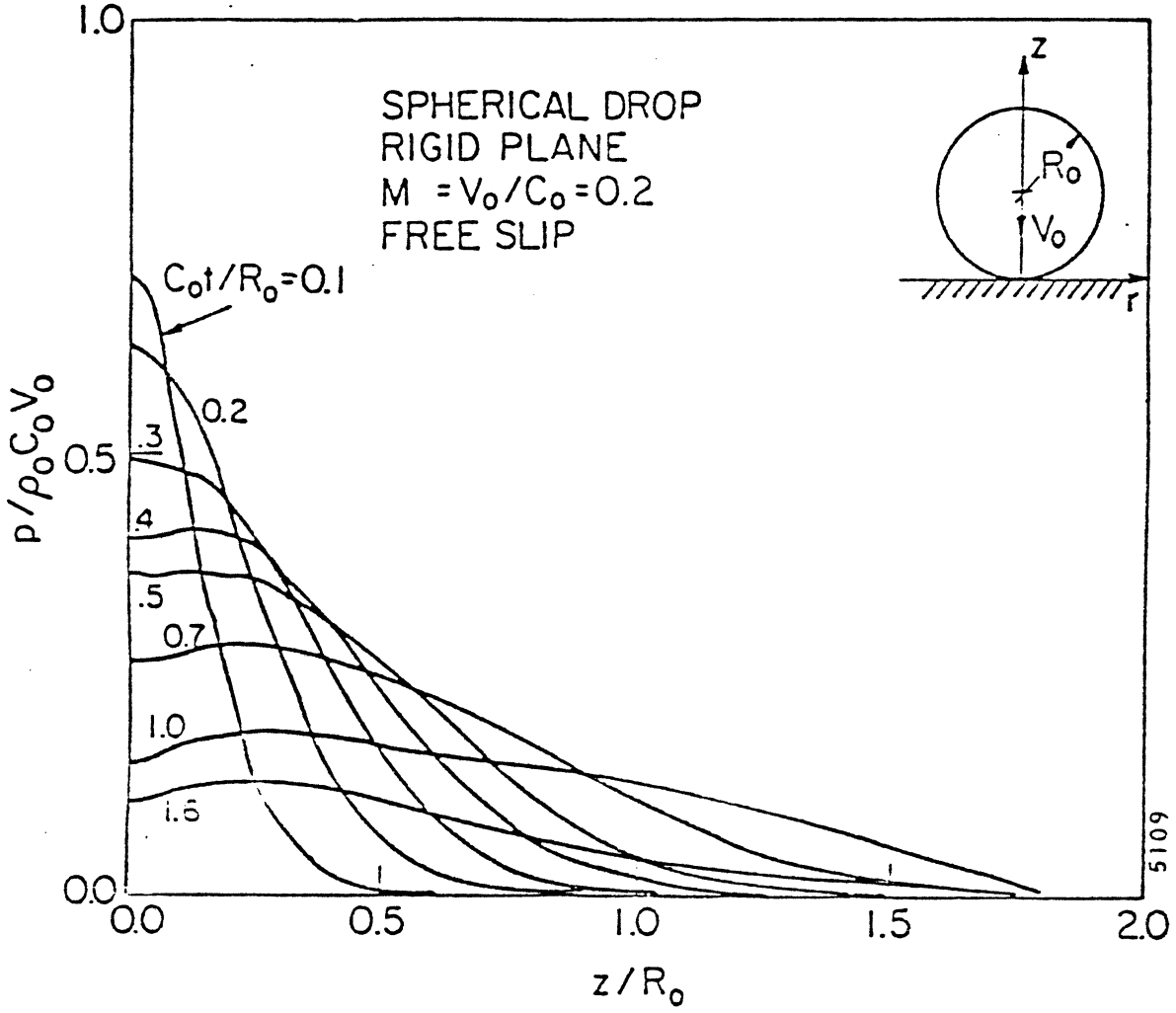

Fig. 10 Pressure Distribution on the Axis of Symmetry (r = 0) at Several Instants following the Collision of a Spherical Drop and a Rigid Plane.

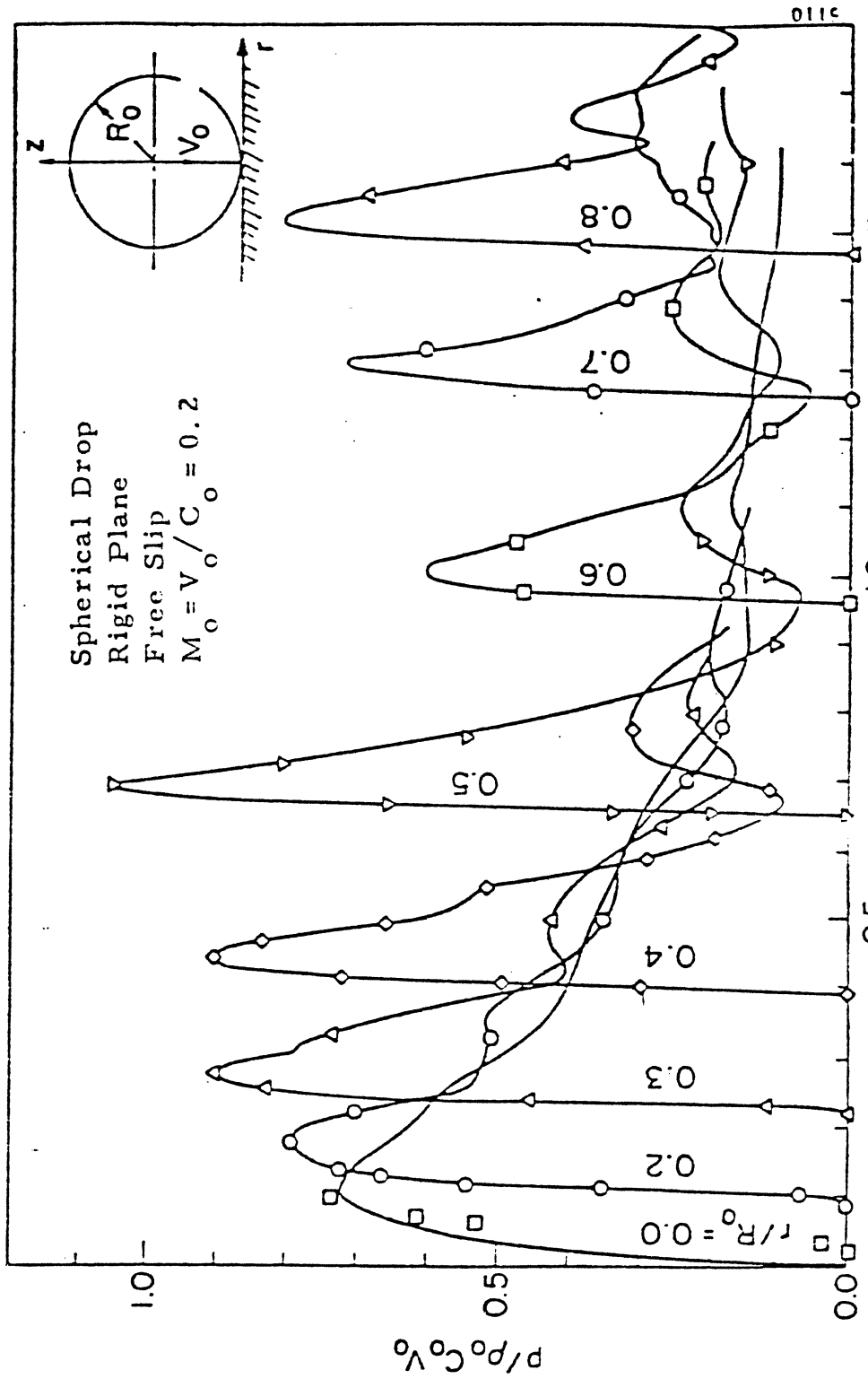

Fig. 11 Transient Pressure at Selected Locations on the Interface following the Collision of a Spherical Water Droplet and

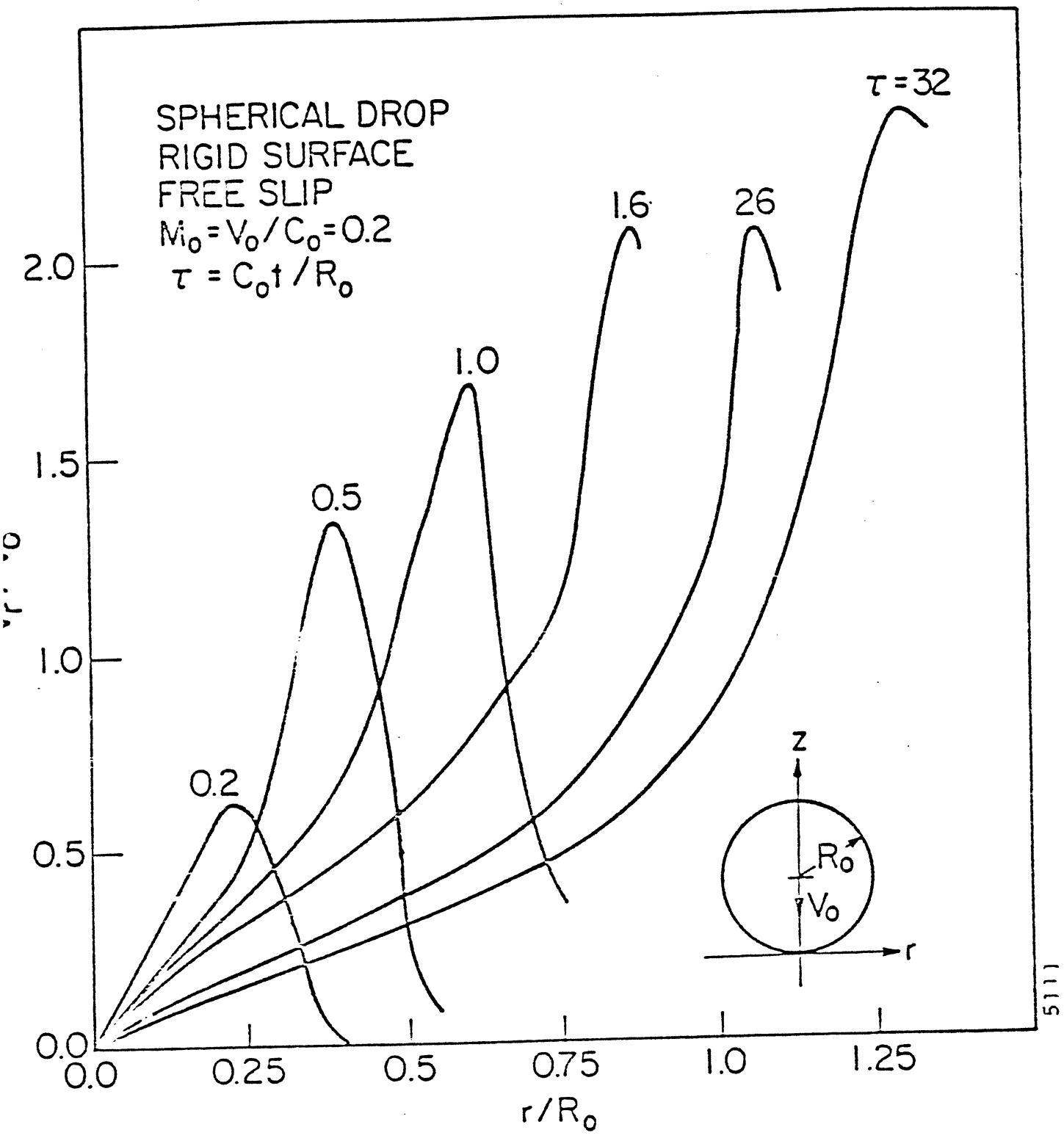

Fig. 12 Radial Velocity on the Liquid-Solid Interface (z = 0) at several Instants following the Collision of a Spherical Water Drop and a Rigid Plane.

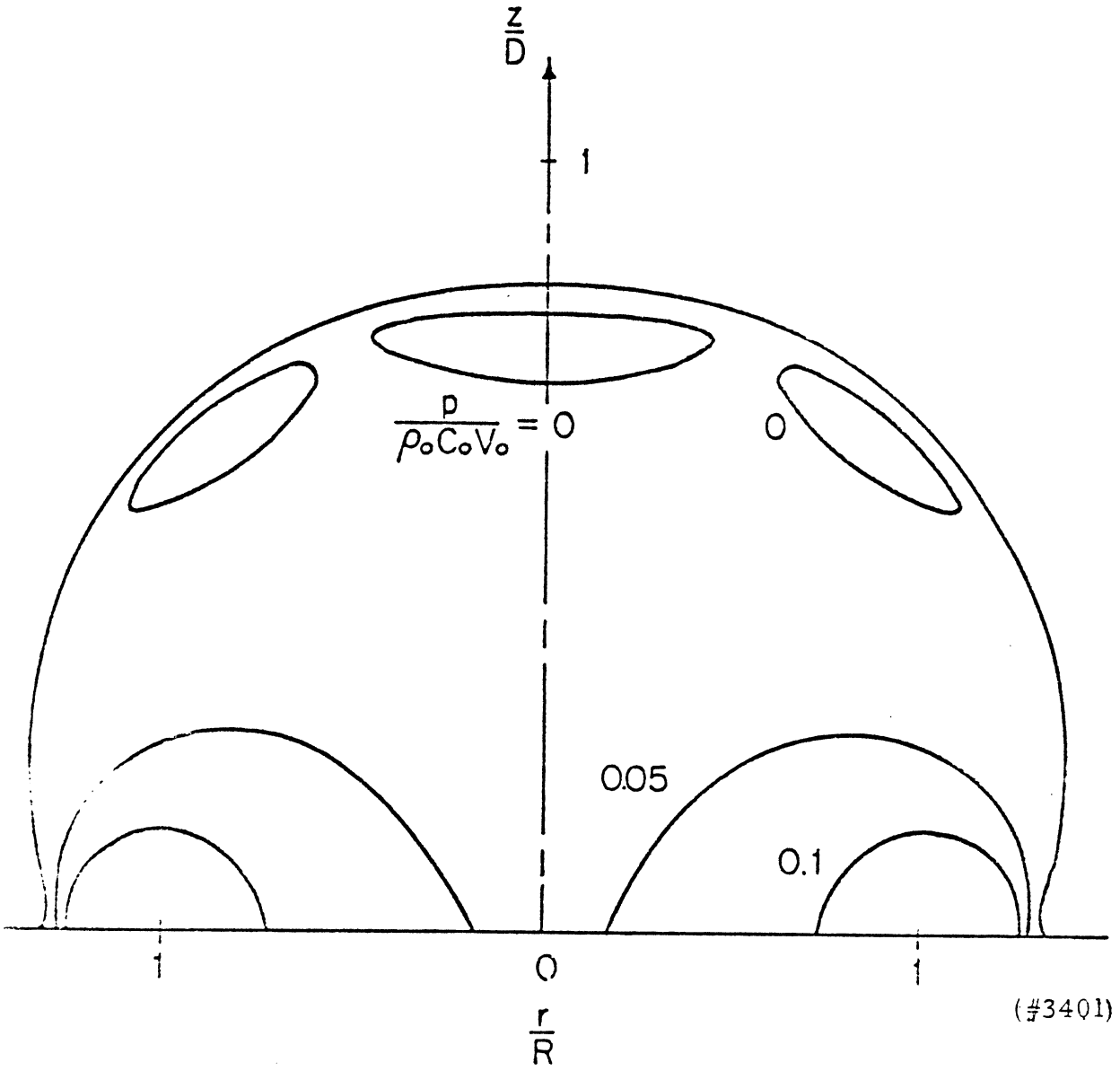

Fig. 13 Isobar Distribution in an Initially Cylindrical-Spherical Composite Droplet with $R_1/R = 0.25$ and $L/D = 1$, at Time $(Ct/D) = 1.5$ for Impact Mach Number of 0.2 and for Free-Slip Boundary Condition.

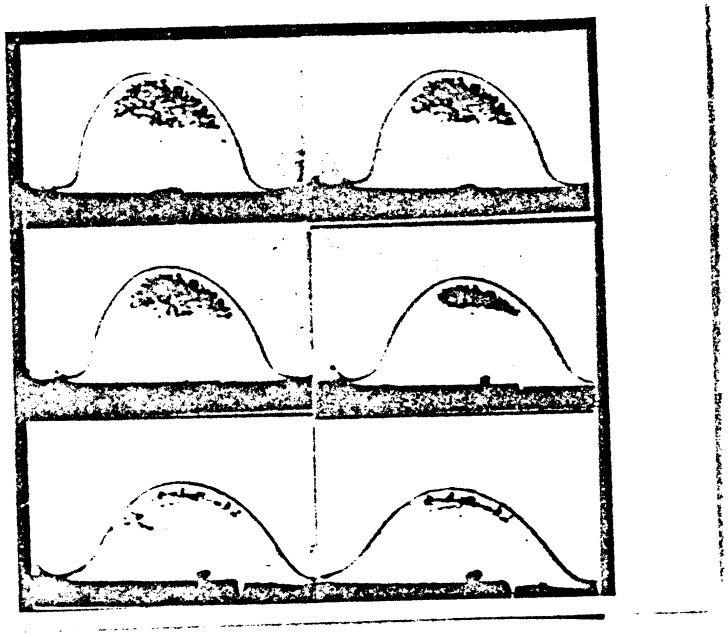

Fig. 14 Photographs of the Cavitation for a Water Droplet Following an Impact on a Solid Plane (Brunton and Camus, 27)

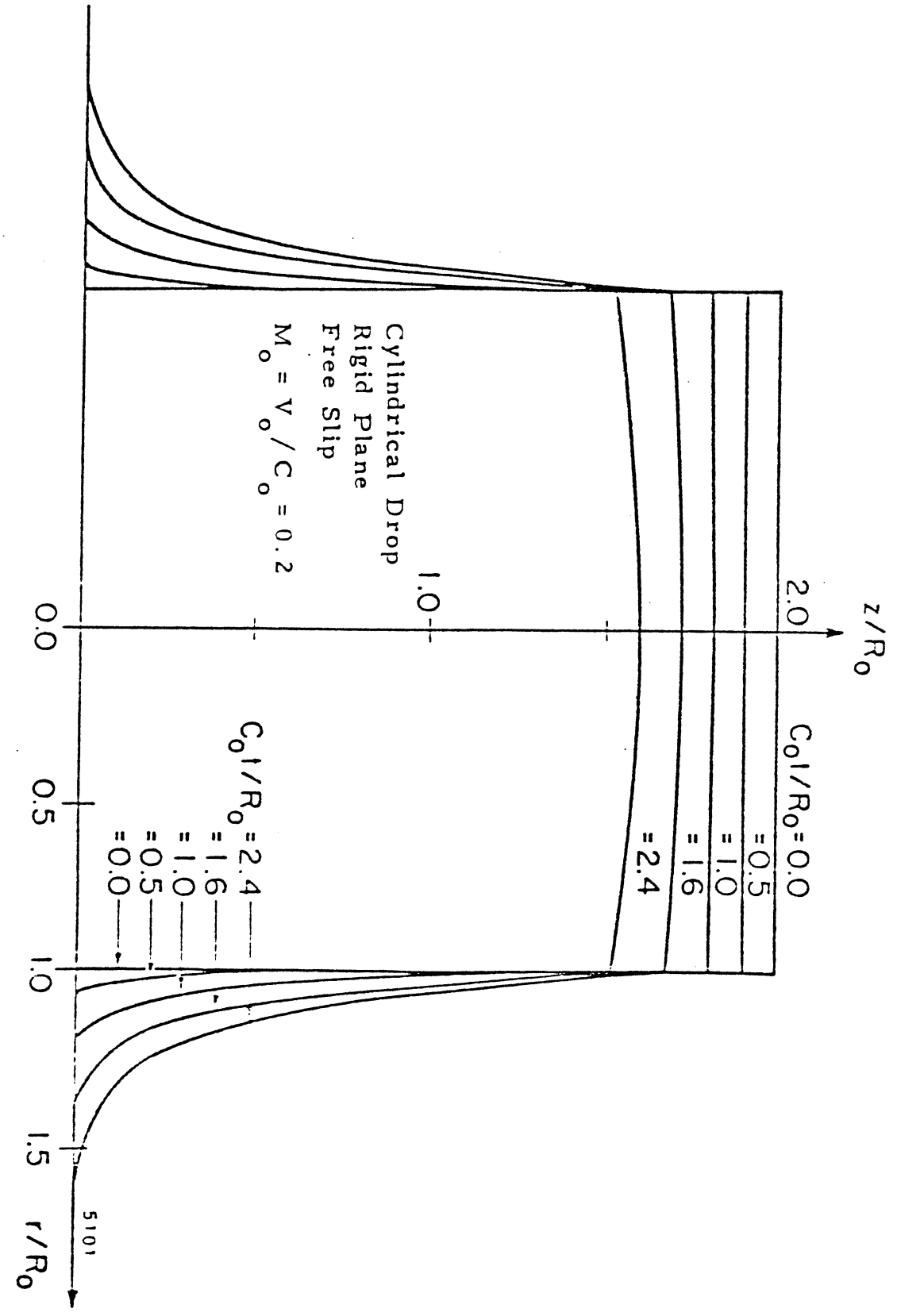

Fig. 15 Shape History of an Initially Cylindrical Water Drop Following the Collision with a Rigid Plane

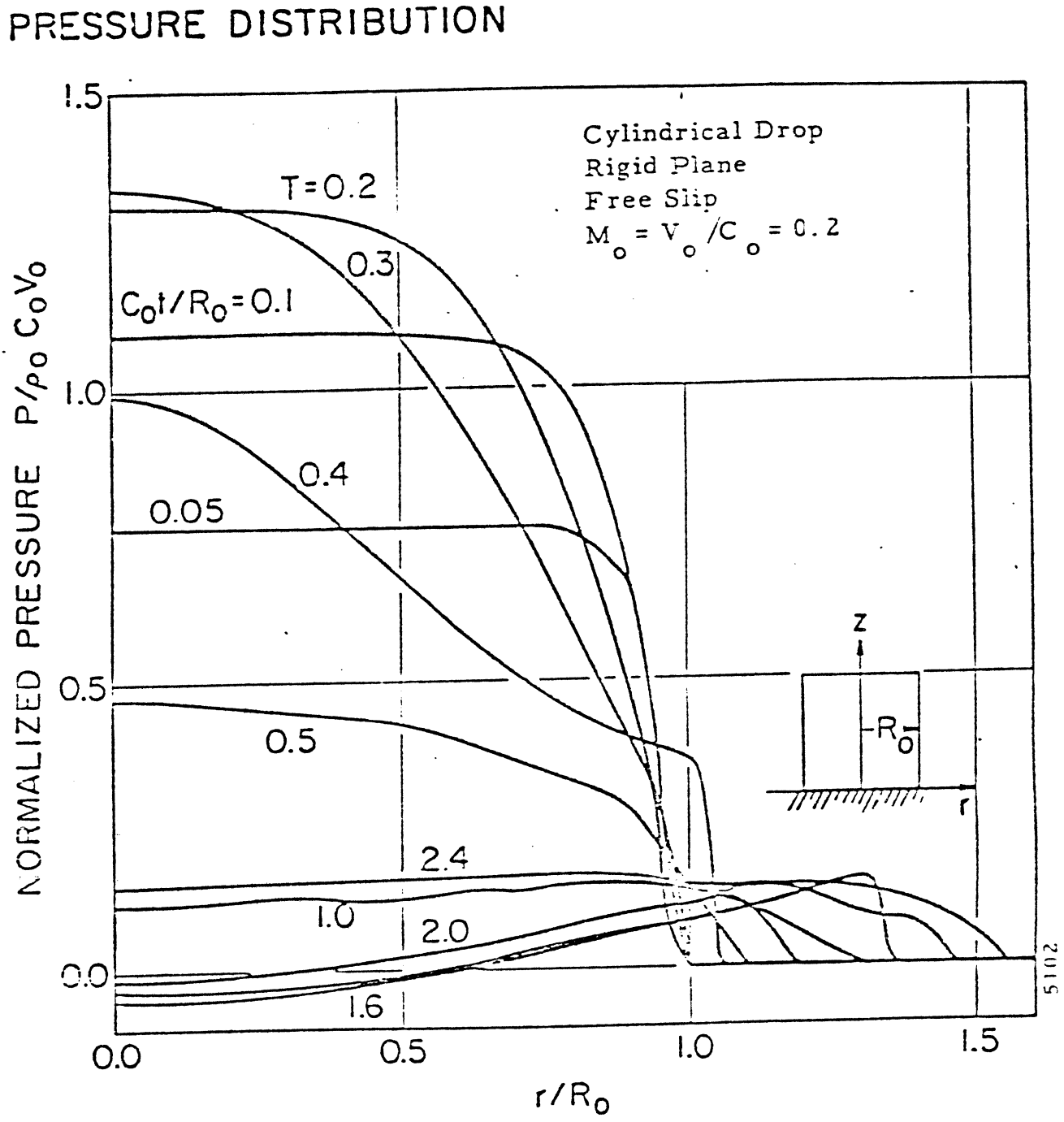

Fig. 16 Pressure Distribution on the Liquid-Solid Interface (z = 0) at Several Instants after the Collision of a Cylindrical Droplet and a Rigid Plane.

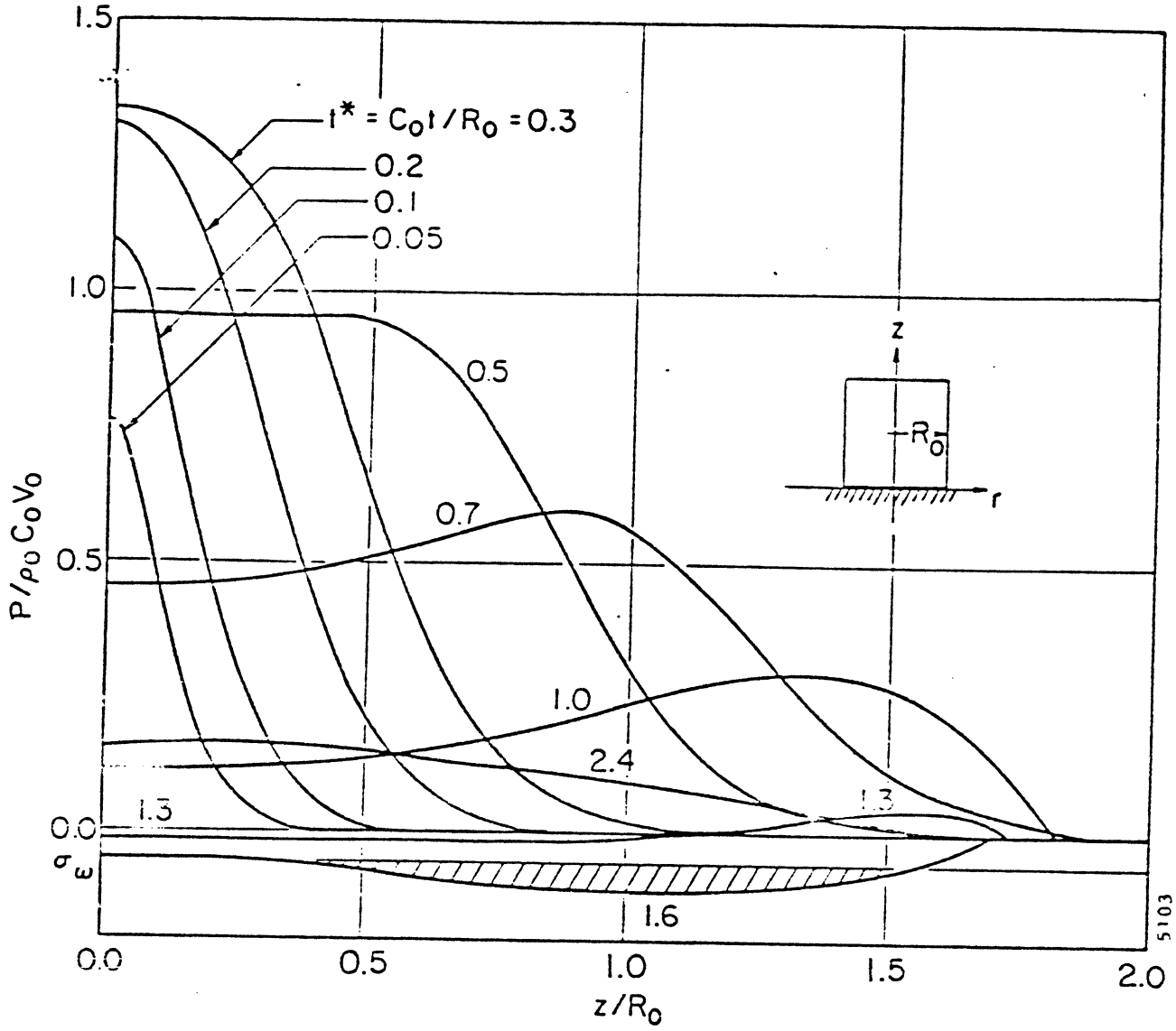

Fig. 17 Pressure Distribution on the Axis of Symmetry (r = 0) at Several Instants after the Collision of a Cylindrical Water Droplet and a Rigid Plane.

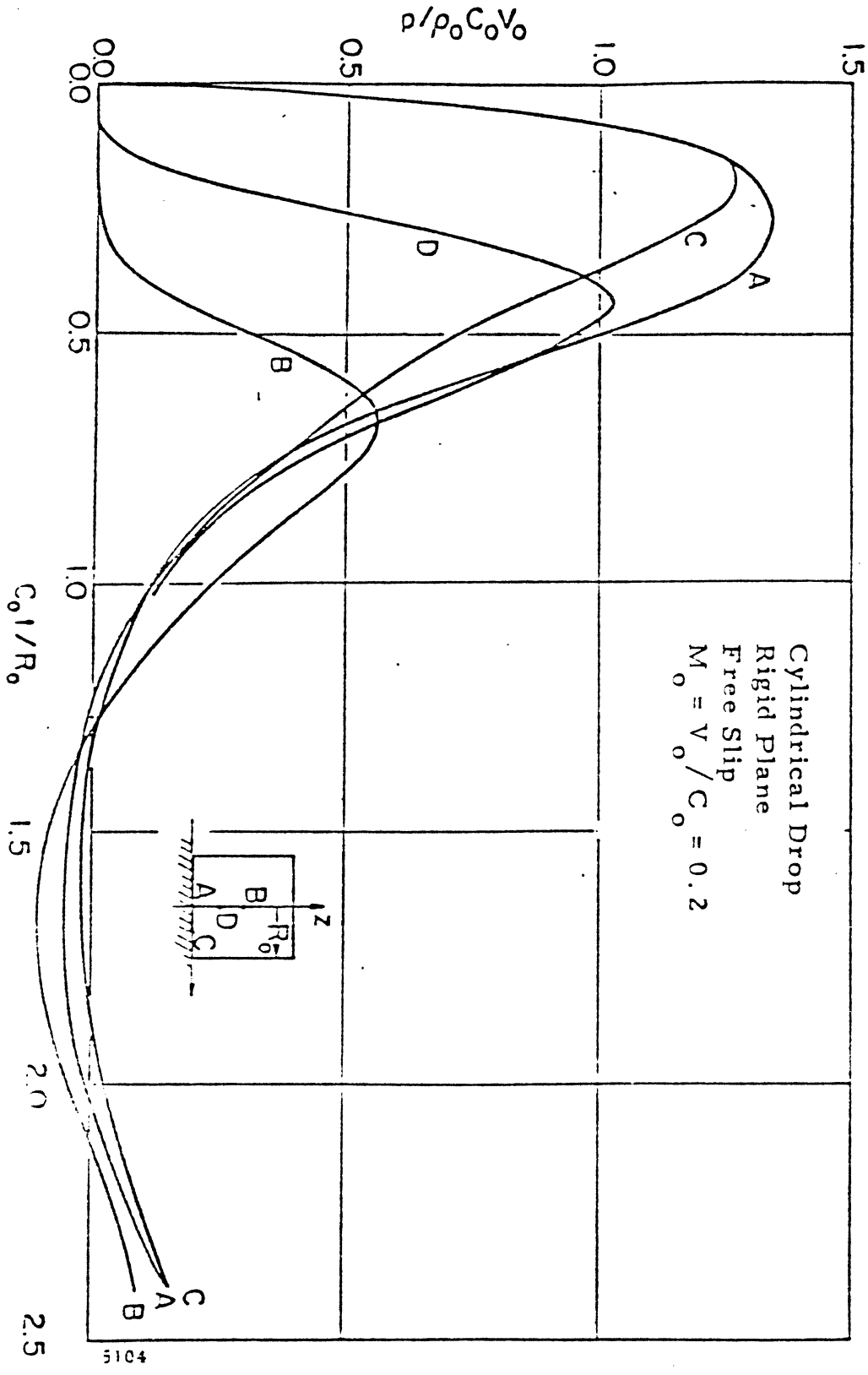

Fig. 18 Transient Pressure at Selected Locations inside an Initially Cylindrical Drop following the Collision with a Rigid Plane.

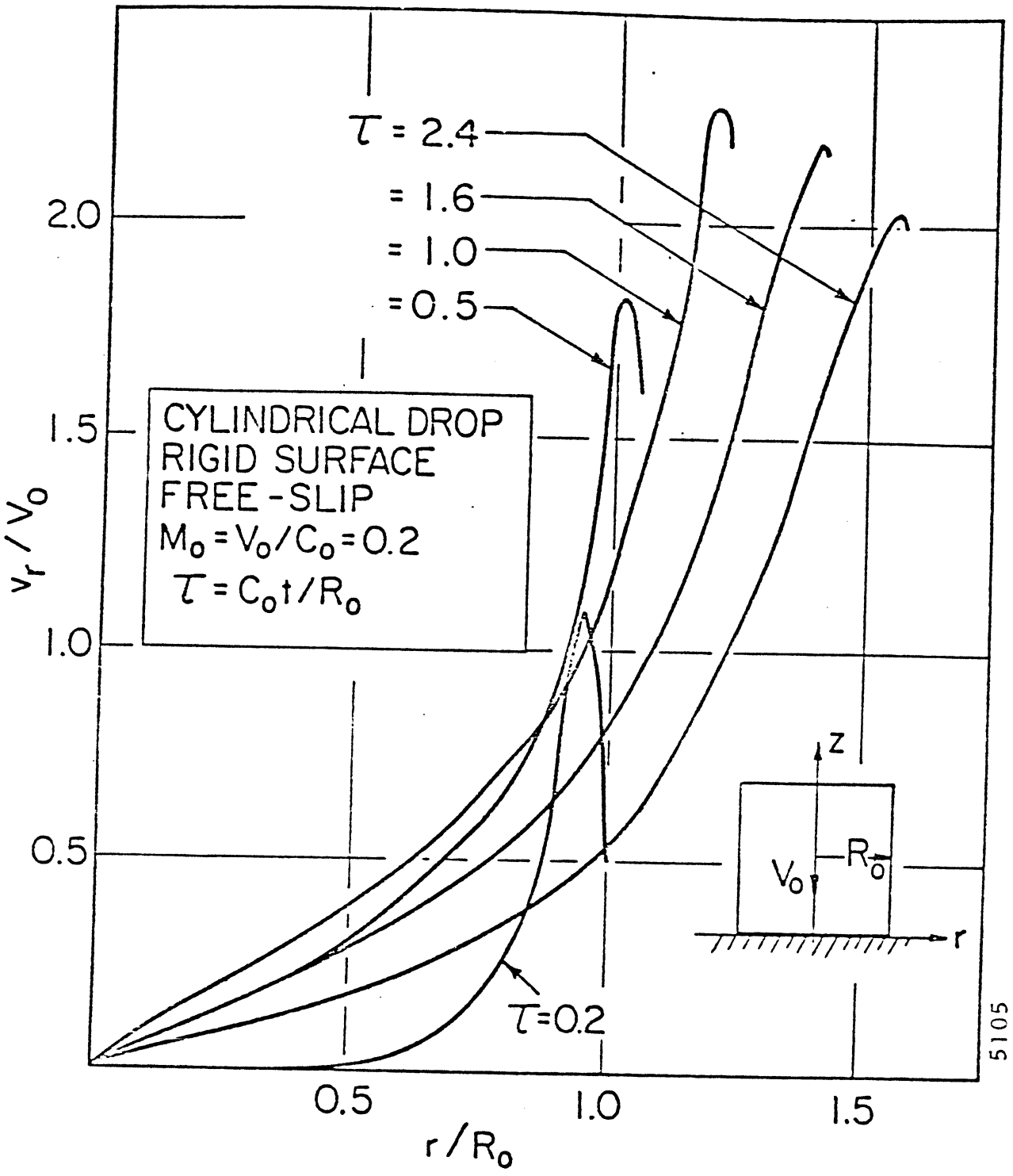

Fig. 19 Radial velocity on the Liquid-Solid Interface (z = 0) at Several Instants after the Collision of a Cylindrical Water Drop and a Rigid Plane.

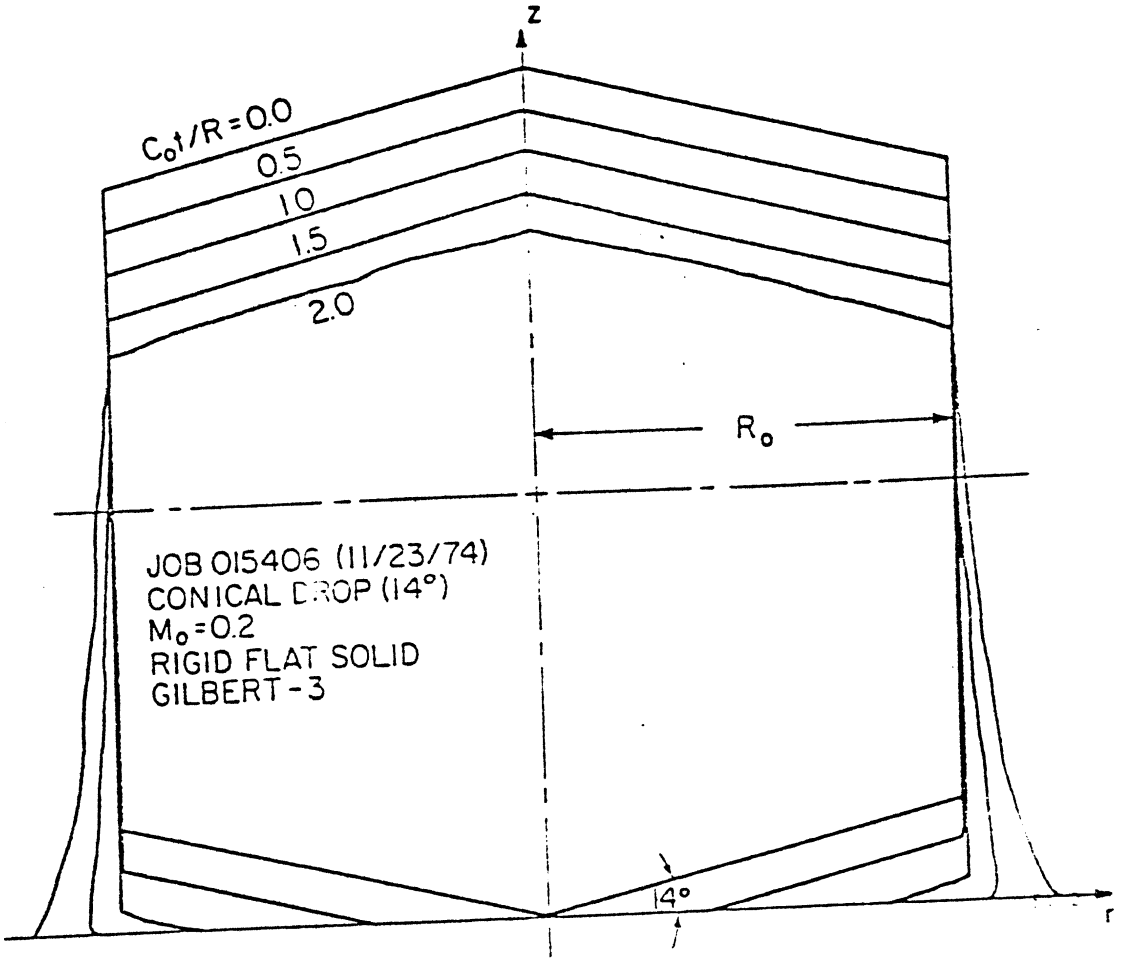

Fig. 20 Shape History of an Initially Conical Water Drop following the Collision with a Rigid Plane.

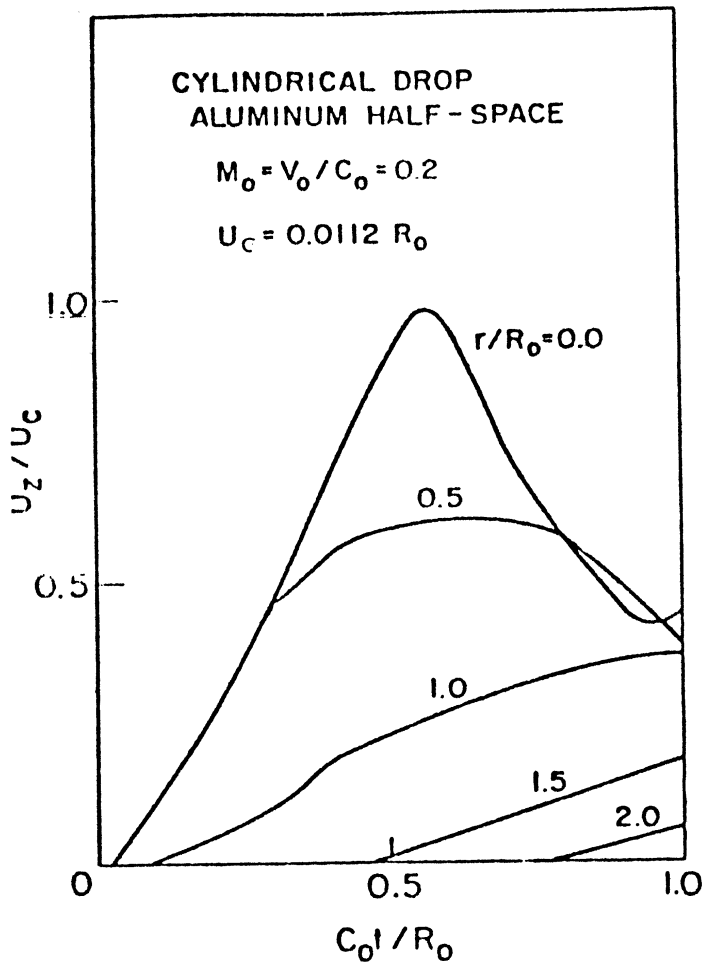

Fig. 21 Transient displacement on the surface of a semi-infinite aluminium body following the impact by a cylindrical water drop

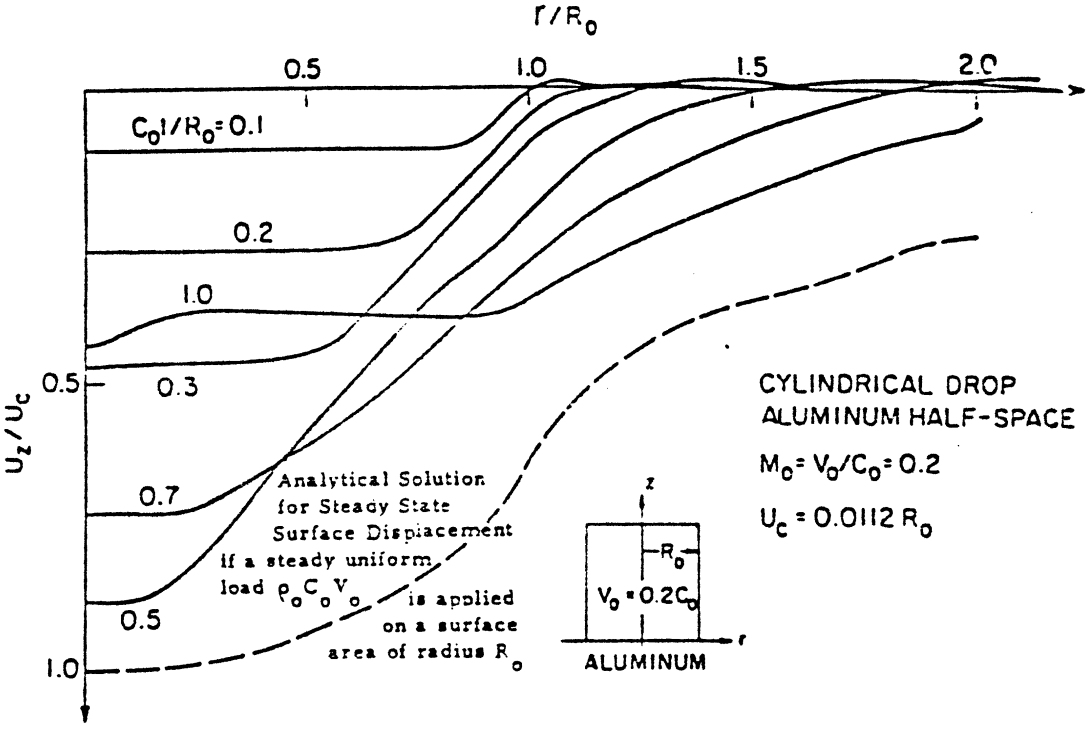

Fig. 22 Surface deformation of a semi-infinite aluminum body at several instants after the collision with a cylindrical water drop

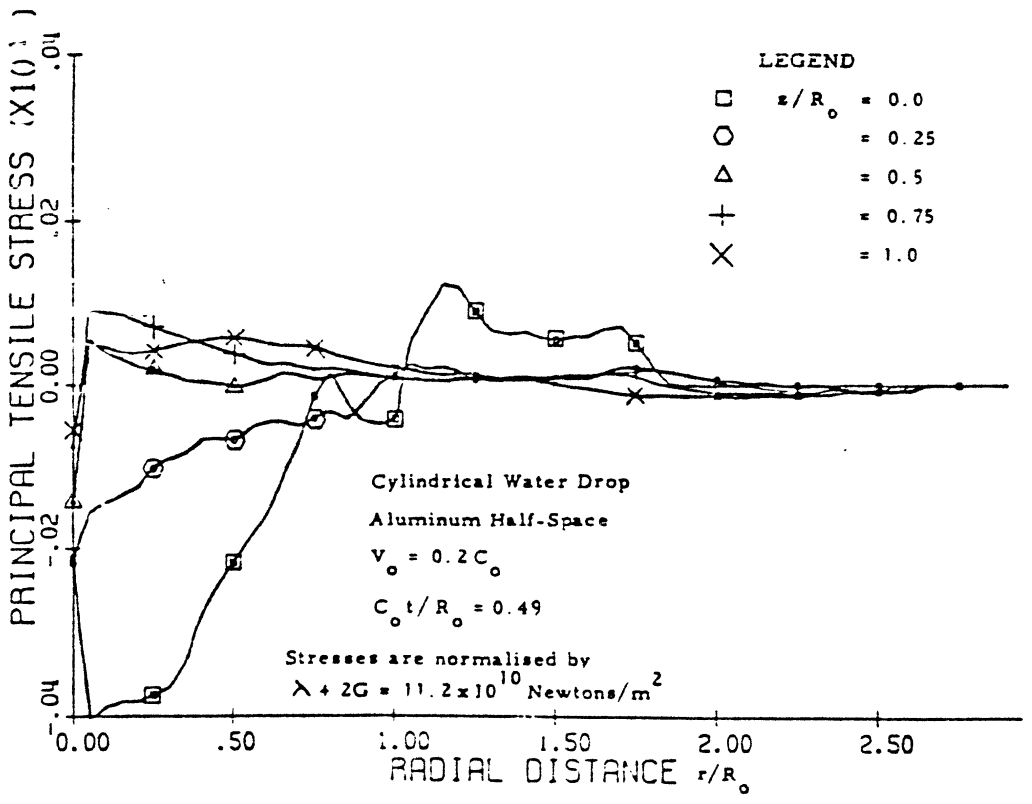

Fig. 23 Distribution of principal tensile stress at $C_0t/R_0 = 0.49$ after the collision of a cylindrical drop and a semi-infinite aluminium body

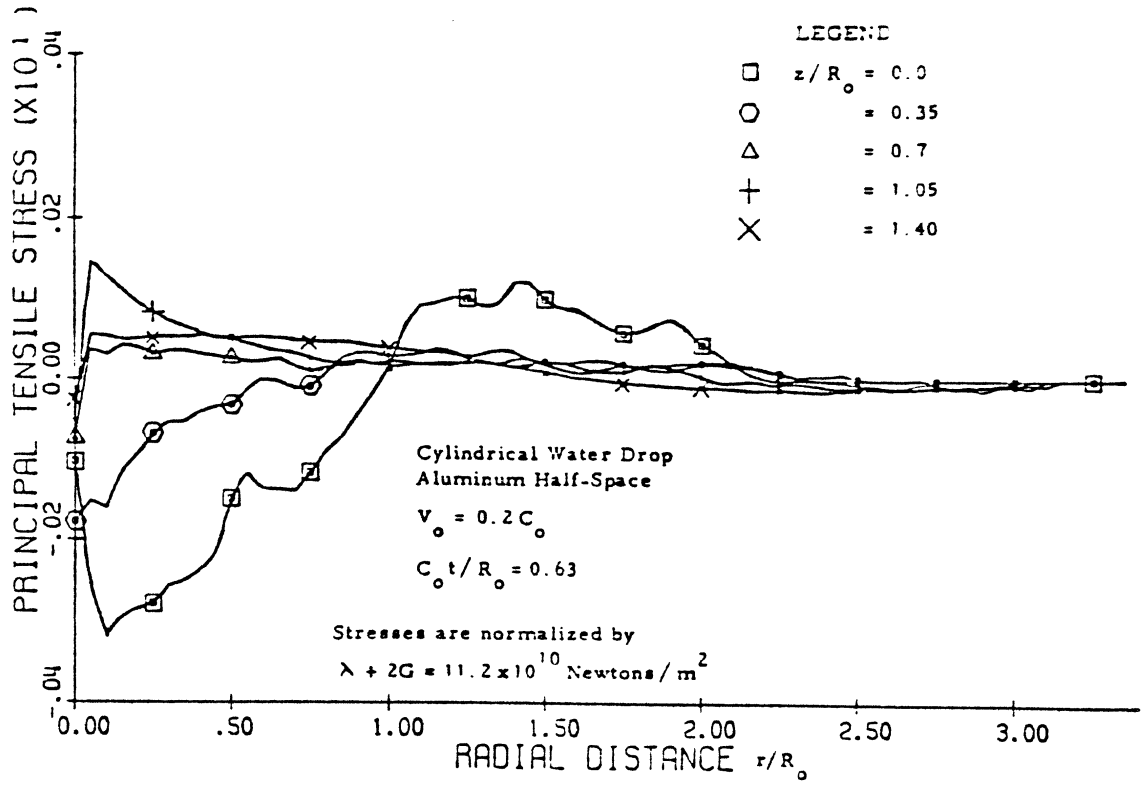

Fig. 24 Distribution of principal tensile stress at $C_o t/R_o = 0.63$ after the collision of a cylindrical drop and a semi-infinite aluminum body

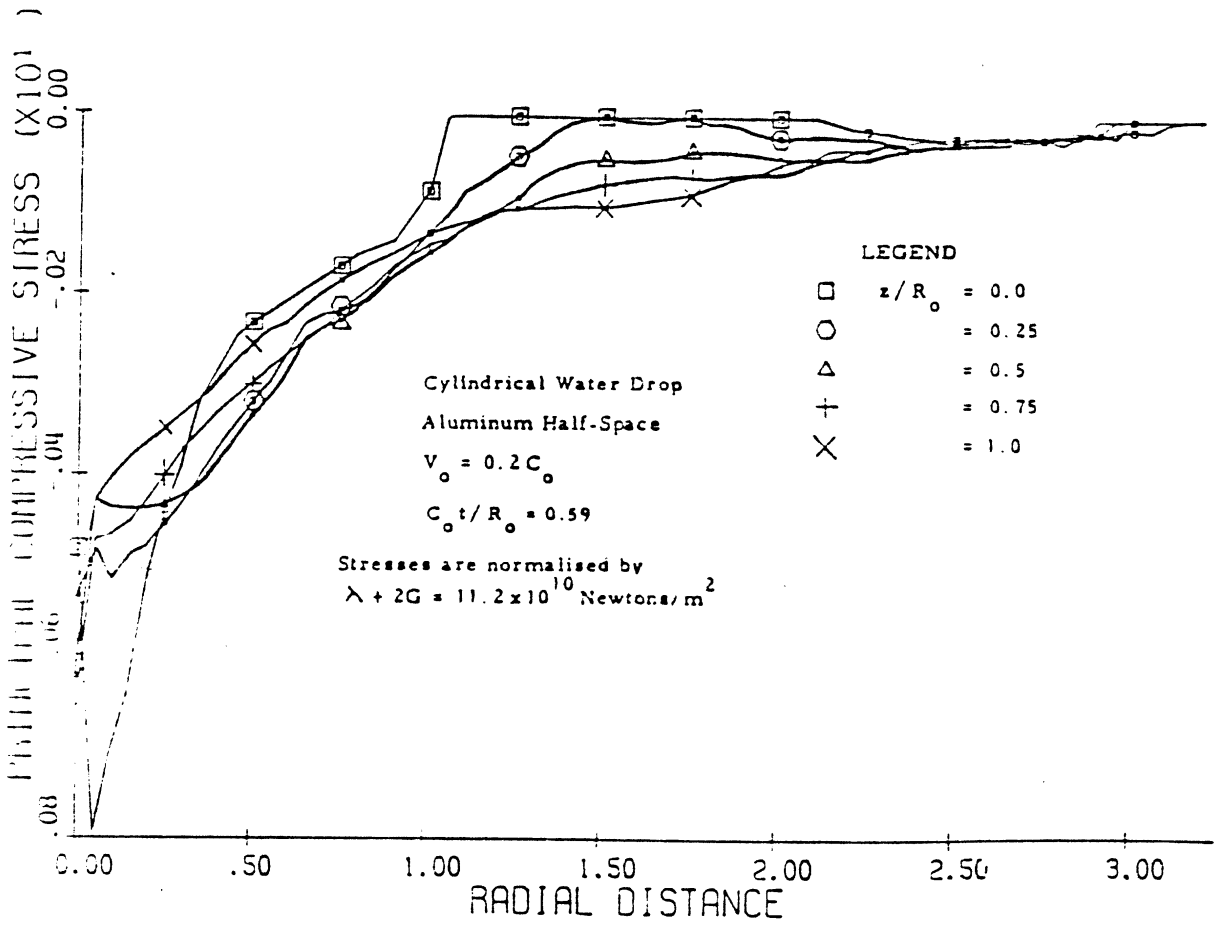

Fig. 25 Distribution of principal compressive stress at $C_o t/R_o = 0.59$ after the collision of a cylindrical drop and a semi-infinite aluminum body

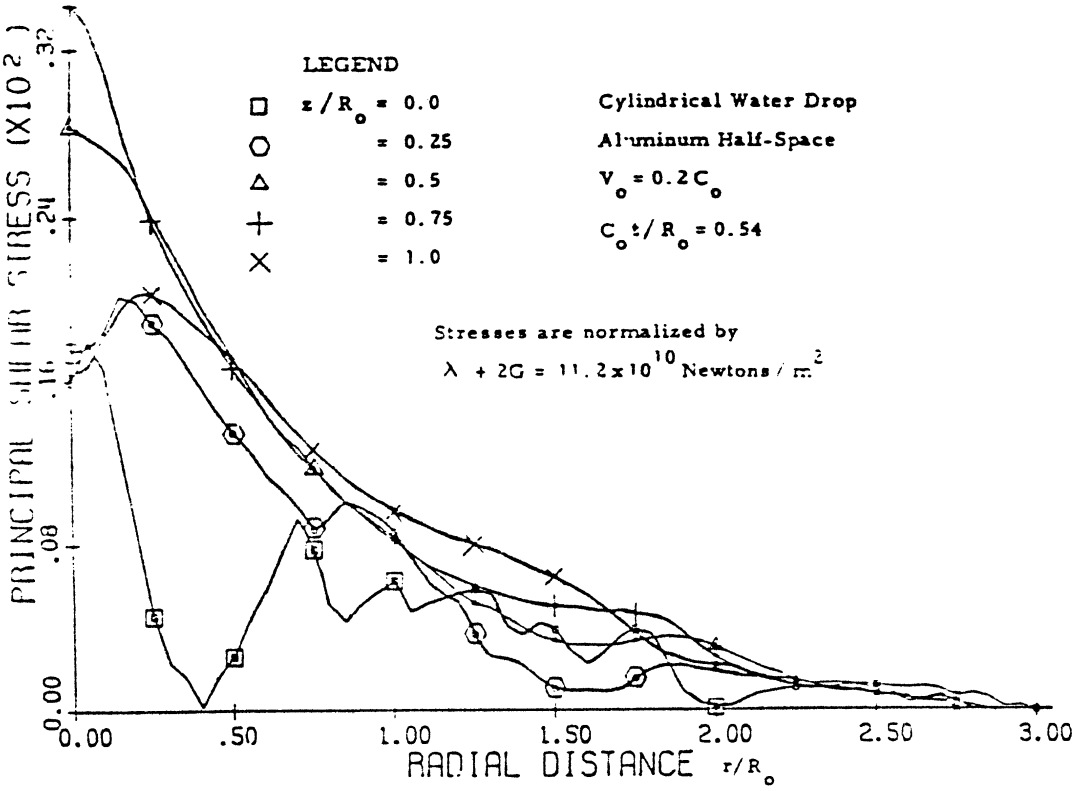

Fig. 26 Distribution of maximum shear stress at $C_o t/R_o = 0.54$ after the collision of a cylindrical drop and a semi-infinite aluminum body

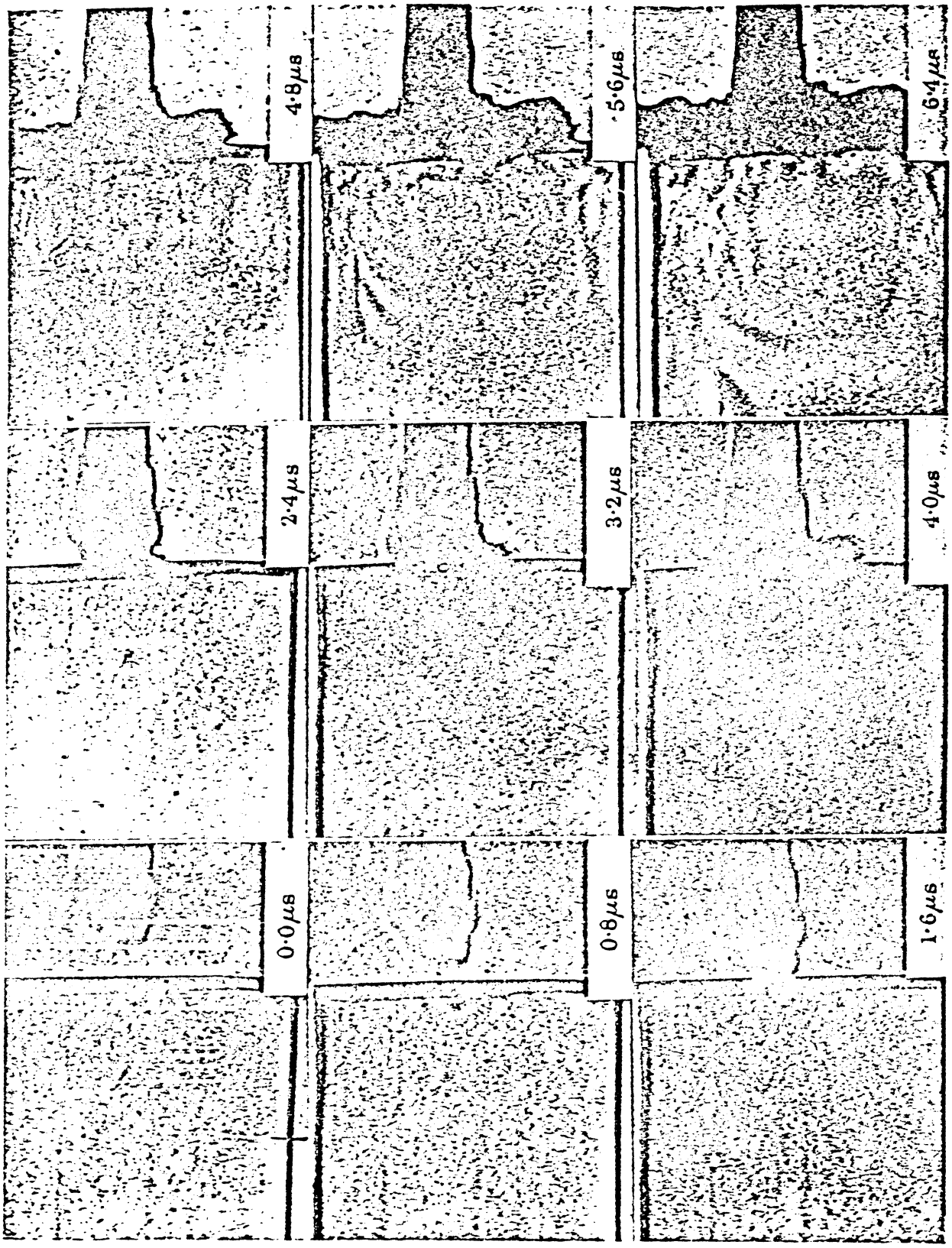

FIGURE 27 The impact of a 2 mm diameter water jet against a polymethylmethacrylate plate. Impact velocity 680 m/s. Framing interval 0·8 s. (ref. 49)

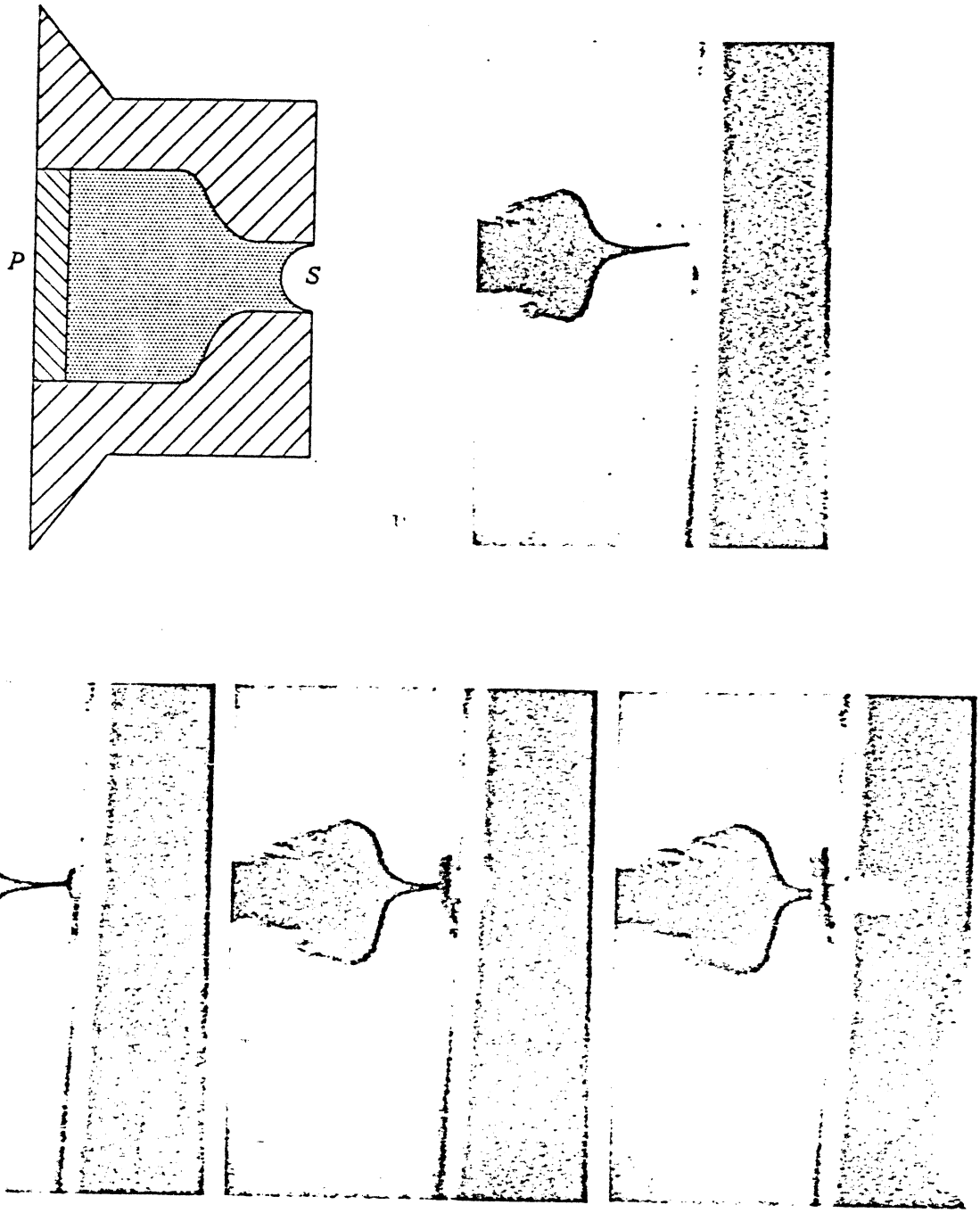

RE 28 Formation of micro-Munroe jet when a shockwave falls on the concave surface *S* of a iquid. Velocity of main jet *ca.* 650 m/s, of microjet *ca.* 1900 m/s. Interval between frames, 0·8 μs. Magn. × 5.) (ref. 88)

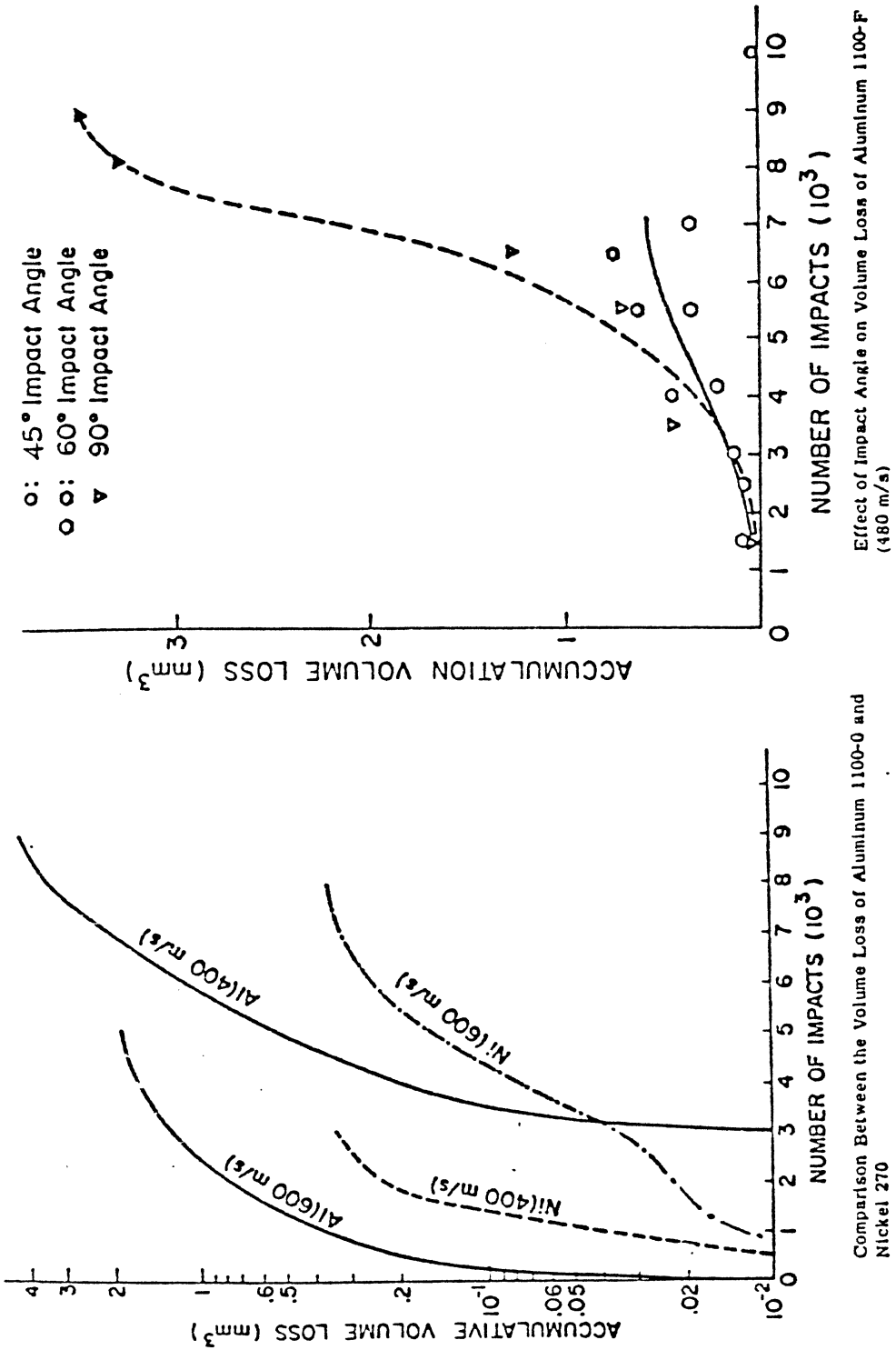

Fig. 29 Typical Results of Liquid Impact Erosion Resistance Tests with the Water Jet Gun at the University of Michigan.

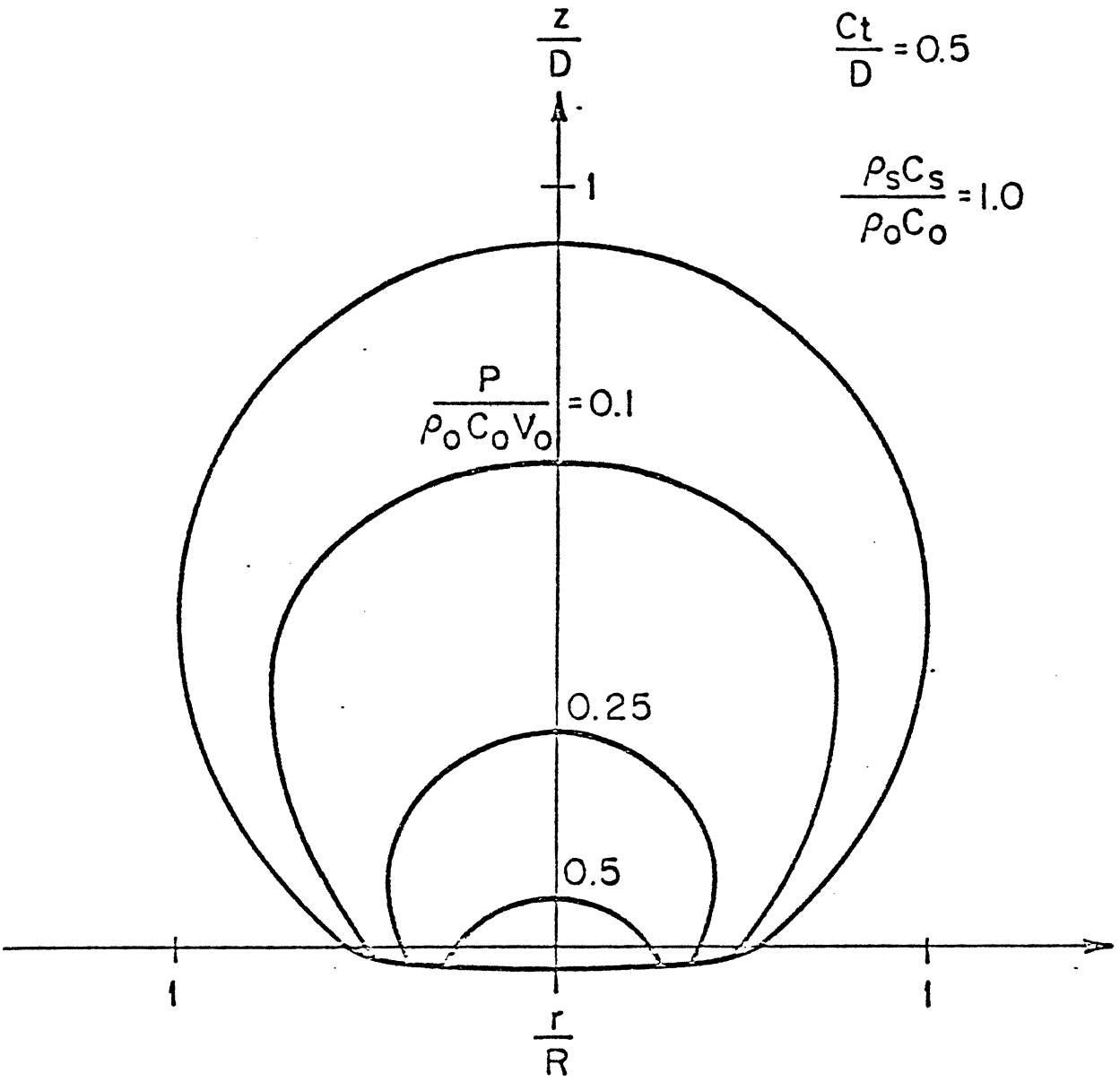

Fig. 30 Isobar Distribution in an Initially Spherical Droplet at Time Ct/D = 0.5, for Impact Mach Number of 0.2 on an Elastic Boundary, $\rho_s C_s / \rho_o C_o = 1.0$.

Gilbert Thesis
(012449-8-T)

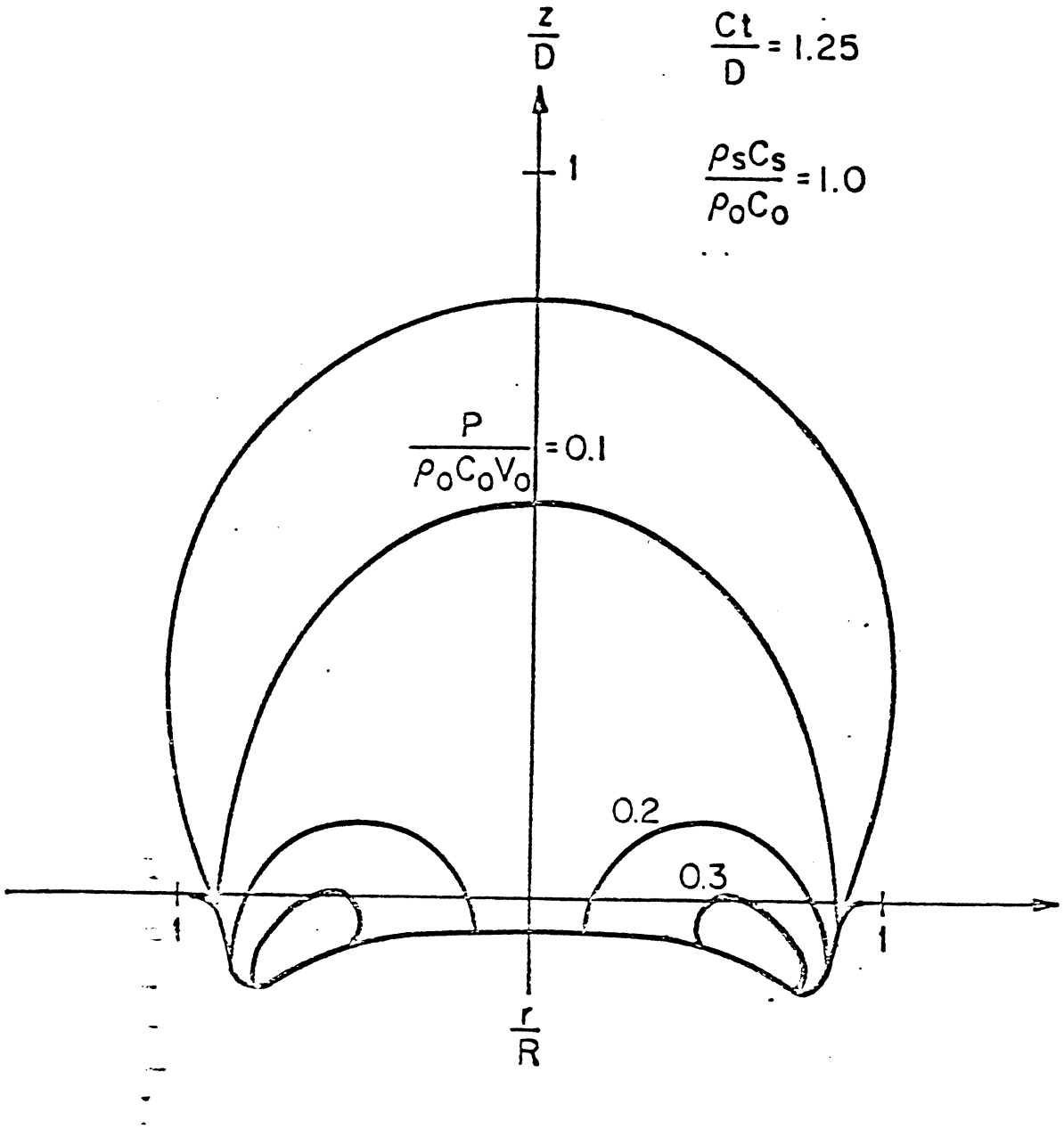

Fig. 31 Isobar Distribution in an Initially Spherical Droplet at Time Ct/D=1.25, for Impact Mach Number of 0.2 on Elastic Boundary, $\rho_s C_s / \rho_o C_o = 1.0$.

Gilbert's Thesis

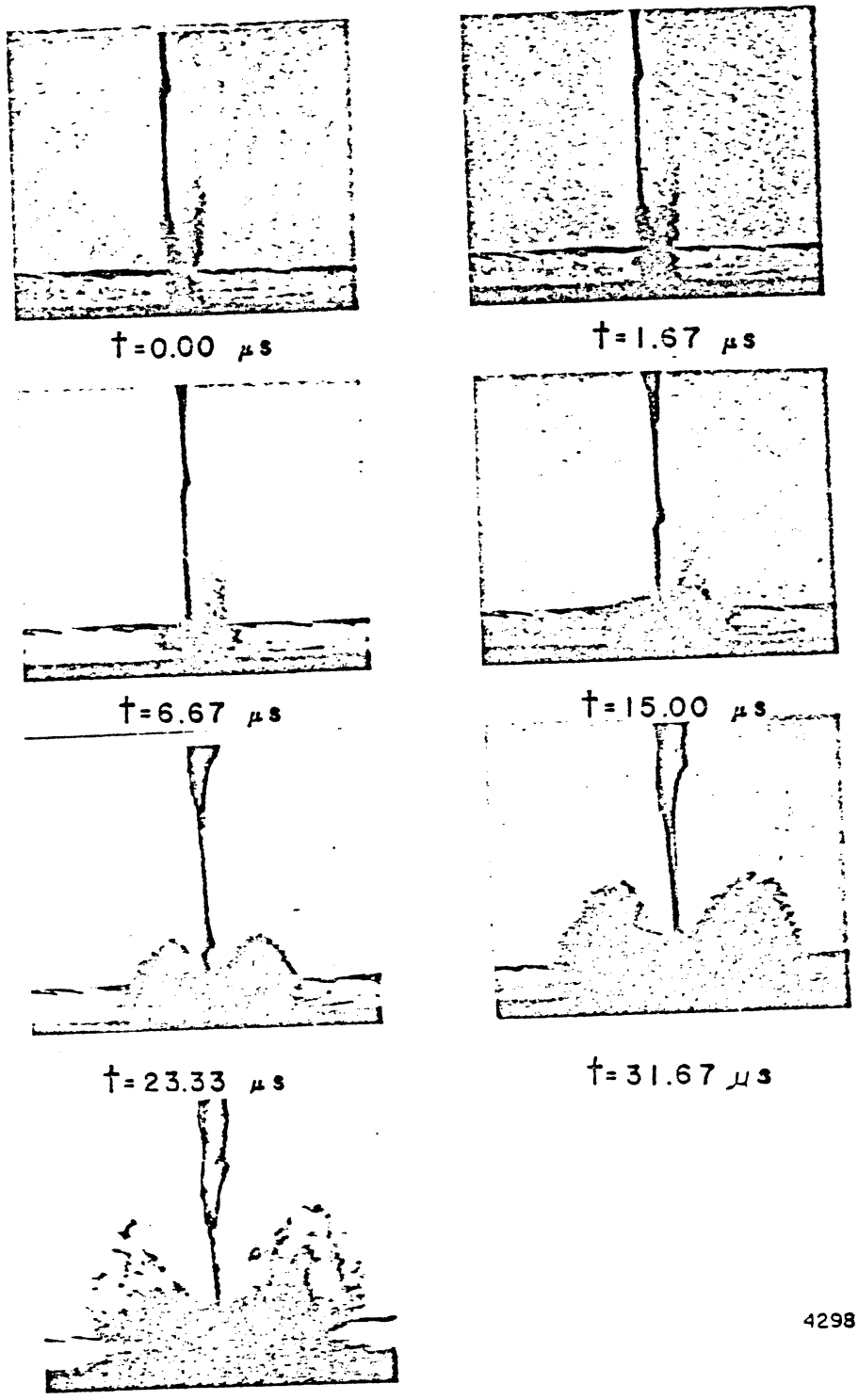

Figure 32 Prints, Run 510-BW-I-4 (ref 60)

Timm Thesis

RUN 4300-BW-I-2

JET VELOCITY = 223m/s
TARGET MTL = RUBBER A

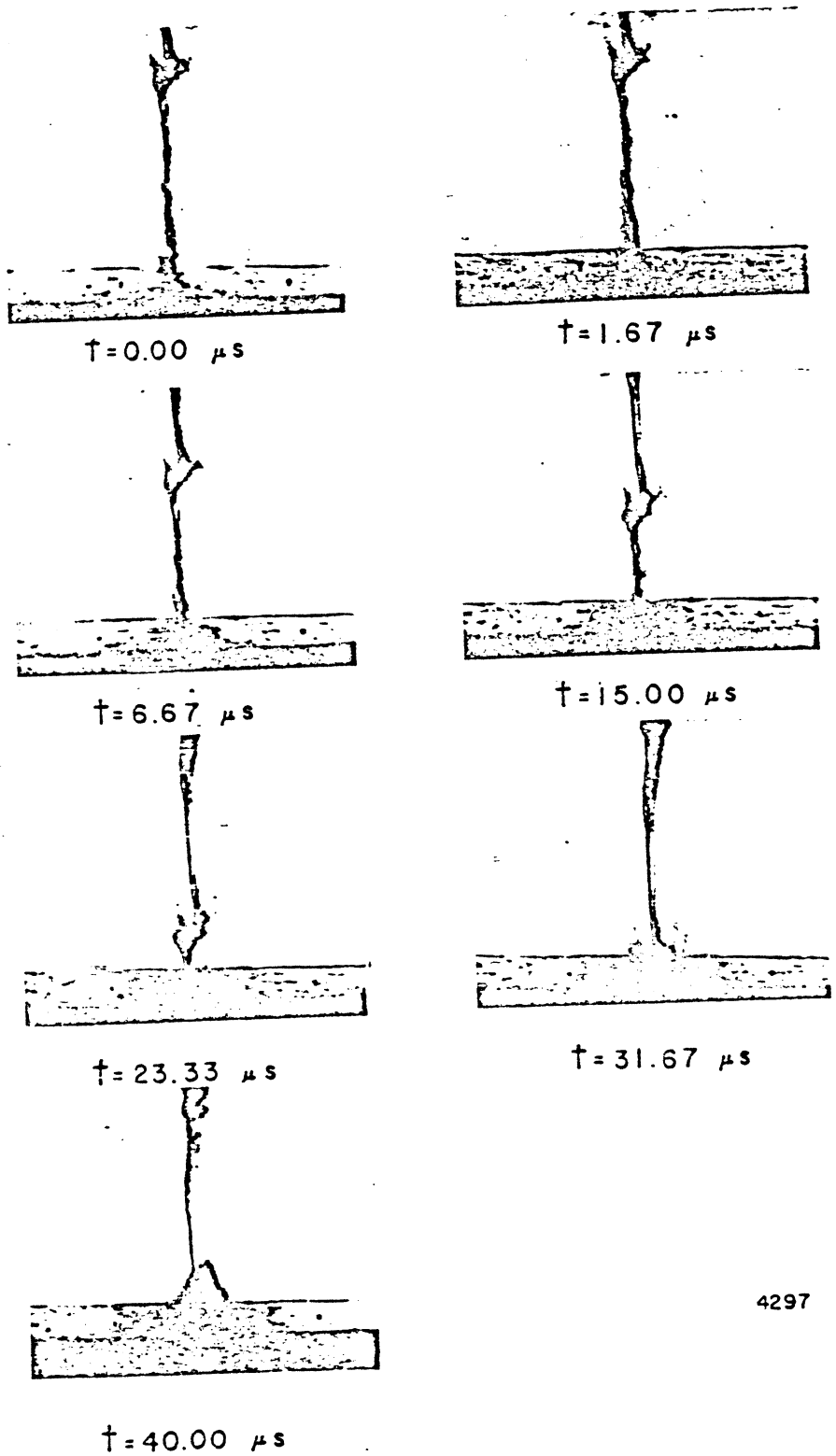

Figure 33 Prints, Run 4300-BW-I-2 (ref. 60)

Timm Thesis

PRINTS FROM SHALNEV AND KOZIREV ( )

BULLET VELOCITY = 24 m/s
SOLUTION VISCOSITY = 30,000 cp
FRAMING RATE = 8000 f/s
EXPOSURE TIME = 60 μs

4304

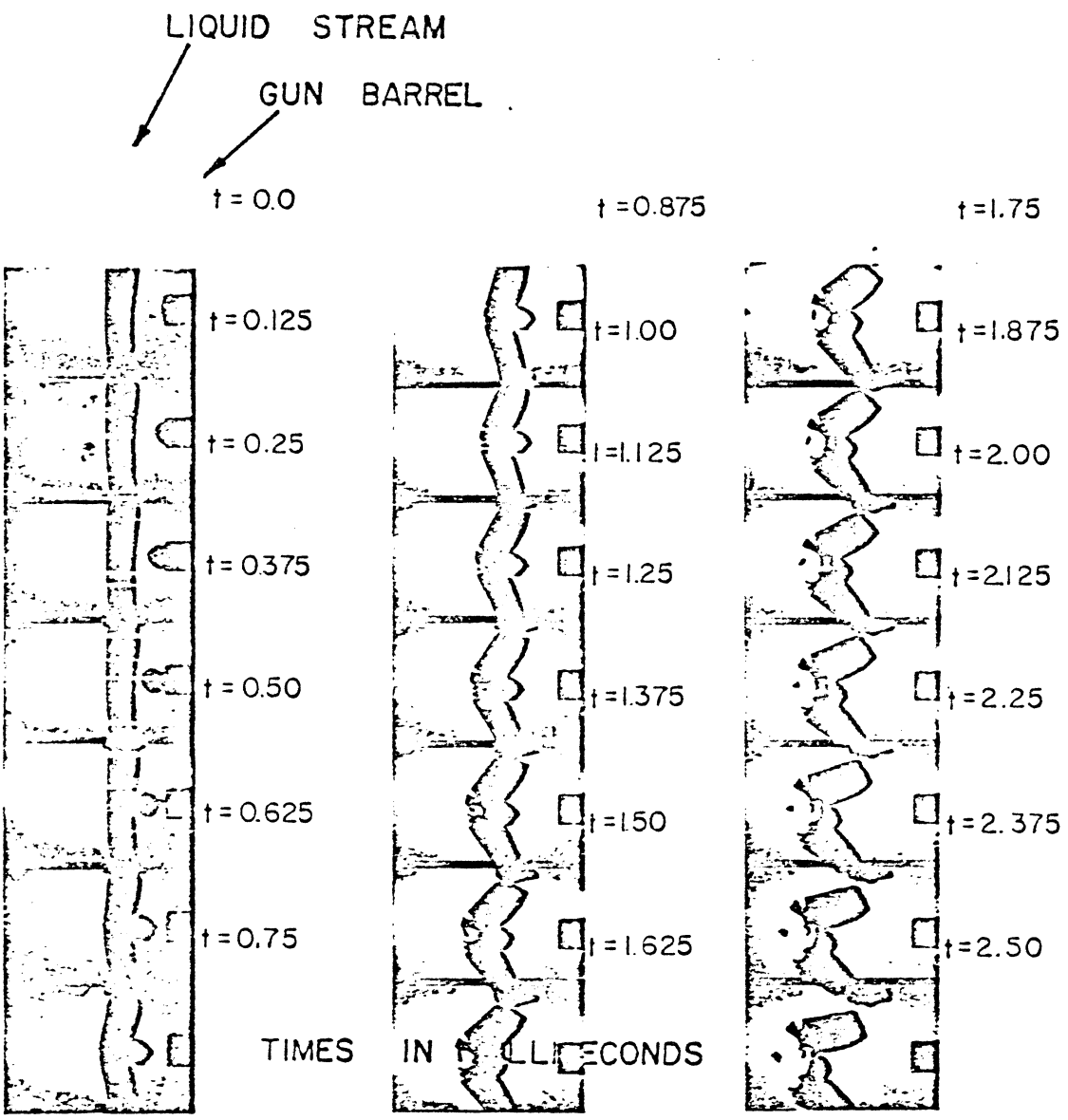

Figure 34 Prints, Shalnev and Kozirev (ref. 60)

Timm Thesis
D135.20-39-T

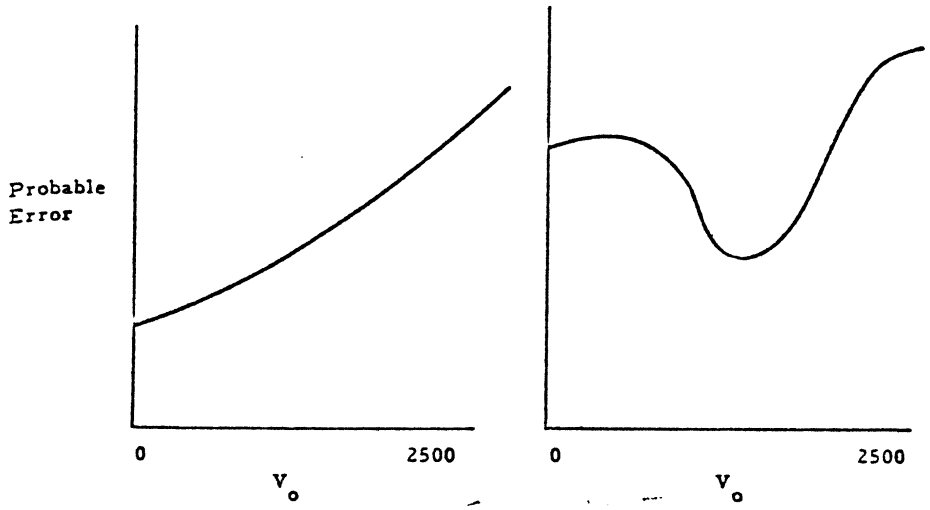

FIG. 35 Typical curves for probable error in erosion rates as a function of threshold velocity.

a curve can be fit almost equally well by various combinations of V_o (including 0) and velocity exponents α, as the present calculations show. Since, strictly, it is unlikely that there will be *zero* damage for repeated impacts at any velocity, it may be permissible to avoid the concept of threshold velocity entirely. If it is used, it is obviously a function of number of impacts per second as well as velocity, and it may be necessary to define an arbitrarily small but finite limit for MDPR which will then define the threshold velocity. Figure 1 shows two typical sketches for the relation between probable error and choice of threshold velocity for this data. For those materials exhibiting behavior of the type shown in Fig 1a, the opti-

TABLE 3—*Results of evaluation of equation* $MDPR \sin^n \theta = K(V \sin \theta - V_o)^\alpha$ *for various values of* n.

n	Threshold Velocity, ft/s	Minimum Probable Error, μm/s	Probable Error for $V_o = 0$ (μm/s)
	MATERIAL D-2		
1.0	1100	82	146
1.5	1000	88	143
2.0	900	95	141
2.5	800	101	140
	MATERIAL I-2		
1.0	350	7.3	7.7
1.5	200	7.3	7.4
2.0	100	7.2	7.3
2.5	0	7.2	7.2

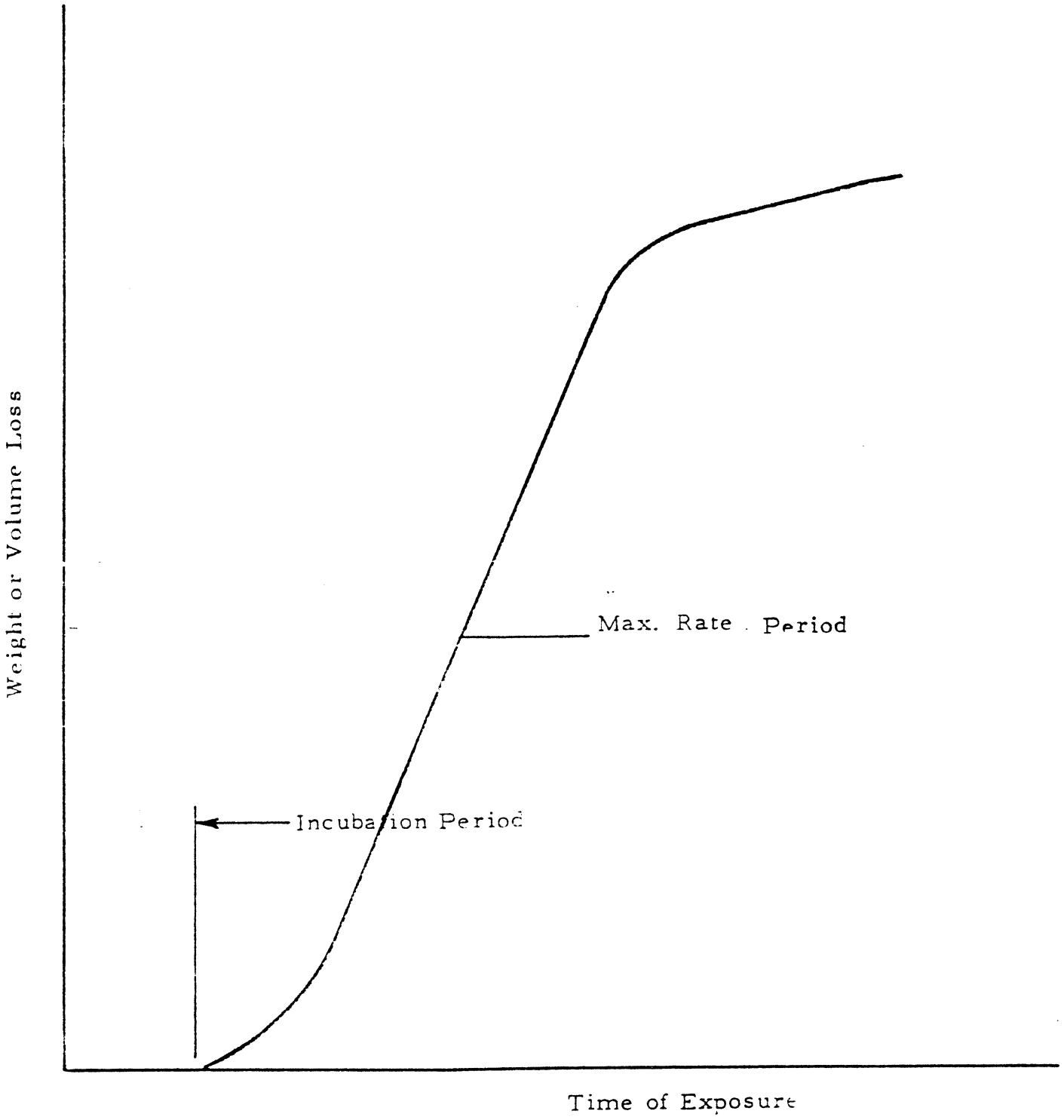

Fig. 36 - Typical Cavitation or Liquid Impact "S-Shaped" Erosion Curve

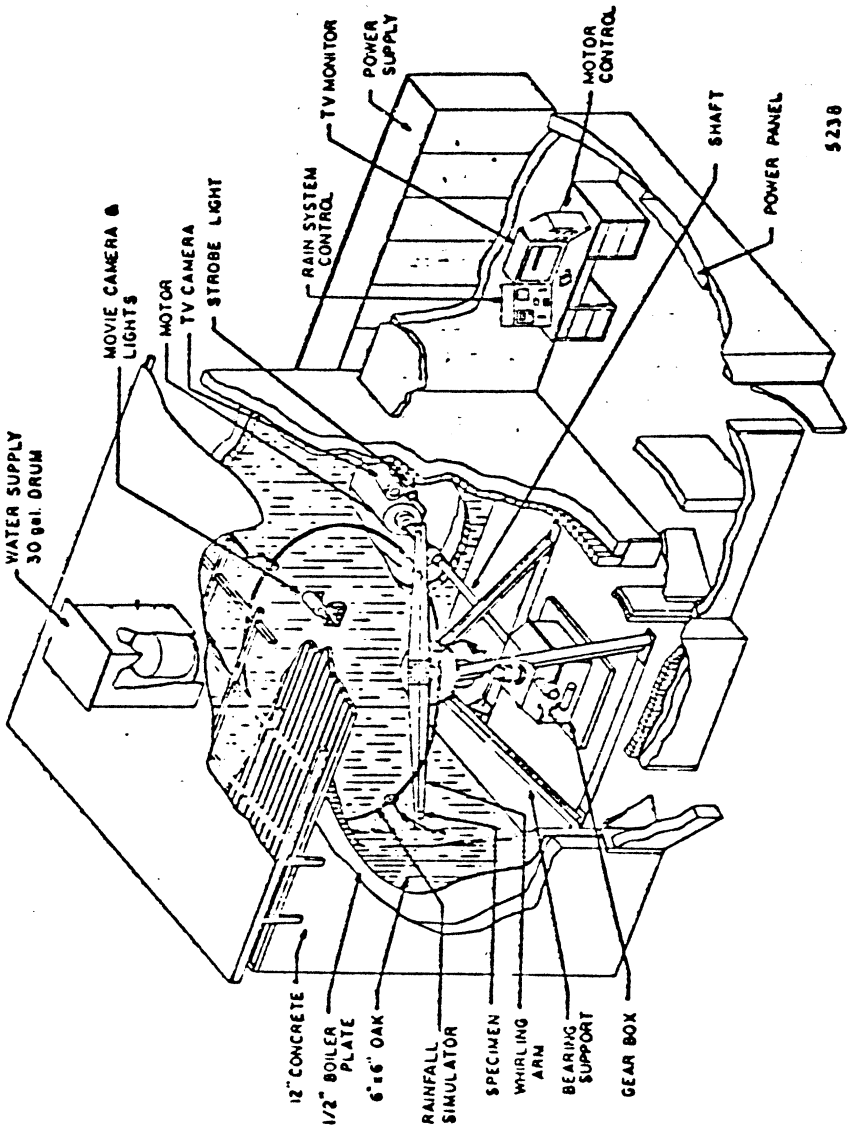

FIG. 37 *AFML rotating arm apparatus.*

Experimental

The experimental arrangement which was used is shown diagrammatically in figure 1. A small volume of liquid is contained in a stainless steel chamber. The chamber converges at one end to a fine orifice and the other end, which is open during filling, is sealed by a Neoprene disk. The liquid is extruded through the orifice as a cylindrical column by firing a flat nosed slug or bullet into the sealed end. The bore of the chamber was 0·53 cm, and the orifice diameters were usually in the range 1 to 3 mm. The inside of the chamber was polished and changes in cross sections were well rounded in order to minimize turbulence.

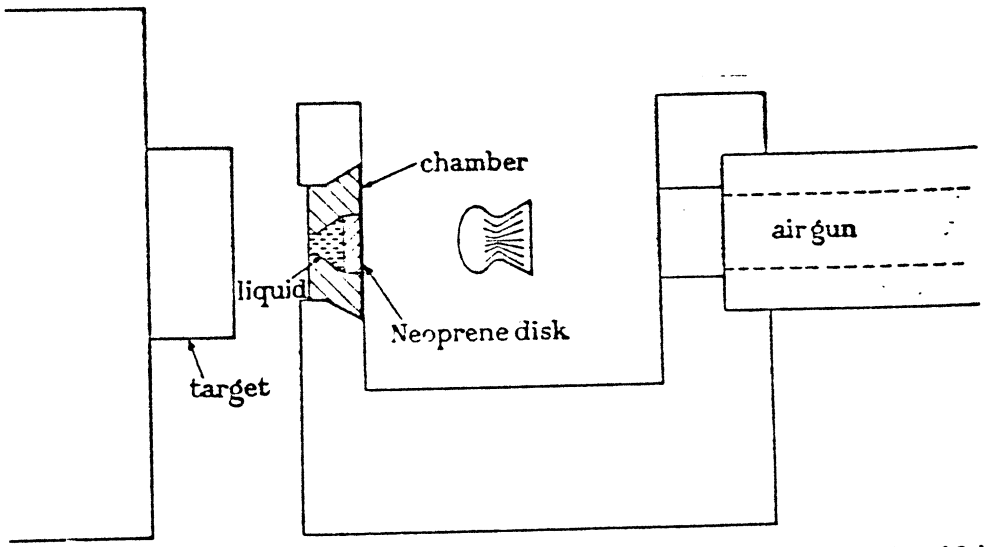

Figure 38. Diagram of the method used for producing a high velocity liquid jet. (49)
(July 1966)

The velocities of the drops produced in this way depended on the chamber dimensions and the bullet velocities. Velocities up to 1200 m/s were measured, and estimated velocities approaching 2000 m/s were possible. The upper limit was usually determined by the bursting strength of the chamber.

Measurements on the velocity and behaviour of the high speed drop were obtained with a Beckman and Whitley rotating mirror camera. Exposure times per frame of a fraction of a microsecond and framing rates of about 10^6/s were used.

Figure 2, plate 2, illustrates a typical sequence of photographs showing a cylindrical water jet produced by the apparatus striking a Perspex target. In this example the core diameter is 2·2 mm and the velocity 680 m/s. In order to produce a uniform jet the orifice section of the chamber must be clear of all liquid before firing. If there is liquid present in this section the head of the jet becomes enlarged and diffuse. Normally the jet will remain coherent for about 1 cm in air before it begins to break up. Various jet shapes have been produced with this method by slightly altering the design of the chamber.

The impact pressure

As long ago as 1928 Cook, in a paper on turbine blade erosion and cavitation erosion, pointed out that very high pressures can occur in liquid impact as a result of the

Meersburg, May 1974
(p. 319 - 345)

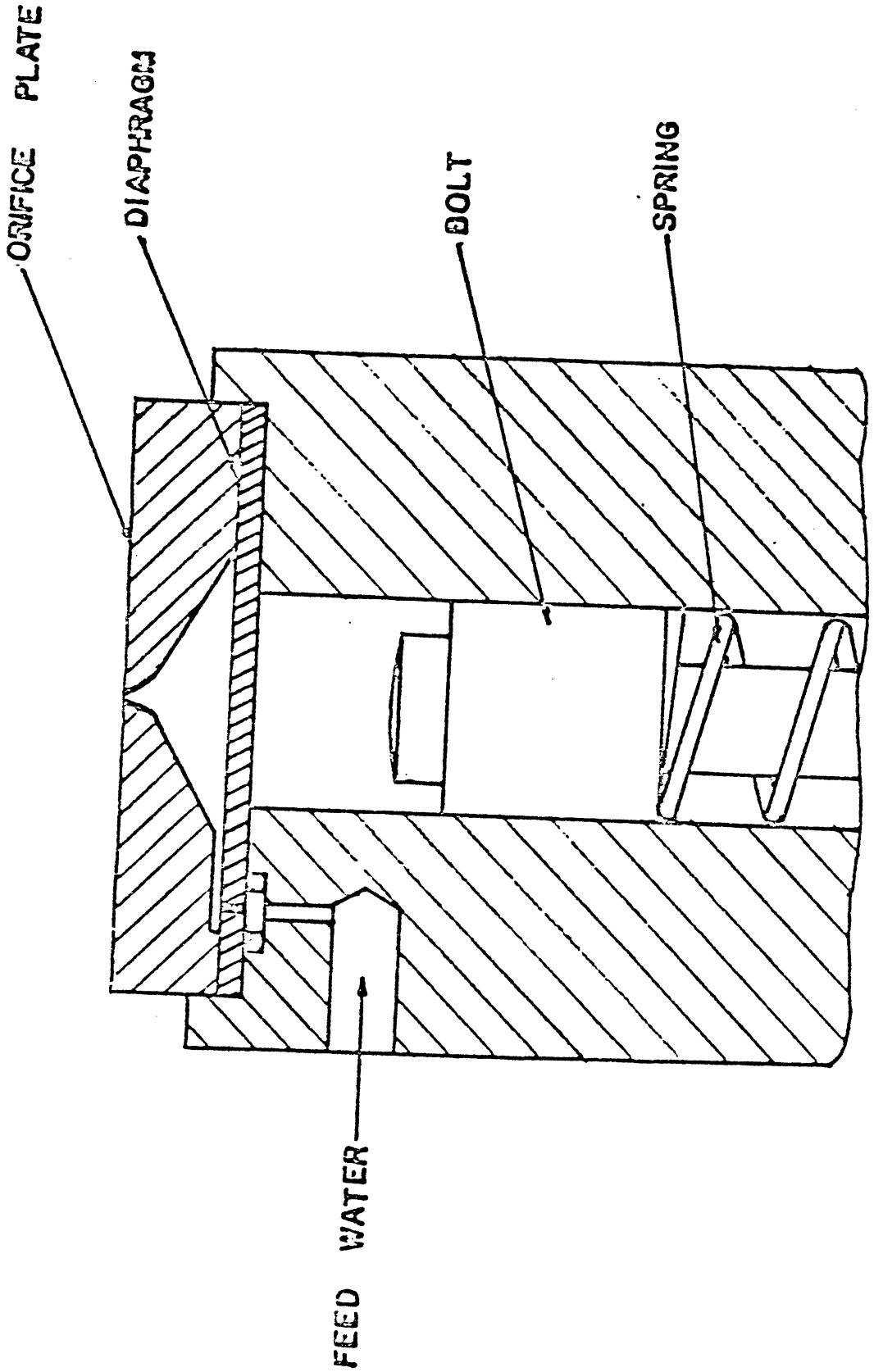

Fig. 39 Schematic of Kenyon, Michigan water gun jet.